

Dissertation
submitted to the
Combined Faculties of the Natural Sciences and for
Mathematics
of the Ruperto-Carola University of Heidelberg, Germany
for the degree of
Doctor of Natural Sciences

Put forward by
Diplom-Physiker Thomas Lompe
Born in Nienburg/Weser
Oral examination: June 1st, 2011

Efimov Physics in a three-component Fermi gas

Referees:

Prof. Dr. Selim Jochim

Prof. Dr. Johanna Stachel

Abstract

This thesis reports on experiments studying the few-body physics of three distinguishable fermionic atoms with large scattering lengths. The experiments were performed with ultracold gases of fermionic ${}^6\text{Li}$ atoms in three different hyperfine states. By tuning the strength of the interactions between the atoms with Feshbach resonances and measuring the rate constants for inelastic three-atom and atom-dimer collisions the intersections of two universal trimer states with the three-atom and atom-dimer continuum could be located. Subsequently, one of these Efimov states was directly observed with RF-association spectroscopy. Using this technique the binding energy of this Efimov state was measured as a function of the strength of the interparticle interactions. The experiments presented in this thesis provide a nearly complete understanding of the universal few-body physics of three-component Fermi gases of ${}^6\text{Li}$ atoms. This understanding will be the foundation for future studies of the many-body physics of three-component Fermi gases.

Zusammenfassung

Diese Arbeit beschreibt die experimentelle Untersuchung der Wenigteilchenphysik dreier unterscheidbarer Fermionen mit großen Streulängen. Die Experimente wurden mit ultrakalten Gasen aus ${}^6\text{Li}$ -Atomen in drei verschiedenen Spinzuständen durchgeführt. Dazu wurde mithilfe von Feshbachresonanzen die Stärke der Wechselwirkung zwischen den Atomen variiert und die Rate von inelastischen Drei-Atom- und Atom-Dimer-Kollisionen gemessen. Auf diese Weise konnten die Kreuzungspunkte von zwei universellen Trimerzuständen mit dem Drei-Atom- und Atom-Dimer-Kontinuum beobachtet werden. Des Weiteren konnten im Rahmen dieser Arbeit solche Efimovzustände mit spektroskopischen Mitteln direkt nachgewiesen werden. Mithilfe dieser Radiofrequenzassoziationsspektroskopie wurde die Bindungsenergie eines Efimovzustandes als Funktion der Wechselwirkungsstärke vermessen. Durch die in dieser Arbeit vorgestellten Experimente wurde ein nahezu vollständiges Verständnis der universellen Wenigteilchenphysik dreikomponentiger Fermigase aus ${}^6\text{Li}$ -Atomen ermöglicht. Dieses Verständnis ist die Grundlage für zukünftige Studien der Vielteilchenphysik ultrakalter dreikomponentiger Fermigase.

Contents

1	Introduction	1
2	Ultracold Fermi gases	5
2.1	The ideal Fermi gas	5
2.2	Universality in ultracold gases	8
2.3	The s-wave scattering length	9
2.4	Zero-energy scattering resonances and halo dimers	13
2.5	Feshbach resonances in ultracold gases	15
2.6	The special case of ${}^6\text{Li}$	19
2.7	Universal dimers in a two-component Fermi gas	21
2.7.1	Atom-dimer and dimer-dimer scattering	23
2.7.2	Formation of weakly bound molecules in a two-component Fermi gas	24
2.8	Many-body physics in a two-component Fermi gas	26
2.8.1	The BEC-BCS crossover	26
2.8.2	Experiments in the BEC-BCS crossover	28
2.9	Adding a third component	30
3	The Efimov effect	35
3.1	Efimov's scenario for three identical bosons	35
3.2	Hyperspherical treatment of the three-body problem	39
3.2.1	The hyperspherical coordinates	39
3.2.2	The Fadeev equations	41
3.2.3	Hyperspherical potentials and the Efimov effect	42
3.3	Efimov's radial law	45
3.3.1	Binding energies of Efimov states	48
3.4	Scattering properties	49
3.4.1	Three-body recombination	49
3.4.2	Atom-dimer scattering	52
3.4.3	Effects of finite collision energy	54
3.5	The Efimov effect for distinguishable particles	55

3.6	Experimental observations of the Efimov effect	57
4	Experimental Setup	61
4.1	The vacuum chamber	62
4.2	Magneto-optical trap and Zeeman slower	64
4.2.1	The Zeeman slower	64
4.2.2	The magneto-optical trap	65
4.3	Optical dipole trap	70
4.4	Feshbach coils	73
4.5	Imaging systems	75
4.6	Standard experiment cycles	77
4.6.1	Creating a molecular BEC	77
4.6.2	Creating a weakly interacting Fermi gas	79
5	Studying Efimov physics by observing collisional loss	83
5.1	Creating a three-component Fermi gas	84
5.2	Three-body recombination in the low-field region	86
5.3	Going to the high-field region	87
5.3.1	Lowering the collision energy	87
5.3.2	Predictions from theory	91
5.4	Three-body recombination in the high-field region	91
5.5	Atom-dimer scattering	96
5.5.1	Creating atom-dimer mixtures	96
5.5.2	The $ 1\rangle$ - $ 23\rangle$ mixture: Crossings of Efimov states	98
5.5.3	The $ 3\rangle$ - $ 12\rangle$ mixture: Ultracold Chemistry	103
5.5.4	The $ 2\rangle$ - $ 13\rangle$ mixture: Suppression of two-body loss	106
5.6	The spectrum of Efimov states in ${}^6\text{Li}$	107
6	RF-Association of Efimov Trimers	111
6.1	RF-spectroscopy in a two-component system	111
6.2	Finding an initial system for trimer spectroscopy	114
6.3	Challenges for trimer association	116
6.3.1	Maximizing the Rabi frequency	118
6.4	Trimer Association from an atom-dimer mixture	120
6.5	RF-association of Efimov trimers: Achievements and prospects	132
7	From few- to many-body physics	135
7.1	Studying the many-body physics of a three-component Fermi gas	135
7.2	Three-component Fermi gases in optical lattices	139
8	Conclusion and outlook	145

Chapter 1

Introduction

The quantization of angular momentum is one of the most fundamental and most stunning properties of nature. The size of this quantum is given by the reduced Planck constant \hbar .¹ All known elementary particles carry inherent angular momentum, which is called spin. The constituents of matter (i.e. quarks and leptons) have a spin of $1/2$, while the known gauge bosons (photons, W and Z bosons and gluons) have a spin of 1. This gives rise to another fundamental property of nature: The division of all particles into two classes: Fermions, which have half integer spin, and bosons, which have integer spin.

This small difference has far-reaching consequences. While two identical bosons can sit on the same "pixel of the universe", this is forbidden for identical fermions. This leads to a completely different behavior for many-body systems consisting of identical bosons or fermions. If an ideal gas of bosonic particles is cooled down to zero temperature, all particles accumulate in the single-particle ground state and form a Bose-Einstein-Condensate (BEC) [Ein25, And95, Dav95]. In contrast, in an ideal Fermi gas at $T = 0$ the particles occupy all available energy states starting from the lowest level up to the Fermi energy E_F .

Systems composed of fermionic particles are ubiquitous in nature. Examples for small and mesoscopic Fermi systems are nucleons, atomic nuclei and the electrons in an atom. The most famous many-body system of fermions - and probably the one with the highest technological relevance - is the Fermi gas formed by the valence electrons in a solid. The microscopic behavior of these electrons determines bulk properties of the material such as electrical conductivity. For temperatures much smaller than the the Fermi temperature $T_F = E_F/k_B$ this Fermi gas can become a superfluid and the electrical resistance of the material drops to zero [Onn11]. This phenomenon can be explained by the BCS theory of superconduc-

¹This constant can be viewed as the "pixel size of the universe" as it also defines the minimum phase space volume $(2\pi\hbar)^3$ to which any particle can be localized according to Heisenberg's uncertainty relation $\Delta p \times \Delta x \gtrsim 2\pi\hbar$.

tivity [Coo56, Bar57a, Bar57b]. This theory postulates that for weak attractive interactions and low enough temperature electrons with opposite spins, i.e. with projections of their spin angular momentum vector onto the quantization axis of plus and minus $\hbar/2$,² pair up to form Cooper pairs, which condense into a superfluid.

Compared to condensed matter physics, the studies of ultracold gases of neutral fermionic atoms are a very recent development, which began only twelve years ago [DeM99]. By using fermionic atoms in two different Zeeman substates it is possible to create systems that effectively behave like a system consisting of spin 1/2 particles. These systems can be much simpler than their "real world" counterparts yet still exhibit the essential physics. An example for this is the observation of a Mott-insulating state in an ultracold Fermi gas in an optical lattice potential [Jor08, Sch08b], a phenomenon which has been known from solid-state physics for many decades [Mot37].

However, ultracold gases can do more than provide simplified realizations of known phenomena; they also allow a level of experimental control unmatched by any other system. One example for this are the interparticle interactions in these gases, which are usually dominated by elastic two-body collisions. These can be described by a single parameter: the s-wave scattering length a . The strength of these interactions can be continuously tuned from zero across $\pm\infty$ back to zero using Feshbach resonances. This has allowed to observe phenomena such as the BEC-BCS crossover [Bar04b], which had been predicted in the context of condensed matter physics thirty years before [Leg80, Noz85]. Another spectacular achievement in the field of ultracold two-component Fermi gases was the observation of high-temperature superfluidity at a critical temperature of $T_c \approx 0.2 T_F$, which is higher than that of high- T_c superconductors [Zwi06a].

All these experiments were performed with systems containing atoms in two different spin states, yet in nature there are fascinating systems that contain many more types of distinguishable fermions. One example is the Quark-Gluon-Plasma (QGP), a hot state of deconfined quarks the universe reached about a picosecond after the big bang. This state has been studied in heavy ion collisions at TeV energies at RHIC [PHE05, STA05, PHE10] and LHC [ALI10, ATL10]. On the opposite end of the phase diagram of quantum chromodynamics (QCD), at low temperature and high net baryon density intriguing phenomena such as color superconducting and color-flavor locked (CFL) states have been predicted, which might exist in neutron stars. However, as these systems are governed by the strong interaction observing these physics requires either extremely high energy or extremely high density. Reaching the temperatures and densities necessary to form a QGP requires huge experimental effort, and the only way to gain information

²This is commonly referred to as spin \uparrow and \downarrow or $\pm 1/2$.

about the system is to study the "ashes" of hadronic particles that are left after the sample cools below the critical temperature for deconfinement. On the other hand, direct experimental studies of quark matter at the high densities and low temperatures where color superconducting phases can be expected are completely impossible.

Under these circumstances it is natural to consider ultracold gases as a convenient system to study multi-component Fermi systems [Rap07, Rap08, Paa06, Hon04]. The first experimental work in this direction was performed by our group in the spring of 2008, when we managed to prepare the first quantum-degenerate three-component Fermi gas [Ott08]. This gas consisted of ultracold ${}^6\text{Li}$ atoms in three different Zeeman sublevels of the electronic ground state. Since then, three-component Fermi gases of ${}^6\text{Li}$ have been created by several other groups [Huc09, Nak10b]. ${}^6\text{Li}$ has the unique advantage that it is possible to simultaneously tune the interparticle interactions between the atoms in the different spin states using Feshbach resonances. As these resonances all occur in the same magnetic field region, all two-particle interactions can be made resonant at the same time. For high magnetic fields all two-body interactions between atoms in different spin states are very similar, and the system has an approximate $\text{SU}(3)$ symmetry. This makes ${}^6\text{Li}$ a perfect candidate for studying the many-body physics of quantum degenerate three-component Fermi systems.

However, before one can make an attempt to study the many-body physics of this system, it is necessary to understand the underlying few-body physics, which are dominated by universal bound states. This thesis details our studies of these few-body physics, and how our findings affect future studies of many-body systems. The most striking feature of these few-body physics is the Efimov effect: For a system of three particles whose two-body interactions are described by a scattering length a , one finds that around each resonance of this two-body scattering length there is an infinite series of universal trimer states. This phenomenon was first predicted by V. Efimov in 1970 [Efi71, Efi70], but finding a system where it could be experimentally observed proved to be difficult. The first clear evidence for the existence of Efimov states was obtained in an experiment with bosonic Cesium atoms in 2006 [Kra06]. The group of R. Grimm used a Feshbach resonance to tune the scattering length to a value where the binding energy of an Efimov state coincides with the energy of three free atoms. This leads to a collisional resonance for the three-body scattering and therefore to an enhanced three-body recombination, which can be observed as a loss of atoms from the trap. Since then, this has become the standard technique for studying Efimov physics with ultracold gases, which has been used to confirm the existence of Efimov states in various experiments [Zac09, Bar09, Ott08, Huc09, Gro09, Gro10, Pol09, Wil09, Ste09, Fer09, Kno09, Lom10a, Nak10b]. However, it is not possible to directly probe the properties of the trimers with this method.

We have applied this technique to a three-component Fermi gas of ${}^6\text{Li}$ to map out the spectrum of Efimov states in this system. We have located all collisional resonances in the three-atom and atom-dimer scattering caused by the presence of Efimov states [Ott08, Wen09b, Lom10a]. This gives us all the information necessary to calculate all few-body properties of the system which are relevant for our planned studies of many-body physics.

Additionally, the fact that we use a three-component Fermi gas has allowed us to develop new experimental techniques for studying Efimov physics which could not be realized with bosonic systems. We used radio-frequency (RF) spectroscopy to directly observe Efimov trimers by associating them from a mixture of atoms and dimers [Lom10b]. This also constitutes the first measurement of the binding energy of an Efimov trimer.

This thesis is organized as follows: The second chapter gives a brief introduction into the physics of a two-component Fermi gas before moving on to the three-component system. This is followed by an introduction of the Efimov effect in chapter three. Chapter four describes the experimental setup and the basic experimental procedure for creating a degenerate Fermi gas. Chapter five details our studies of three-atom and atom-dimer collisions in our three-component Fermi gas and discusses how these measurements allow to calculate the spectrum of Efimov states in ${}^6\text{Li}$. The sixth chapter describes the direct observation of an Efimov trimer with RF-association spectroscopy. In the final chapter of this thesis the impact of our results on future studies of the many-body physics of a three-component Fermi gas is examined; followed by a short discussion of our plans to study three-component Fermi gases in an optical lattice.

Chapter 2

Ultracold Fermi gases

All experiments described in this thesis have a two-component Fermi gas as a starting point. Therefore a detailed understanding of the physics of two-component Fermi gases is required before one can start to explore a three-component system. This chapter will give a brief overview of the aspects of this physics that are essential for the understanding of this thesis. It will start with a discussion of a non-interacting (ideal) Fermi gas and its density distribution. As our Fermi gases consist of ultracold neutral atoms we will then discuss the – fortunately very simple – interactions between these particles, followed by an explanation how these interactions can be tuned using Feshbach resonances. Then we briefly introduce the ^6Li system, which has some unique properties that are crucial for the success of our experiments. The next section will mainly be concerned with the formation of molecules in a two-component Fermi gas, and the stability of these molecules against inelastic collisions. The final sections will give a brief overview of the many-body physics of two-component Fermi gases and the qualitative changes one can expect when adding a third component to the system.

2.1 The ideal Fermi gas

The most powerful toolset available to describe the behavior of a large many-body system is without any doubt statistical physics. If one tries to apply these tools in a regime where quantum mechanical effects are important, one finds that bosons and fermions behave differently. While two or more identical bosons can occupy the same quantum state, this is forbidden for fermions by the Pauli principle. Therefore Bosons and Fermions occupy the available quantum states according to different distribution functions - the so-called Bose and Fermi distributions. The

Fermi distribution – here in its grand canonical formulation –

$$f(E, \mu, T) = \frac{1}{e^{(E-\mu)/k_B T} + 1} \quad (2.1)$$

describes the occupation probability $f(E, \mu, T)$ for each quantum state depending on the energy of the state E , the chemical potential μ and the temperature T of the system. In our case the chemical potential is fixed by the condition that the total particle number N has to be conserved. In the zero temperature case one can directly see that $f(E < \mu, T = 0) = 1$, while $f(E > \mu, T = 0) = 0$. At zero temperature the chemical potential therefore corresponds to the energy of the highest occupied state. This is defined as the Fermi energy

$$E_F = \mu(N, T = 0). \quad (2.2)$$

The Fermi energy is the natural energy scale of the system to which all other energies have to be compared. By defining the Fermi temperature $T_F = E_F/k_B$ and the Fermi wave number $k_F = \sqrt{2mE_F}/\hbar$ one can get corresponding scales for temperature and momentum.

In a harmonic oscillator potential

$$V(x, y, z) = \frac{1}{2}m(\omega_x^2 x^2 + \omega_y^2 y^2 + \omega_z^2 z^2) \quad (2.3)$$

with trapping frequencies $(\omega_x, \omega_y, \omega_z)$ in x,y and z direction one has $E = \frac{\mathbf{p}^2}{2m} + V(\mathbf{r})$ and the Fermi distribution becomes

$$f(\mathbf{r}, \mathbf{p}) = \frac{1}{e^{(\frac{\mathbf{p}^2}{2m} + V(\mathbf{r}) - \mu)/k_B T} + 1}. \quad (2.4)$$

In this case the Fermi energy is given by

$$E_F = (6N)^{1/3} \hbar \bar{\omega}, \quad (2.5)$$

where $\bar{\omega} = (\omega_x \omega_y \omega_z)^{1/3}$ is the mean trapping frequency.

To obtain the spatial and momentum distribution of the ideal Fermi gas in a harmonic trap one has to multiply the distribution 2.4 with the density of states $1/(2\pi\hbar)^3$ and integrate over momentum and space respectively. This yields

$$n(\mathbf{r}, T = 0) = \frac{8N}{\pi^2 x_F y_F z_F} \left(1 - \frac{x^2}{x_F^2} - \frac{y^2}{y_F^2} - \frac{z^2}{z_F^2}\right) \quad (2.6)$$

for the spatial and

$$n(\mathbf{p}, T = 0) = \frac{8N}{\pi^2 p_F^3} \left(1 - \frac{p^2}{p_F^2}\right)^{3/2} \quad (2.7)$$

for the momentum distribution, with the Fermi momentum p_F and the Fermi radii (x_F, y_F, z_F) defined by

$$E_F = \frac{p_F^2}{2m} = \frac{1}{2}m\omega_x^2 x_F^2 = \frac{1}{2}m\omega_y^2 y_F^2 = \frac{1}{2}m\omega_z^2 z_F^2. \quad (2.8)$$

From this one can see that while trapping an ideal Fermi gas in an anisotropic potential affects the shape of the cloud, its momentum distribution remains isotropic. An anisotropic expansion of a Fermi gas which has been released from its trapping potential can therefore be used as a signature for hydrodynamic behavior [O'H02, Tre11].

For $0 < T \lesssim 0.5 T_F$ the spatial and momentum distributions are much more complicated, as the chemical potential μ is no longer equal to E_F . For the spatial distribution of a Fermi gas in a harmonic trap one obtains [Wei09]

$$n(\mathbf{r}) = -\left(\frac{mk_B T^2}{2\pi\hbar^2}\right)^{(3/2)} \text{Li}_{3/2}\left(-e^{\left(\frac{\mu - V(\mathbf{r})}{k_B T}\right)}\right), \quad (2.9)$$

where

$$\text{Li}_n = \frac{1}{\Gamma(n)} \int \frac{t^{(n-1)} dt}{e^t/x - 1} \quad (2.10)$$

is a polylogarithmic function.

This density distribution is rather complicated, which makes developing a model for three-body loss in a system with such a density distribution a quite challenging task. For this and other reasons (see Sect. 3.4.3 and 6.3) we have generally tried to avoid this regime for the experiments described in this thesis. Therefore we will refrain from discussing it here in more detail, more information on this topic can be found in [Wei09, Wen09a].

For even higher temperatures $T \gtrsim 0.5 T_F$ the system reaches the classical limit, where the number of particles is much smaller than the number of available quantum states. Under these conditions it does not matter anymore whether two particles can occupy the same quantum state and the system is well described by a Boltzmann distribution. In this case the density distribution is simply a Gaussian of the form

$$n(\mathbf{r}) = n_0 e^{-\left(\frac{x^2}{\sigma_x^2} + \frac{y^2}{\sigma_y^2} + \frac{z^2}{\sigma_z^2}\right)} \quad (2.11)$$

where

$$\sigma_i = \sqrt{\frac{k_B T}{m\omega_i^2}} \quad (2.12)$$

are the $1/\sqrt{e}$ radii of the cloud and

$$n_0 = \frac{N}{(\pi)^{(3/2)} \sigma_x \sigma_y \sigma_z} \quad (2.13)$$

is the peak density in the trap center. The many body physics of this system is classical and much simpler than the many-body physics of strongly interacting degenerate Fermi gases, which is still not fully understood even for two-component gases. Using a thermal gas allows us to study the few-body physics of three distinguishable fermions in a system whose many-body physics are completely understood. This greatly simplifies the evaluation of the experiments.

2.2 Universality in ultracold gases

The concept of universality is one of the major recurring themes of this thesis. It is founded on a separation of scales between the long-range and short-range physics of a system. If there is a sufficient separation of scales the details of the microscopic physics are no longer resolved on a macroscopic scale and its effects can be described by a few effective parameters. Quantities that depend only on such effective parameters are independent of the nature of the underlying microscopic physics and are therefore called universal.

One of the most prominent examples for this is low-energy scattering, which is also highly relevant for this thesis. Let us consider the scattering of two particles whose interaction potential has a finite range r_0 . In our case, these particles are two neutral atoms interacting via a van-der-Waals potential with a finite range r_{vdW} , but the same reasoning can be applied to any system with a finite-range interaction. If the de Broglie wavelength λ_{DB} of the colliding particles is much larger than the range of the interaction potential between the particles the details of this potential are not resolved in the collision. Under these circumstances the scattering properties of the system are described by a single number: the s-wave scattering length a . A more formal derivation of the scattering length will be given in the following section.

In ultracold gases λ_{DB} is usually on the order of $1\ \mu\text{m}$ or more, while typical values of r_{vdw} are below $5\ \text{nm}$. Consequently the scattering length describes the scattering properties of ultracold atoms almost perfectly. The second great advantage of ultracold gases is that they are dilute: The average distance between the particles is usually several orders of magnitude larger than the range of the interaction potential. This means that the atoms in these gases only interact via collisions. As we have just seen these collisions are universal, as they are fully described by the scattering length. Therefore many-body observables such as the average energy per particle or the critical temperature for superfluidity in a two-component Fermi gas that depend on the strength of the interparticle interactions are also universal.

If we additionally impose the condition $a \gg r_0$ universality does not only apply to the scattering of two particles, but also to their most shallow bound state. This

shallow dimer state then has a binding energy which is much smaller than the characteristic energy associated with the range of the potential. Therefore the particles do not probe the details of the interaction potential and the binding energy of the dimers is given by the universal relation

$$E_B = \frac{\hbar^2}{\mu a^2}, \quad (2.14)$$

where μ is the reduced mass of the two particles. For a molecule consisting of two atoms with the same mass m , μ is equal to the mass of a single atom. These universal dimers will be discussed in more detail in Section 2.4.

One field where such universal two-body states have been discussed is nuclear physics. Examples are the deuteron, which has been described as a weakly bound state of a neutron and a proton, and the ${}^8\text{Be}$ nucleus, which is a weakly bound pair of two alpha particles. It has even been suggested that the X(3872), a $c\bar{c}$ meson with a mass of 3872 MeV/ c^2 , is actually a universal molecule of two charm mesons [Vol04, Bra04].

All these examples are the result of an accidental fine-tuning of the interaction potential between the particles, which causes these shallow bound states. However, in ultracold gases the scattering length can be tuned using Feshbach resonances (see Section 2.5). Therefore ultracold atoms provide a perfect environment to study such universal bound states.

Describing weakly bound molecules of three particles requires an additional non-universal parameter. This three-body parameter describes the effect of short-range three-body physics on the long-range behavior of the three-body system, just like the scattering length does for the two-body problem. The properties of such universal trimer states will be discussed in chapter 3.

2.3 The s-wave scattering length

To describe the quantum mechanical scattering of two particles we have to solve the stationary Schrödinger equation for this system. The first step is to go into the center-of-mass frame to reduce the two-body problem of two colliding particles to the simpler problem of one particle with effective mass $\mu = \frac{m_1 m_2}{m_1 + m_2}$ scattering off an interaction potential $V(r)$. In our case this potential is spherically symmetric. If the interaction potential has a finite range the wavefunction of the scattering particle has to be equal to the wavefunction of a free particle for $r \rightarrow \infty$. In this case the incoming particles can be described by a plane wave

$$\Psi_{in} \propto e^{ikz} \quad (2.15)$$

for $r \rightarrow \infty$, while the scattered particle is described by a spherical wave

$$\Psi_{out} \propto f(\theta, k) \frac{e^{ikr}}{r}. \quad (2.16)$$

Here $f(\theta, k)$ is the probability amplitude for a particle with momentum $\hbar k$ to scatter under an angle θ . $f(\theta, k)$ is directly related to the differential cross section $d\sigma/d\Omega$, which for two distinguishable particles is given by [Fli05]

$$\frac{d\sigma}{d\Omega} = |f(\theta, k)|^2. \quad (2.17)$$

We can now describe the scattering process by combining the wavefunctions Eq. 2.15 and Eq. 2.16 to

$$\Psi_{sc} = \Psi_{in} + \Psi_{out}. \quad (2.18)$$

As the scattering potential is radially symmetric, we can expand this wavefunction into eigenfunctions of angular momentum, the Legendre polynomials $P_l(\cos \theta)$. This is called the partial wave expansion and results in the following expression for the scattering amplitude (see for example [Fli05, Wei09])

$$f(\theta, k) = \frac{1}{2ik} \sum_{l=0}^{\infty} (2l+1) (e^{2i\delta_l(k)} - 1) P_l(\cos \theta), \quad (2.19)$$

where $\delta_l(k)$ is the phase shift between the incoming and scattered wavefunction for each partial wave. These phase shifts contain all relevant information about the scattering process. By inserting Eq. 2.19 into Eq. 2.17 and integrating over the solid angle we obtain the total cross section

$$\sigma(k) = \frac{4\pi}{k^2} \sum_{l=0}^{\infty} (2l+1) \sin^2 \delta_l. \quad (2.20)$$

For two particles interacting via a short-range two-body potential the phase shift $\delta_l(k)$ approaches zero like k^{2l+2} for $k \rightarrow 0$ [Fli05]. For vanishing collision energy ($k \rightarrow 0$) one can therefore neglect all but the lowest partial wave $l = 0$. The scattering amplitude then simplifies to

$$f_0 = \frac{1}{2ik} (e^{2i\delta_0(k)} - 1). \quad (2.21)$$

We can now expand the scattering phase shift δ_0 in a power series of k^2 , which reads

$$k \cot(\delta_0(k)) = -\frac{1}{a} + \frac{1}{2} r_e k^2 + O(k^4), \quad (2.22)$$

which defines the s-wave scattering length a and the s-wave effective range r_e . For sufficiently small $k \ll 1/r_e \approx 1/r_0$ one can truncate the series after the first term, resulting in

$$a = \lim_{k \ll 1/r_0} -\frac{\tan \delta_0}{k}.^1 \quad (2.23)$$

If one inserts this into Eq. 2.21 one obtains the scattering amplitude for pure s-wave scattering

$$f(k) = -\frac{a}{1 + ika}, \quad (2.24)$$

which can be inserted into Eq. 2.17 and integrated over Ω to obtain the total cross section for the s-wave scattering of two distinguishable particles

$$\sigma_{dist} = \frac{4\pi a^2}{1 + k^2 a^2}. \quad (2.25)$$

In the limit $ka \ll 1$, which is the usual situation in ultracold gases this simplifies to an energy-independent cross-section

$$\sigma = 4\pi a^2. \quad (2.26)$$

However, for resonant interactions it is possible to reach the regime where $ka \gg 1$. In this case the scattering cross section is limited to

$$\sigma = \frac{4\pi}{k^2} \quad (2.27)$$

by the momentum of the scattering particles. This is actually one of the major challenges for our measurements, as will become clear in Section 3.4.3.

For the scattering of two identical particles Eq. 2.17 is slightly modified to

$$\frac{d\sigma}{d\Omega} = |f(\theta, k) \pm f(\pi - \theta, k)|^2, \quad (2.28)$$

where the plus (minus) sign applies to identical bosons (fermions) respectively. This results in a factor of 2 higher cross section for identical bosons

$$\sigma_{idbosons} = \frac{8\pi a^2}{1 + k^2 a^2}, \quad (2.29)$$

while for identical fermions the two terms cancel out leading to a vanishing cross section

$$\sigma_{idfermions} = 0 \quad (2.30)$$

¹In the absence of a resonance caused by an accidental fine-tuning of the potential r_e is of order r_0 [Bra06]

for identical fermions. Therefore the lowest partial wave for the scattering of identical fermions is $l = 1$. As we have seen such p-wave collisions are suppressed with $k^{2l+2} = k^4$, so at ultracold temperatures and in the absence of p-wave scattering resonances identical fermions can be assumed to be non-interacting. Performing experiments with ultracold Fermi gases therefore requires distinguishable fermions. These can either be atoms in different spin states of the same isotope or atoms of different species.

Mean-field energy of a weakly interacting gas

Let us now consider the effect of interparticle interactions in a many-body system². We do this by looking at the wavefunction of a particle with momentum $\hbar k$ moving a distance l through a gas with density n , which consists of particles which are distinguishable from the incoming particle but have the same mass m . If the system is in the weakly interacting ($na^3 \ll 1$) and ultracold ($k \ll 1/r_0$) regime, the outgoing wavefunction is a superposition of all possible scattered waves resulting from collisions with atoms in the gas. In the far field, this results in a phase shift

$$\delta = -\frac{4\pi anl}{k} \quad (2.31)$$

of the incoming wave [Dal98]. As the individual scattering processes are fully described by the scattering length a , this phase shift depends only on a and the density of scatterers n . The phase shift corresponds to a change of the particle momentum $\Delta k = \delta/l$ while the particle moves through the gas. This is equivalent to a change in energy of

$$\frac{\hbar^2(k^2 - (k - \Delta k)^2)}{2m} \approx -\frac{4\pi\hbar^2 an}{m}. \quad (2.32)$$

This is the potential energy

$$U = \frac{4\pi\hbar^2 an}{m} \quad (2.33)$$

of a particle due to the mean field of the surrounding particles. If $a > 0$ this energy is positive, which means that the particle is repelled by the mean field of the other particles. For $a < 0$ it is negative, which corresponds to an attractive mean field potential. Therefore the interparticle interactions are called attractive for $a < 0$ and repulsive for $a > 0$. However, one should keep in mind that this only describes the effect of the scattering in the long-distance limit. On a microscopic scale of order r_{vdw} the Van-der-Waals potential between ultracold atoms is always attractive.

²We follow here the very instructive approach taken in [Dal98], more formal derivations can be found in [Pit03].

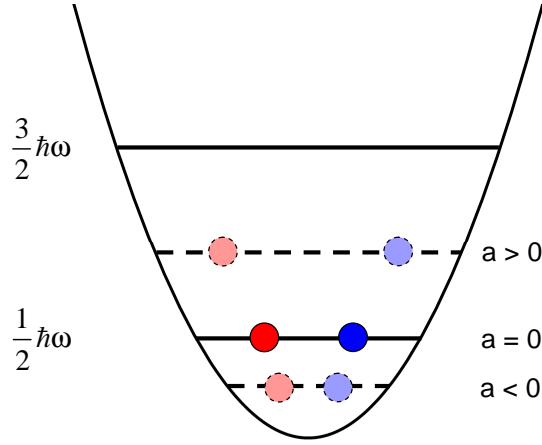


Figure 2.1: Sketch of two particles in a harmonic trap. In the non-interacting case $a = 0$ the energy of the particles is given by the levels of the harmonic oscillator. For $a > 0$ the interactions increase the energy of the system and the interactions are called repulsive. For $a < 0$ the energy of the system is decreased, which corresponds to an attractive interaction between the particles.

2.4 Zero-energy scattering resonances and halo dimers

Studying the scattering of particles - and especially looking for scattering resonances - is the main experimental approach to studying both high-energy and nuclear physics. In these cases, scattering experiments are usually performed with a well-defined, finite energy. In contrast, particles in ultracold gases collide with vanishing momentum. Here we therefore discuss the special case of scattering resonances at vanishing collision energy, which are commonly referred to as zero-energy resonances. We will first introduce the general phenomenology of a zero-energy resonance using the example of a simple box potential. We will then move on to the slightly different case of a Feshbach resonance.

Let us assume a particle with momentum $\hbar k$ scattering off a box potential with a range r_0 and depth V , where we are in the limit $k \ll 1/r_0$. As we have seen in the previous section, this scattering process can be described by the s-wave scattering length a , which is determined by the phase shift of the wavefunction according to Eq. 2.23.

For a potential with depth $V_0 = 0$, the wavefunction experiences no phase shift, and consequently the scattering length is zero (see Fig. 2.2 a). For a finite potential depth the scattered wavefunction is displaced from the unperturbed wavefunction by a distance x (see Fig. 2.2 b), resulting in a phase shift $\delta = kx$. Inserting this into Eq. 2.23 and using the small-angle approximation we find $a \approx \delta/k \approx x$. With this, we have found an intuitive physical interpretation for the concept of

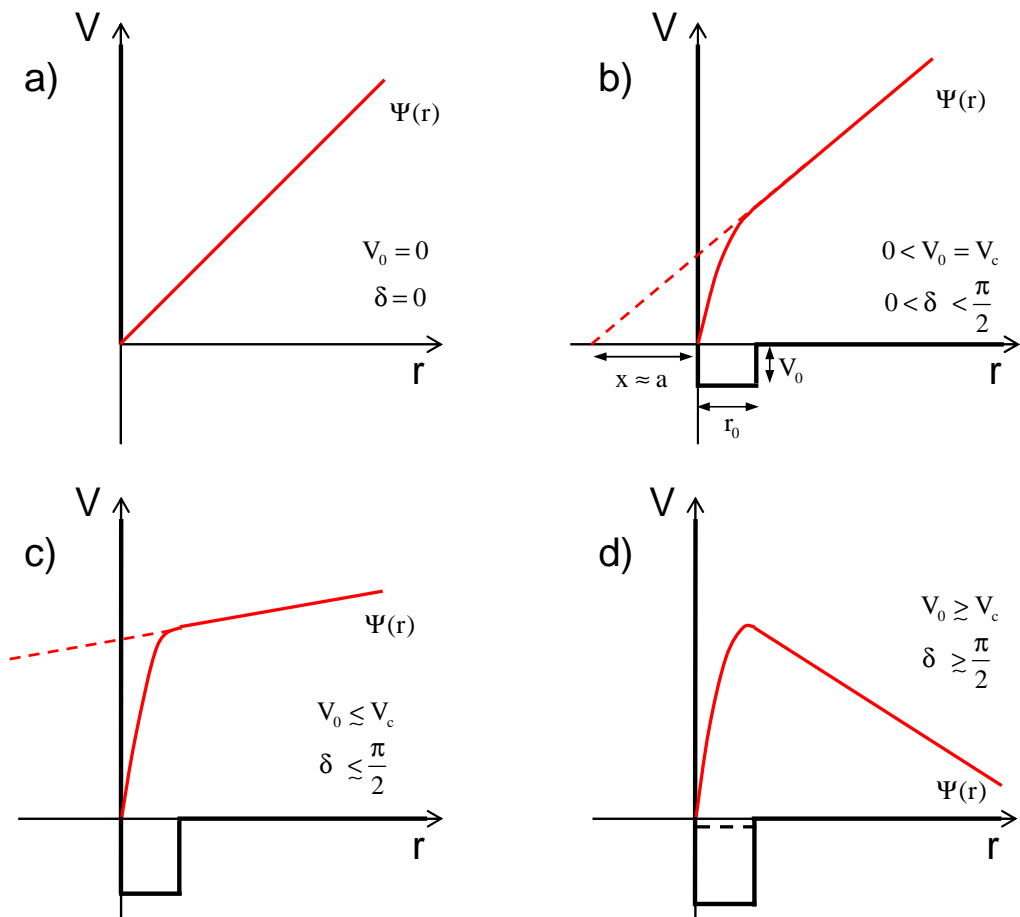


Figure 2.2: Scattering of a particle off a simple box potential. For a box with zero depth, the wavefunction of the scattered particle remains unaffected (a). For a box with a finite depth, the wavefunction is displaced by a distance $x \approx a$ by the potential (b). When the potential depth approaches the critical value V_c at which a new state becomes bound, the phase shift δ of the wavefunction approaches $\pi/2$ and the scattering length diverges (c). If there is a shallow bound state in the potential, the scattering length becomes positive (d).

the scattering length as the displacement of the wavefunction by the scattering potential. For a potential depth $0 < V_0 < V_c$, where the potential is not deep enough to support a bound state the scattering length is negative. If the potential depth approaches the critical depth V_c where the potential has a bound state with zero binding energy the phase shift between the unperturbed and scattered wavefunction approaches $\frac{\pi}{2}$, and the scattering length diverges to $-\infty$ (see Fig. 2.2 c), resulting in a pole in the scattering length for $V_0 = V_c$. For $V_0 > V_c$ the scattering length is positive, and the potential supports a weakly bound dimer state (Fig. 2.2 d). If V_0 is close to V_c the binding energy of this dimer state is given by [Zwi06a]

$$E_B = \frac{1}{4} \frac{(V_0 - V_c)^2}{\frac{\hbar^2}{mr_0^2}} = \frac{\hbar^2}{ma^2}, \quad (2.34)$$

with a scattering length $a \gg r_0$, while the actual shape of the potential drops out of the problem. The second part of Eq. 2.34 can therefore be applied to any finite-range potential with a shallow bound state close to the continuum. The wavefunction of this dimer state is of the form

$$\Psi(r) = \frac{1}{\sqrt{2\pi a}} e^{-\frac{r}{a}} \quad (2.35)$$

for $r > r_0$, so the size of the dimer is not given by the range of the potential but by the size of the scattering length. Most of the wavefunction of the dimer is located outside the range r_0 of the potential, therefore these weakly bound molecules are called halo dimers [Chi10].

To first order corrections to the universal value of the dimer binding energy are given by the finite range of the potential and scale with r_0/a . For ultracold gases they can be approximated by subtracting a so-called mean scattering length

$$\bar{a} = \frac{\Gamma(3/4)}{2\sqrt{2}\Gamma(4/5)} r_{vdw} \approx 0.487 r_{vdw} \quad (2.36)$$

from the scattering length in Eq. 2.14 [Gri93], which leads to

$$E_B = \frac{\hbar^2}{m(a - \bar{a})^2}. \quad (2.37)$$

This effective range correction extends the validity of Eq. 2.14 to lower values of the scattering length.

2.5 Feshbach resonances in ultracold gases

Ultracold neutral atoms interact via a Van-der-Waals potential whose depth and shape are determined by the properties of the colliding atoms, which are fixed by

nature. So unless there is an accidental fine-tuning of these parameters that causes a bound state to sit close to the threshold, the absolute value of the scattering length is on the order of the range r_{vdw} of the potential [Bra06]. Achieving experimental control over the scattering length of an ultracold gas therefore requires a different type of resonance. These are the so-called Feshbach resonances.

To understand Feshbach resonances we first have to introduce the concept of scattering channels. A scattering channel is given by a set of quantum numbers that fully describes the internal state of two incoming or outgoing particles. If there is a coupling, particles entering in one channel can in principle change their internal state and exit in another scattering channel. In this channel the particles generally have a different interaction potential and a different internal energy. If the energy of the incoming particles is too small to end up in a certain scattering channel this is called a closed channel. Scattering channels which are energetically allowed are called open channels³. The entrance channel is therefore by definition always an open channel.

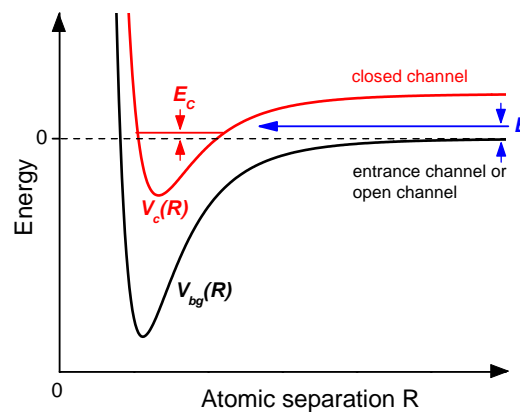


Figure 2.3: Two-channel model of a Feshbach resonance. The particles enter in the open channel, where they have the interaction potential V_{bg} (black). If the energy E of the incoming particles (blue arrow) is close to the energy E_c of a bound state in the closed channel interaction potential (red) there can be a resonant coupling of the incoming particles to the bound state in the closed channel. For ultracold gases the kinetic energy of the particles can usually be neglected and E is equal to the continuum of the open channel. Figure taken from [Chi10]

We will now take a look at a simple two-channel model with one open (entrance) channel and one closed channel, as shown in Fig. 2.3. Particles enter in the open

³In our discussion we neglect scattering channels which are forbidden by other mechanisms such as angular momentum conservation.

channel, scatter, and leave again in the open channel, as they have to fulfill energy conservation. Let us assume that there is a bound state in the interaction potential between two atoms in the closed channel, which is coupled to the open channel with a coupling strength g . As the atoms enter and leave in the open channel, the coupling to the molecular state is a second order process, whose strength is proportional to g^2 . In a naive picture a resonance occurs when the energy E_c of this bound state becomes degenerate with the energy E of the incoming particles (see Fig. 2.3). In an ultracold gas we can assume the kinetic energy of the incoming particles to be zero, and consequently a resonance should occur if the continuum of the open channel has the same energy as a bound state in the closed channel.

However, a more careful analysis [Chi10, Zwi06a] reveals that the resonance is shifted by $\delta \propto g^2$, as the coupling causes an avoided crossing between the molecular state in the closed channel and the lowest continuum state of the open channel (see Fig. 2.4). Therefore the molecular state becomes a superposition of the open and closed channel. Close to the resonance the molecules are dominated by the open channel, and their properties are well described by the universal relations 2.14 and 2.35. Farther away from the resonance the closed channel fraction becomes larger, which causes corrections to the universal formulas. The width of the universal region is determined by the width $\Gamma \propto g^2$ of the resonance, which depends quadratically on the coupling strength g .

For an ultracold gas the open and closed channel are given by different configurations of the total electron spin. These configurations - for example singlet and triplet - have different magnetic moments. Therefore one can easily bring the continuum of the open channel in resonance with a closed channel bound state by applying a homogeneous magnetic offset field B , which causes an energy shift $\Delta E = \Delta\mu B$, where $\Delta\mu$ is the difference in the magnetic moments of the open and closed channel. By varying the magnetic field around the resonance position B_0 one can therefore vary the scattering length according to the formula [Chi10]

$$a(B) = a_{bg} - a_{bg} \frac{\Delta B}{B - B_0}, \quad (2.38)$$

where a_{bg} is the background scattering length and $\Delta B = \Gamma/\Delta\mu$ is the width of the resonance (see Fig. 2.4).

In Section 2.2 we mentioned the great advantage that in ultracold gases the interparticle distance is much larger than the range of the interaction potential between the particles. The fact that we can tune the interparticle interactions using Feshbach resonances allows us to take this a step further: We can increase the scattering length to values comparable to or even larger than the interparticle spacing, thus driving the system into a strongly correlated many-body state. However, as r_0 is still much smaller than the interparticle spacing the system remains

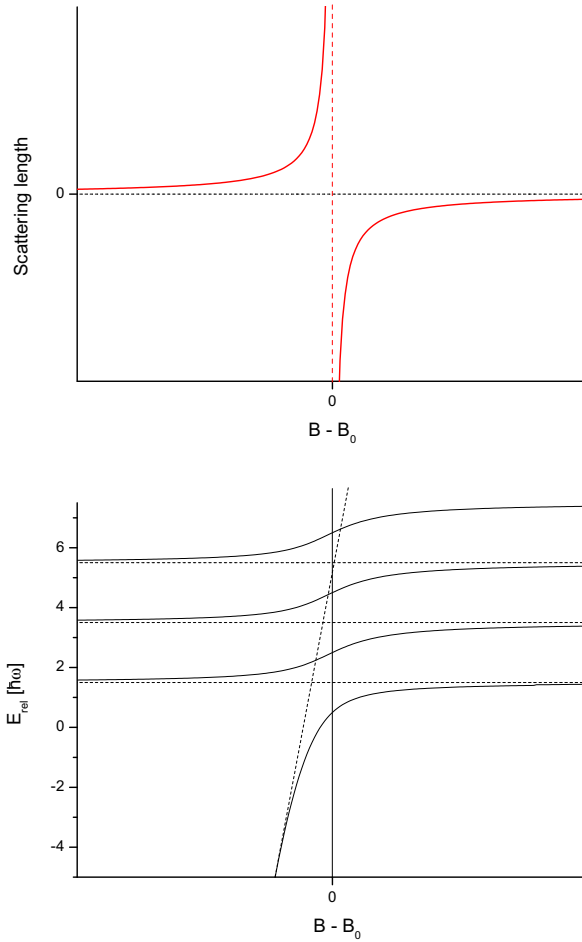


Figure 2.4: (a) Scattering length around a Feshbach resonance at $B = B_0$. (b) Sketch of the crossing of the molecular state with the continuum at a Feshbach resonance. As the atoms are usually in a trap we plot the continuum states as the relative motion of the particles in a harmonic oscillator potential. The unperturbed molecular state and trap levels are shown as dashed lines. Adiabatically crossing the resonance from the molecular side smoothly connects the molecular state to the ground state of the trapping potential, while a pair of unbound atoms in the trap gains an energy of $2\hbar\omega$ in their relative motion [Bus07]. Moving across the resonance in the opposite direction converts all atom pairs with zero relative momentum into molecules. This means that BCS-like pairs can be smoothly converted into molecules by ramping across a Feshbach resonance [Bar04b].

dilute, which gives us a strongly correlated many-body system with point-like interactions. This is an amazing playground for both theory and experiment, which currently cannot be realized in any other system.

2.6 The special case of ${}^6\text{Li}$

${}^6\text{Li}$ is an alkali atom with a single valence electron. It therefore has an electronic spin of $S = 1/2$ and a hydrogen-like level structure, which greatly simplifies laser cooling. The ${}^6\text{Li}$ nucleus consists of three protons and three neutrons, and consequently ${}^6\text{Li}$ has a nuclear spin of $I = 1$. At low magnetic fields S and I couple to a new quantum number F resulting in the two hyperfine levels $F = 1/2$ and $F = 3/2$ of the electronic ground state (see Fig. 4.4 for the complete level scheme). In the presence of an external magnetic field these states split into six magnetic sublevels $|F, m_F\rangle$ according to their magnetic quantum number m_F . We label these states with the numbers $|1\rangle$ to $|6\rangle$ as shown in Fig. 2.5. For high magnetic fields the coupling of electron and nuclear spin breaks down, and $|F, m_F\rangle$ decouples into $|S, m_s, I, m_I\rangle$. As ${}^6\text{Li}$ has an uncommonly small hyperfine constant a_{hf} , the system enters the high-field regime already at magnetic fields $B \gtrsim 50 \text{ G}$.

Any collision of two ${}^6\text{Li}$ atoms which involves an atom in state $|4\rangle$, $|5\rangle$ or $|6\rangle$ can lead to dipolar relaxation of this atom into one of the lower states $|1\rangle$, $|2\rangle$ or $|3\rangle$. For magnetic fields that are larger than a few Gauss this spin flip releases so much energy that the atoms are lost from the trap after the collision. Therefore we can only use atoms in states $|1\rangle$, $|2\rangle$ and $|3\rangle$ for our experiments, for whom dipolar relaxation is forbidden by a combination of energy and angular momentum conservation⁴.

In a scattering event the atoms feel a different interaction potential depending on the relative orientation of their electronic spins, which can be either in a singlet ($\uparrow\downarrow$) or triplet ($\uparrow\uparrow$) configuration. In the low-field regime $|m_s\rangle$ is not a good quantum number and the scattering length is a linear combination of the singlet scattering length a_s and the triplet scattering length a_{tr} . For the $|1\rangle$ - $|2\rangle$ mixture $a_s \approx 39 a_0$ while the triplet scattering length has an unusually large value of $a_{tr} \approx -2240 a_0$, where a_0 is Bohr's radius. From our previous discussion of resonant scattering we know that such a large scattering length has to be connected with a bound state in the vicinity of the continuum. In this case it is a virtual bound state which sits about 300 kHz above the continuum of the triplet potential. This is an example of an accidental fine tuning as it was discussed in Sect. 2.2. In fact,

⁴The process $|1\rangle$ - $|3\rangle \rightarrow |2\rangle$ - $|2\rangle$ is actually energetically allowed, but for high magnetic fields the released energy is small enough that the particles have to leave in an s-wave configuration, which is Pauli blocked.

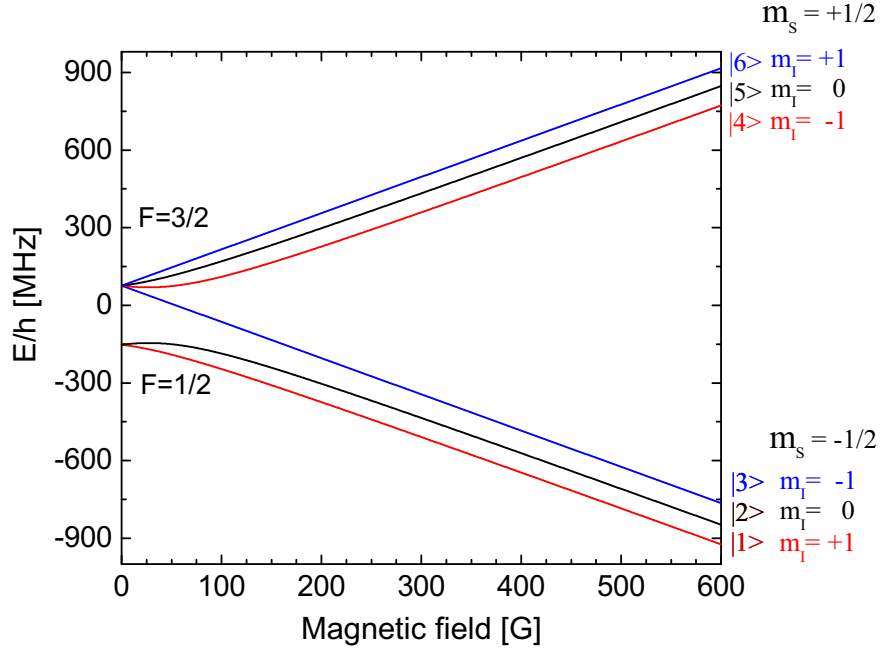


Figure 2.5: Energy of the Zeemann sublevels of the electronic ground state of ${}^6\text{Li}$ as a function of the strength of the magnetic offset field.

if the ${}^6\text{Li}$ triplet potential were only 0.1% deeper, it would support another bound state [Zwi06a, Joc04].

In the high field regime the electron spin becomes polarized and the scattering of the particles is almost purely triplet, while singlet scattering is energetically forbidden. Therefore the triplet channel is the open channel, while the singlet channel is closed. As the magnetic moment of the atoms is determined by the electron spin, the energy of the triplet channel tunes with $2\mu_B \approx h \times 3 \text{ MHz/G}$ in an external magnetic field, while the singlet state remains unaffected. This allows to tune the triplet continuum in resonance with the highest vibrational level ($\nu = 38$) of the singlet interaction potential, which causes a Feshbach resonance.

Figure 2.6 shows the scattering lengths for all stable spin state combinations as a function of magnetic field. One can see that there are Feshbach resonances for the $|1\rangle\text{-}|2\rangle$, $|2\rangle\text{-}|3\rangle$ and $|1\rangle\text{-}|3\rangle$ mixtures at magnetic fields of 834 G, 811 G and 690 G. These resonances are remarkable for their large widths of more than 100 G, which is roughly a factor of $10^2\text{-}10^3$ more than the usual widths of Feshbach resonances in ultracold gases [Chi10]. This is caused by the presence of the virtual bound state in the triplet channel, which greatly enhances the strength of the coupling to the closed channel bound state.

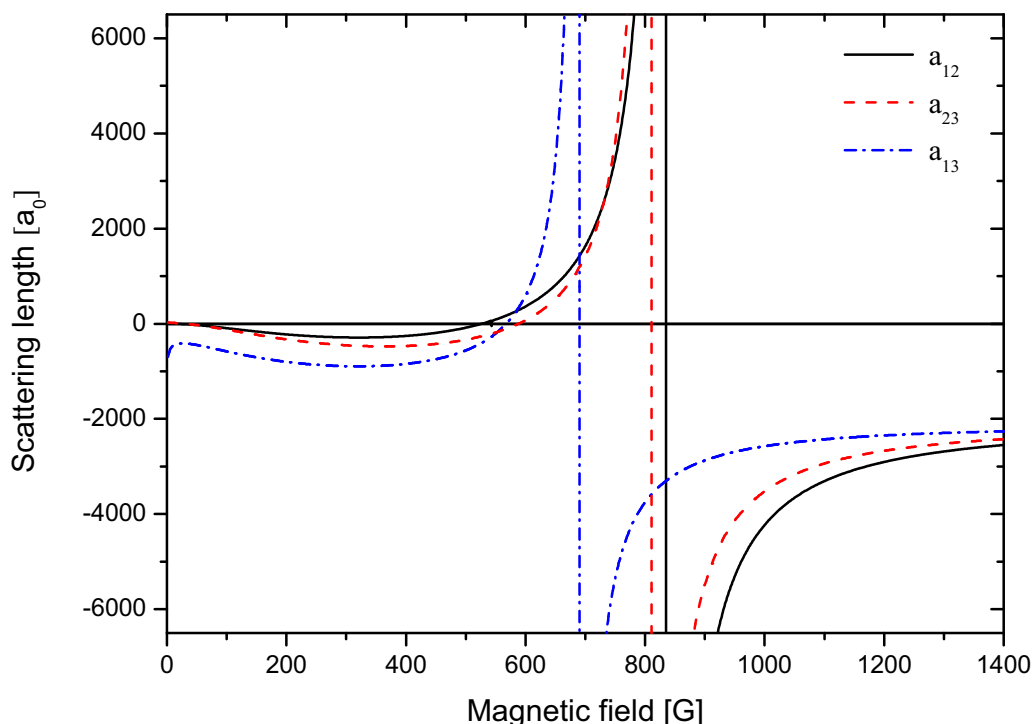


Figure 2.6: Scattering lengths (in units of Bohr's radius a_0) for the $|1\rangle$ - $|2\rangle$, $|2\rangle$ - $|3\rangle$ and $|1\rangle$ - $|3\rangle$ spin mixtures of ${}^6\text{Li}$ as a function of magnetic field.

The fact that these three Feshbach resonances overlap – i.e. that the distance between the resonance positions is smaller than their widths – is a critical condition for almost all experiments described in this thesis. Without the resonance in the triplet scattering, this would not be the case and this thesis would not have been possible in this form.

2.7 Universal dimers in a two-component Fermi gas

At first glance, the fact that gases of alkali atoms can exist at nanokelvin temperature is quite surprising: The equilibrium state of an alkali metal at this temperature is definitely a solid. However, while the gas phase is not the equilibrium state of the system, it can be a metastable state with a lifetime of minutes, much longer than the usual duration of our experiments.

The first step on the way to turning such a supercooled gas into a solid is to bind two atoms into a molecule. However, two particles cannot just collide and stick together, as the collision has to fulfill momentum and energy conservation. This requires that a third atom takes part in the collision to carry away the excess mo-

Scattering channel	Type	Position	Width
$ 1\rangle - 2\rangle$	s-wave	834 G	-300 G
$ 2\rangle - 3\rangle$	s-wave	811 G	-222.3 G
$ 1\rangle - 3\rangle$	s-wave	690 G	-122.3 G
$ 1\rangle - 2\rangle$	s-wave	543 G	0.1 G
$ 1\rangle - 1\rangle$	p-wave	159.14 G	-
$ 1\rangle - 2\rangle$	p-wave	185.09 G	-
$ 2\rangle - 2\rangle$	p-wave	214.94 G	-
$ 1\rangle - 3\rangle$	p-wave	225.33 G	-

Table 2.1: Feshbach resonances in the three energetically lowest Zeemann sub-states of ${}^6\text{Li}$. There are three broad and one narrow s-wave resonances, as well as four p-wave resonances. Values taken from [Chi10] except for the position of the $|1\rangle - |3\rangle$ p-wave resonance (own measurement).

mentum, a process which is called three-body recombination. The rate for such three-body collisions depends on the probability that three atoms "see" each other at the same time, which scales with the third power of the density. For a sufficiently low density these processes are strongly suppressed and the gas becomes metastable.⁵

This metastability is one of the most important limiting factors in experiments with ultracold gases. It sets an upper limit for the density of an ultracold Bose gas, which - depending on the atomic species - is usually between 10^{12} atoms/cm³ (e.g. ${}^{133}\text{Cs}$) and 10^{15} atoms/cm³ (e.g. ${}^{23}\text{Na}$). This density limit sets an upper limit for the temperature at which quantum degeneracy can be reached for a certain species. At the same time it limits experiments with ultracold Bose gases to the weakly interacting regime where $na^3 \ll 1$, as for large scattering lengths the larger scattering cross section leads to an enhanced three-body recombination which scales with a^4 (see Sect. 3.4.1).

However, if we consider the case of a two-component Fermi gas we immediately realize that there is a drastic qualitative difference: In a two-component Fermi gas, three-body collisions have to involve at least two identical fermions. As we have seen in Sect. 2.3 this is not possible for s-wave scattering. Accordingly three-body collisions should be completely suppressed in two-component Fermi gases, which should therefore be much more stable for large interaction strengths

⁵While this metastable state is not the true ground state of the system, we still refer to it as the ground state in the discussion of many-body physics. This is justified if the lifetime of the metastable state is much longer than the characteristic timescales of the many-body system.

$k_F a \gtrsim 1$.⁶ Experimentally, one finds that this conclusion is true for small values of a . However, if the interactions become resonant one has to include the effects of the shallow bound state and things get a lot more interesting.

First, we will examine the elastic scattering properties of these shallow dimers as well as their stability against inelastic atom-dimer and dimer-dimer collisions. Then we will discuss how these weakly bound molecules are formed in three-body collisions. This naturally leads to a discussion of the different ways to create a stable BEC of ${}^6\text{Li}_2$ molecules.

2.7.1 Atom-dimer and dimer-dimer scattering

Dimers consisting of two fermionic atoms are in principle bosonic objects that do not experience Pauli blocking. However, this is only true if the size of the dimers is much smaller than the de-Broglie wavelength $\lambda_{dB} \propto 1/k_F$ of the particles. For $a \gg r_0$ the size of the dimer is approximately a , so for $k_F a \gtrsim 1$ the fermionic nature of its constituents has to be taken into account. This means that calculating the outcome of an atom-dimer or dimer-dimer collision requires solving a three- or four-body problem, which contains either one or two identical fermions.⁷ This was done by D. Petrov et. al. in a series of papers in 2003/2004 [[Pet03](#), [Pet04](#), [Pet05](#)]. Assuming that the range of the interatomic potential goes to zero and that the scattering particles have vanishing energy, they found that the atom-dimer and dimer-dimer scattering lengths a_{ad} and a_{dd} are directly given by the atom-atom scattering length a according to

$$a_{ad} = 1.2a \quad (2.39)$$

$$a_{dd} = 0.6a.⁸ \quad (2.40)$$

If there are deeply bound levels below the shallow dimer state (which is generally the case in experiments) the universal molecule can be deexcited into such a deeply bound dimer by a collision. This releases a large amount of energy and leads to the loss of the colliding particles from the trap. These processes therefore limit the lifetime of samples containing such universal molecules.

The nature of the experiments one can do with these molecules now depends critically on the ratio between elastic and inelastic collisions in the atom-dimer and

⁶The dimensionless parameter $k_F a$ is used to compare scattering length and interparticle spacing in a Fermi gas with $T \lesssim T_F$.

⁷Except for the fact that the system includes identical fermions, this problem is actually quite similar to the three-body problem introduced in chapter 3.

⁸ a_{ad} had already been calculated in 1956 in the context of neutron-deuteron scattering in [[Sko57](#)].

dimer-dimer scattering. As their name suggests, the deep dimers actually sit deep down in the interatomic potential,⁹ consequently they have a size which is smaller than the range r_{vdw} of the potential. Relaxation of a universal molecule into such a deeply bound level therefore requires three atoms to approach each other to a distance smaller than r_{vdw} – two to form the deep dimer, and one to carry off the excess momentum. If the scattering length is large – and the individual atoms are therefore resolved in the collision process – the probability that two identical fermions involved in the collision approach each other to such a short distance is strongly suppressed.

In [Pet04, Pet05] Petrov et. al. found that this leads to the following rate constants for relaxation into deeply bound dimers in atom-dimer and dimer-dimer collisions

$$\beta_{ad} = C \frac{\hbar r_{vdw}}{m} \left(\frac{a}{r_{vdw}} \right)^{-3.33} \quad (2.41)$$

$$\beta_{dd} = C \frac{\hbar r_{vdw}}{m} \left(\frac{a}{r_{vdw}} \right)^{-2.55} \quad (2.42)$$

where C is a non-universal constant describing the overlap between the universal dimer and the deeply bound states. This means that for a gas of such ultracold molecules the stability of the gas actually increases for stronger interactions¹⁰.

The only question that remains is the value of the constant C , which depends on the non-universal properties of the specific atom. For ${}^6\text{Li}$ $C \sim 10^{15}$, which makes it possible to create molecular samples with densities of $\sim 10^{12}$ atoms/cm³ with lifetimes on the order of 10 s. This corresponds to a ration of elastic to inelastic collisions which is larger than 10^5 . In other systems such as ${}^{40}\text{K}$ the coefficient C is much larger (about one to two orders of magnitude [Reg04]), which makes the creation of long-lived molecular samples much harder.

2.7.2 Formation of weakly bound molecules in a two-component Fermi gas

Let us now consider the formation of such weakly bound molecules from a two-component gas of fermionic atoms. Forming the dimer requires a three-body collision to fulfill energy and momentum conservation. Therefore two identical fermions have to approach each other to a distance comparable to the size of the final bound state, just as it was the case for the relaxation into deeply bound dimer states discussed above. However, as the size of the universal dimer is given by

⁹At least compared to the universal molecule, which sits basically outside of the potential.

¹⁰This is completely different from the behavior of molecules consisting of bosonic atoms, which decay faster for larger values of the scattering length.

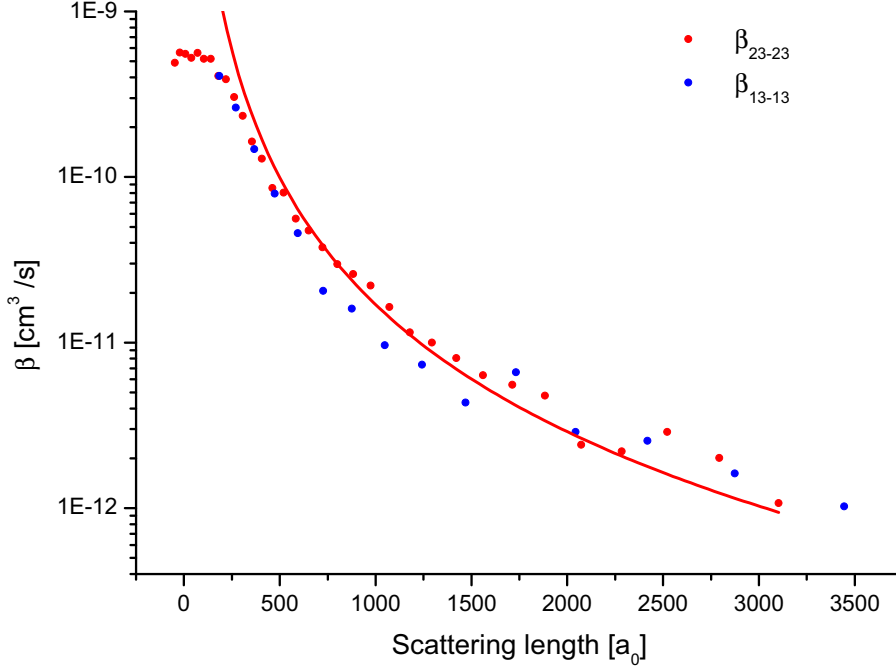


Figure 2.7: Rate coefficients for the dimer-dimer relaxation for two different two-component mixtures of ${}^6\text{Li}$ as a function of the scattering length. Both mixtures show a similar behavior, the red line shows the result of Eq. 2.42 for $C = 7 \times 10^{14}$.

the scattering length it is much larger than the deep dimers, so in this case this is a much weaker restriction. The relevant energy scale for this suppression is the binding energy E_B of the dimer, and consequently these processes are suppressed by E_{kin}/E_B where E_{kin} is the relative kinetic energy of the two identical fermions involved in the collision [Esr01, Pet03]. Combined with the general a^4 scaling of three-body recombination (see Sect. 3.4.1) this yields a rate coefficient of

$$L \approx 111 \frac{\hbar a^4}{m} \frac{E_{kin}}{E_B} = 111 a^6 \frac{E_{kin}}{\hbar} \quad (2.43)$$

for this process [Pet03].

If the released binding energy is smaller than the trap depth and the scattering length is large enough for the molecules to be sufficiently stable against inelastic collisions the produced molecules are accumulated in the trap. However, if there is a finite density of molecules they can be dissociated again in atom-dimer and dimer-dimer collisions. For a thermal gas this leads to a chemical equilibrium between the number of atoms and molecules.

By setting up the partition function of the system and minimizing the free energy one can find that the atomic and molecular phase space densities Φ_N and Φ_M are

related by [Chi04b]

$$\Phi_M = \Phi_N^2 e^{\frac{E_B}{k_B T}}. \quad (2.44)$$

As the total number of particles $N_G = N + 2M$ has to be conserved this means that for $k_B T \ll E_B$ the sample consist almost entirely of molecules. Thus we now have two ways to create samples of ultracold molecules:

The first is to start from a cold gas of atoms on the BCS-side of a Feshbach resonance and perform a slow magnetic field sweep across the resonance. This converts particles with zero relative momentum into molecules (see Sect. 2.5). The second is to perform evaporative cooling of an atomic gas at large scattering length until for $k_B T \lesssim E_B$ the molecular fraction begins to grow. By continuing to evaporate this atom-dimer mixture one ends up with an almost pure sample of molecules for $k_B T \ll E_B$. These dimers can be cooled down further until they form a molecular BEC. This procedure has been discussed in detail in [Joc03b, Chi04b] and is our standard scheme for creating molecular BECs (see Sect. 4.6). One should note that this approach is so far unique to ${}^6\text{Li}$, as it is the only system where the ratio between inelastic and elastic atom-dimer and dimer-dimer collisions is low enough for this scheme to work.

2.8 Many-body physics in a two-component Fermi gas

In this section we aim to give a brief overview of the many-body physics of strongly interacting two-component Fermi gases.¹¹ We focus on the parts that are most relevant for the experiments described in this thesis, which are the BEC-BCS crossover and Fermi gases with a population imbalance between atoms in states $|\uparrow\rangle$ and $|\downarrow\rangle$. Additionally we will mention some of the experimental techniques that have been used to probe these systems.

2.8.1 The BEC-BCS crossover

The key feature in the many-body physics of ultracold two-component Fermi gases is the BEC-BCS crossover, which smoothly connects two systems which at first glance seem completely different. Experimentally, this can be realized by starting from a Fermi gas with a weak attractive interaction and performing an adiabatic ramp across a Feshbach resonance, which binds pairs of fermions with opposite spin into bosonic molecules (see Fig. 2.4). We will start by introducing

¹¹By strongly interacting we mean that $k_F a > 1$, in contrast to the case of weak interactions for $k_F a \ll 1$.

the limiting cases (BEC and BCS) and then describe the crossover between these regimes.

In the BCS limit the system consists of spin $|\uparrow\rangle$ and $|\downarrow\rangle$ particles with a weak attractive interaction. Let us first consider the zero-temperature case. According to the BCS theory developed by Bardeen, Cooper and Schrieffer to explain superconductivity in metals [Coo56, Bar57a, Bar57b], this attractive interaction causes a pairing of particles with opposite momenta $\hbar\mathbf{k}$ and $-\hbar\mathbf{k}$ into so-called Cooper pairs. This pairing causes an energy gap

$$\Delta_0 = \frac{8}{e^2} E_F e^{\frac{\pi}{2k_F|a|}} \quad (2.45)$$

to open at the Fermi surface and the system becomes superfluid. This energy gap can be interpreted as the binding energy of the Cooper pairs. For finite temperature the critical temperature for superfluidity is given by

$$k_B T_c = \frac{e^\gamma}{\pi} \Delta_0, \quad (2.46)$$

where Δ_0 is the zero-temperature gap, $\gamma \approx 0.58$ is Euler's constant and $e^\gamma \approx 1.78$.¹² One should note that the size of the gap scales exponentially with interaction strength. As the attractive interaction in conventional superconductors is very weak, the critical temperatures for superconductivity in these systems are on the order of $10^{-4} T_F$. For a more detailed introduction to BCS-theory (given from an atomic physics perspective) see [Ket08].

The other limiting case is a weakly interacting BEC of molecules. For an ideal gas in a harmonic trap the critical temperature is

$$T_C = \frac{\hbar\bar{\omega} N^{1/3}}{\xi(3)^{1/3}} \approx 0.94 \hbar\bar{\omega} N^{1/3}, \quad (2.47)$$

where $\xi(\alpha) = \sum_{n=1}^{\infty} n^{-\alpha}$ is the Riemann Zeta function [Pit03]. The condensate fraction N_0 is given by

$$\frac{N_0}{N} = N \left(1 - \left(\frac{T}{T_C} \right)^3 \right). \quad (2.48)$$

In the presence of interactions the condensed particles form a superfluid. For a weakly interacting gas with $0 < na^3 \ll 1$ the ground state of the BEC is described by the time-independent Gross-Pitaevski equation

$$\left(\frac{\hat{p}^2}{2m} + V(\mathbf{r}) + \frac{4\pi\hbar^2 a}{m} |\Psi(\mathbf{r}, t)|^2 \right) \Psi(\mathbf{r}) = \mu \Psi(\mathbf{r}). \quad (2.49)$$

¹²Strictly speaking this formula does not give the critical temperature for superfluidity but for pair formation, however these two temperatures coincide for $a \rightarrow 0_-$.

where $4\pi a/m |\Psi(\mathbf{r})|^2$ is the mean-field energy of the condensate [Pit03].

One should note that both of these theories are only valid in the limit of weak interactions ($k_F|a| \ll 1$ and $na^3 \ll 1$). In between these regimes is the region of resonant interactions, where the scattering length diverges to $\pm\infty$.

To understand how this regime connects the BCS and BEC limits let us consider a deeply degenerate Fermi gas with small attractive interactions. These attractive interactions between the atoms pull the particles together, until the attractive mean field is balanced by the increased Fermi pressure in the smaller cloud. If we increase the strength of the interactions, the size of the cloud shrinks accordingly. In the limit of $a \rightarrow -\infty$ one would naively expect the system to collapse due to the attractive interaction. However, this collapse is prevented by the fact that the strength of the interaction cannot actually become infinite. Similar to what we have seen in Eq. 2.27, the interaction strength is limited by the momentum of the particles for $k_F|a| \gg 1$ and the system is in an equilibrium between the repulsion due to Fermi pressure and the attractive interaction. Right on resonance the system enters the so-called unitary regime where both the Fermi pressure and the strength of the interaction are solely determined by the Fermi wave vector k_F . In this limit the energy of the system is simply the energy of the non-interacting system rescaled by a universal number β to

$$E = (1 - \beta)E_F. \quad (2.50)$$

For a two-component Fermi gas $(1 - \beta)$ has been determined by both experiment and theory to be about 0.42.

If we further increase the attraction between the particles, two atoms can form a weakly bound dimer. When ramping across a Feshbach resonance, the size of a cooper pair continuously shrinks until the two atoms form a real-space molecule as a flips from $-\infty$ to $+\infty$. These molecules are bosonic and do not experience Pauli blocking, but as the scattering length is now positive the Fermi pressure is replaced by the repulsive mean field interaction.

While this is an instructive picture, one should keep in mind that this "flip" is mostly a change in the point of view of the description. The physical system exhibits a smooth crossover between these two regimes (see also Fig. 2.4). Therefore it can be useful to divide the BEC-BCS crossover into three regimes instead of two: The BCS-regime for $k_F|a| < 1$, the resonance region with $k_F|a| \geq 1$ and the BEC-regime with $na^3 < 1$.

2.8.2 Experiments in the BEC-BCS crossover

The first step on the way to experimentally studying this crossover was the observation of the anisotropic expansion of an ultracold Fermi gas with resonant

interactions [O’H02], which showed that the system could be brought into the strongly interacting regime.

After the properties of the universal dimers had been understood in a series of theoretical and experimental works [Reg03, Joc03a, Cub03, Str03, Reg04, Pet04, Chi04b], molecular BECs were produced almost simultaneously in several experiments [Joc03b, Gre03, Zwi03]. The next step was to study the evolution of the system across the entire crossover by mapping the cloud size as a function of interaction strength [Bar04b].

However, there was still the big question whether the created systems were actually superfluid, and how the critical temperature for superfluidity would behave across the crossover. To study these (and other) questions the system was probed in a number of different ways. One was to excite collective oscillations in the cloud [Bar04a, Kin04] and extract information about the system from the observed frequency and damping of the oscillation. Another method was to study the properties of the molecules [Reg03, Bar05] on the BEC side of the resonance as well as BCS-like pairs on the BCS side [Chi04a, Sch08c, Sch08a] using RF-spectroscopy.¹³ We will discuss this technique in detail in the context of the RF-association of Efimov Trimers in chapter 6.

The first definite proof for superfluidity in an ultracold Fermi gas was provided by M. Zwerlein et al., who were able to create vortex lattices by rotating Fermi gases in a cylindrical trap [Zwi05, Sch07]. They managed to observe these vortex lattices for interaction strengths between $-0.8 < 1/k_F a < 1.5$, thus showing that superfluidity persists across the BEC-BCS crossover. This was an impressive experimental achievement, which has not been reproduced by any other research group so far.

One should note that it has not been possible to reach the actual BEC and BCS limits in these experiments, all experiments are performed with at least moderately large interactions. On the BEC side the dimers become unstable against two-body collisions when a is not much larger than r_0 , while in the BCS limit T_c is so low that it cannot be reached with current cooling techniques.

Pairing in imbalanced Fermi gases

One particularly interesting aspect of strongly interacting Fermi gases, which will also become relevant in chapters 5 and 6, is the case of imbalanced spin populations. Once again, this is a question that had already been studied theoretically in the context of condensed matter physics long ago, but could not be experimentally realized in these systems [Clo62]. When it was realized in strongly

¹³[Bar05] is of special importance for the ${}^6\text{Li}$ system, as it fixed the parameters of the ${}^6\text{Li}$ Feshbach resonances with high precision. Before these measurements the positions of these resonances had an uncertainty of several tens of Gauss [Bou03, Die02, Zwi04, Hou98].

interacting Fermi gases, it was observed that below a certain critical imbalance (the so-called Clogston limit) the system separates into a fully paired, superfluid core and an outer shell of unpaired fermions in the normal (i.e. non-superfluid) state [Zwi06c, Zwi06b, Shi06, Par06]. For imbalances above the Clogston limit superfluidity breaks down and the system enters the normal phase.

For a gas which is deeply in the molecular regime this manifests itself as a separation of the gas into a molecular BEC in the trap center surrounded by a cloud of fermionic atoms which cannot enter the BEC due to its repulsive mean field. Examples for this are shown in figure 2.8.

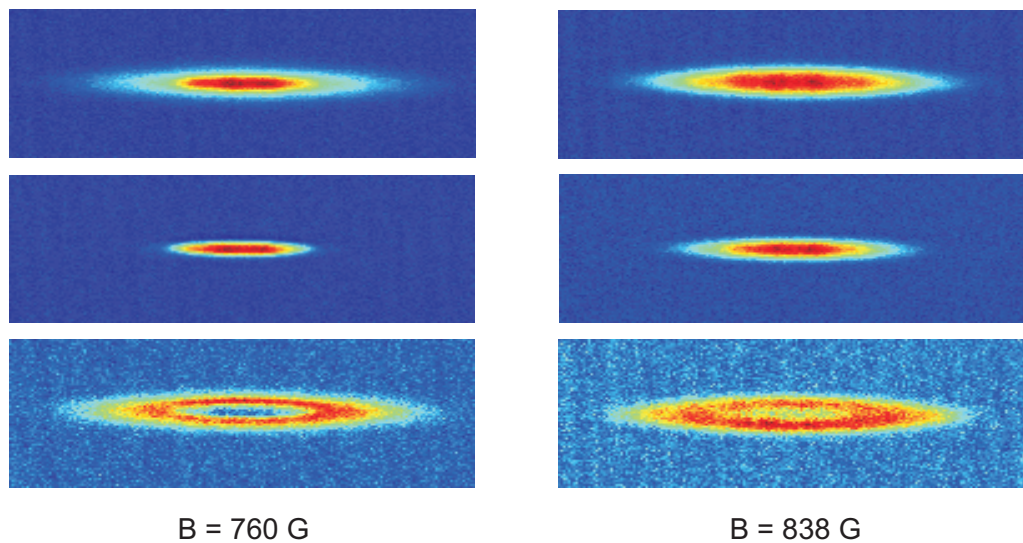


Figure 2.8: Absorption images of an imbalanced two-component Fermi gas in the BEC-regime (left) and close to resonance (right). The images show the density of atoms and molecules integrated along the imaging axis. The upper images show the density of the majority (top) and minority (center) component. The density difference, which was obtained by subtracting the two upper images from each other, is shown in the bottom panels. The suppression of the density difference in the center of the cloud is clearly visible, which indicates the separation into a core of pairs surrounded by a shell of unpaired atoms. All images are the average of twenty individual measurements.

2.9 Adding a third component

Adding a third component lets ultracold Fermi gases step out of the shadow of condensed matter physics. While two-component Fermi gases possess quite strong

strong conceptual similarities to a system of spin $|\uparrow\rangle$ and $|\downarrow\rangle$ electrons, a three-component Fermi gas has a completely different symmetry from these systems. A two-component Fermi gas has an $SU(2)$ symmetry, i.e. the system is invariant under the exchange of spin $|\uparrow\rangle$ and $|\downarrow\rangle$. In contrast, a three-component Fermi gas with equal interparticle scattering lengths $a_{12} = a_{23} = a_{13} = a$ has an $SU(3)$ symmetry. This is the same symmetry as for the color charge in QCD, therefore it is natural to assign three colors to the spin states. However, one should keep in mind that the van-der-Waals interactions between ultracold atoms are electromagnetic and therefore very different from the interactions between quarks, which interact via the exchange bosons of the strong force, the gluons.¹⁴

For weak attractive interactions the ground state of the system is predicted to be BCS-like, where it is energetically favorable to fully pair up two components, while the third remains a spectator [Rap07, Paa06]. However, for equal scattering lengths and densities for all components none of the three possible realizations of this ground state is preferred. This leads to a spontaneous breaking of the $SU(3)$ symmetry to an $SU(2)\times U(1)$ symmetry as two random components form Cooper pairs. In analogy to color superconductors, which have been discussed in the context of QCD at high net baryon density, these states are called color superfluids [Rap07]. Other examples for such a spontaneous symmetry breaking are the appearance of ferromagnetic order in solids being cooled below their Curie temperature and the Higgs mechanism in the standard model.

One interesting question is what the BEC-BCS crossover would look like in such a system. In principle one could expect it to be very similar to the two-component case: The Cooper pairs smoothly turn into molecules, while the third component remains a spectator during the whole crossover. However, this picture neglects the fact that the few-body physics of the system are also fundamentally different from the two-component case. As there are distinguishable fermions, three-body collisions are no longer suppressed by Pauli blocking. This leads to a drastically decreased stability of the gas, a problem whose impact we will discuss in chapter 7. On the other hand three-body bound states with s -wave symmetry are now allowed as well. For resonant interactions this leads to the appearance of universal three-body bound states, the so-called Efimov trimers (see chapter 3). These trimers become the new ground state of the system, thus "interrupting" the BEC-BCS crossover (see Fig. 2.9). If all scattering lengths are equal, these trimers have an $SU(3)$ symmetry. Thus changing the system from a color superfluid with an $SU(2)\times U(1)$ symmetry via a gas of trimers to an atom-dimer mixture on the BEC side, which again has a $SU(2)\times U(1)$ symmetry should involve two phase transi-

¹⁴While the low-energy behavior of nucleons – which also interact via the strong force – can be described with a scattering length, this is not the case for free quarks because their interaction potential does not have a finite range. (Confirm this or leave it out!)

tions. This is a completely different behavior than the BEC-BCS crossover in a two-component system. However, as we will see in chapters 3 and 5 the trimers are actually quite unstable, so it seems improbable that it will be possible to realize this specific scenario experimentally.

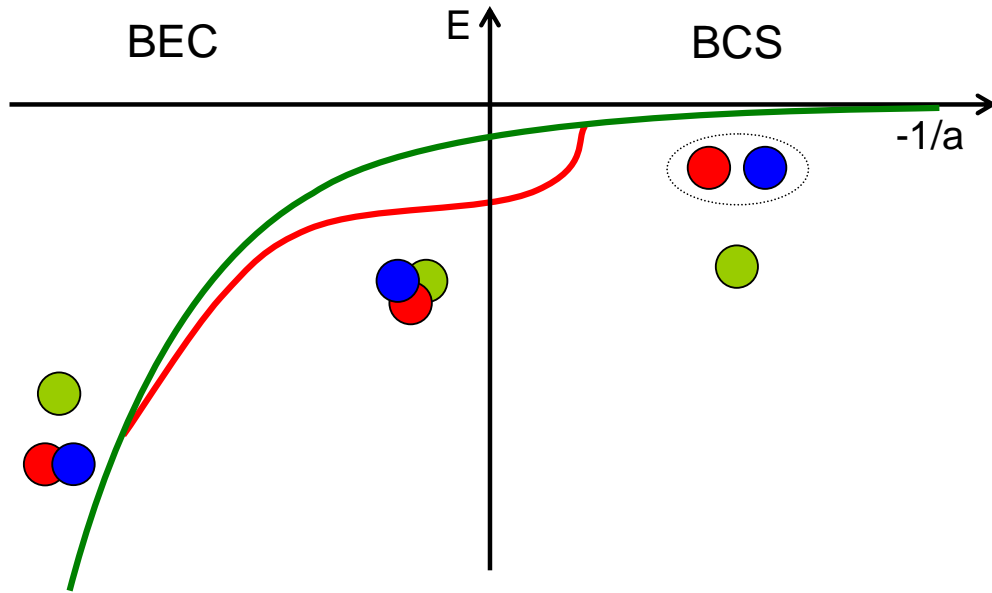


Figure 2.9: Sketch of the BEC-BCS crossover for three components. The energy of the system is plotted for the case of two-body (green line) and three-body pairing (red line) as a function of $-1/a$. (We use the inverse scattering length, as this makes plotting the resonance region where $a \rightarrow \pm\infty$ much more convenient. The minus sign causes the BEC side of the resonance to sit on the left side of the graph, as it does when plotting the ${}^6\text{Li}$ scattering lengths as a function of magnetic field.) For a small and negative scattering length the ground state of the system is a color superfluid consisting of BCS-like pairs and unpaired atoms. If the scattering length is large enough, there is a universal trimer state in the system which becomes the new ground state. For small and positive scattering length the system consists of a mixture of bosonic molecules and free fermionic atoms.

Another interesting question is whether a three-component Fermi gas which has not formed trimers is actually stable for $a \rightarrow -\infty$. In the two-component Fermi gas it has been shown that attractive interactions and Fermi pressure form an equilibrium, with the size of the system rescaled by the universal constant $(1 - \beta) \approx 0.42$ (see Sect. 2.8). By increasing the number of components one effectively decreases the ratio between Fermi pressure and attractive interactions. For a system

with an infinite number of components – i.e. every atom is distinguishable from any other atom – there is no Fermi pressure and the system will collapse, similar to a BEC with attractive interactions. This suggests that somewhere between two and infinity there should be a critical number of components for which the gas becomes unstable. As this number has been predicted to lie somewhere between two and three components [Hei01, Blu08] such a collapse might be observable in a three-component Fermi gas with resonant interactions.

If the three scattering lengths do not have the same value there is no spontaneous symmetry breaking as the SU(3) symmetry is already broken. In this case the two components with the strongest interparticle attraction pair up. If there are overlapping Feshbach resonances between the three components – as it is the case in ${}^6\text{Li}$ – one can change which two components feel the strongest attraction towards each other by changing the magnetic field. Doing this should cause the system to reorganize itself into the new ground state. A theoretical study which also included the effect of the trapping potential predicted that inside a trap the sample separates into a paired core and an outer shell of unpaired atoms, or into several regions of different pairs and unpaired atoms [Paa07].

As we have seen in the previous section, understanding the behavior of the universal dimers was the key to exploring the many-body physics of the two-component system. Therefore the natural next step after creating a three-component Fermi gas was to study the few-body physics of the system, especially the universal trimer states. These studies are detailed in chapters 5 and 6. With this knowledge we can then formulate an approach to studying the many-body physics of three-component Fermi gases, which we will do in chapter 7.

Chapter 3

The Efimov effect

In this chapter we will discuss the Efimov effect, and how it affects the behavior of an ultracold gas with resonant interactions (i.e. $a \gg r_0$). The chapter starts with a qualitative description of Efimov's scenario for a few-body system of three identical bosons. This allows us to introduce some key concepts of Efimov physics using the simplest available system as an example. Next, we examine the influence of the Efimov trimers on some key properties of the system, such as the rate constants for three-body recombination and the scattering between atoms and dimers. Then we will discuss changes that occur for the case of distinguishable particles with large interparticle scattering lengths that we studied in our experiment. The chapter closes with a brief review of the experimental studies of Efimov physics that have been performed in the past five years.

3.1 Efimov's scenario for three identical bosons

During our discussion of two-body scattering in chapter 2 we found that for sufficiently low momenta ($k \ll 1/r_0$) we could put the effect of all short-range physics into a single parameter - the scattering length a - and the low-energy physics of the system becomes universal. This even applies to bound states, as long as the size of the dimers is much larger than the range of the interatomic potential. For a long time, theorists have been working on extending this concept of universality to a three-body system. One example is the calculation of the atom-dimer scattering length given in Eq. 2.39, which was first done in the context of nuclear physics to describe low-energy neutron-deuteron scattering [Sko57]. In 1970, V. Efimov studied a system of three particles with equal scattering lengths in the zero-energy ($k \rightarrow 0$) and zero-range ($r_0 \rightarrow 0$) limit [Efi71, Efi70]. If a two-body bound state crosses into the continuum, the scattering length diverges at a two-body scatter-

ing resonance (see Sect. 2.4).¹ Around this scattering resonance there is a series of universal three-body bound states. For negative scattering length these bound states disappear into the three-atom continuum when their binding energies become degenerate with the energy of three free atoms. On the other side of the resonance the trimer states disappear when their binding energy becomes degenerate with the energy of an atom and a dimer (i. e. they hit the atom-dimer threshold) (see Fig. 3.1). The intersections of such a trimer state with the three-atom and atom-dimer continuum occur at specific values a_*^- and a_*^+ of the two-body scattering length, which are related by $a_*^- \approx 22 a_*^+$.

These three-body bound states exhibit a discrete scaling symmetry, i.e. they are self-similar under a rescaling of all length scales by a discrete scaling factor e^{π/s_0} . For a system of three identical bosons $s_0 \approx 1.00624$, so the system looks the same after a magnification by a factor of ~ 22.7 . Consequently, if a trimer state crosses the three-atom continuum at a scattering length $a = a_*^-$, increasing the scattering length by this factor to $e^{\pi/s_0} a_*^-$ causes a new trimer state to appear in the system (see Fig. 3.1). For $a \rightarrow \pm\infty$ there is an infinite series of such trimer states in the system.

So far we have only discussed the shape and periodicity of these trimer states, however there is still one free parameter which defines the overall offset of the series. This is the so-called three-body parameter, which describes the effect of short-range three-body interactions on the long-range three-body physics. As it describes short-range physics, this three-body parameter necessarily depends on the specifics of the system and is therefore non-universal. This is very similar to the way the scattering length describes the effects of a short-range two-body potential on the long-distance behavior of the two-body system. Due to the discrete scaling symmetry mentioned above, the three-body parameter is only defined modulo e^{π/s_0} . It can be defined in a number of different ways. One choice is to define a wavenumber κ_* from the binding energy

$$E_T^n = \frac{\hbar^2 \kappa_*^2}{2m} (e^{2\pi/s_0})^n \quad (3.1)$$

of a trimer on resonance, which scales as 22.7^2 with the position of the trimer state in the series. In experiments it is convenient to express the three-body parameter in terms of a measured quantity, which is usually a scattering length a_*^- or a_*^+ at which a trimer state becomes degenerate with the three-atom or atom-dimer continuum.

For small length scales (or equivalently: high energies) universality breaks down and Efimov's scenario is no longer valid. The "window of universality" in which

¹In our experiments this is a Feshbach resonance, but for Efimov's scenario the origin of the scattering resonance is actually irrelevant.

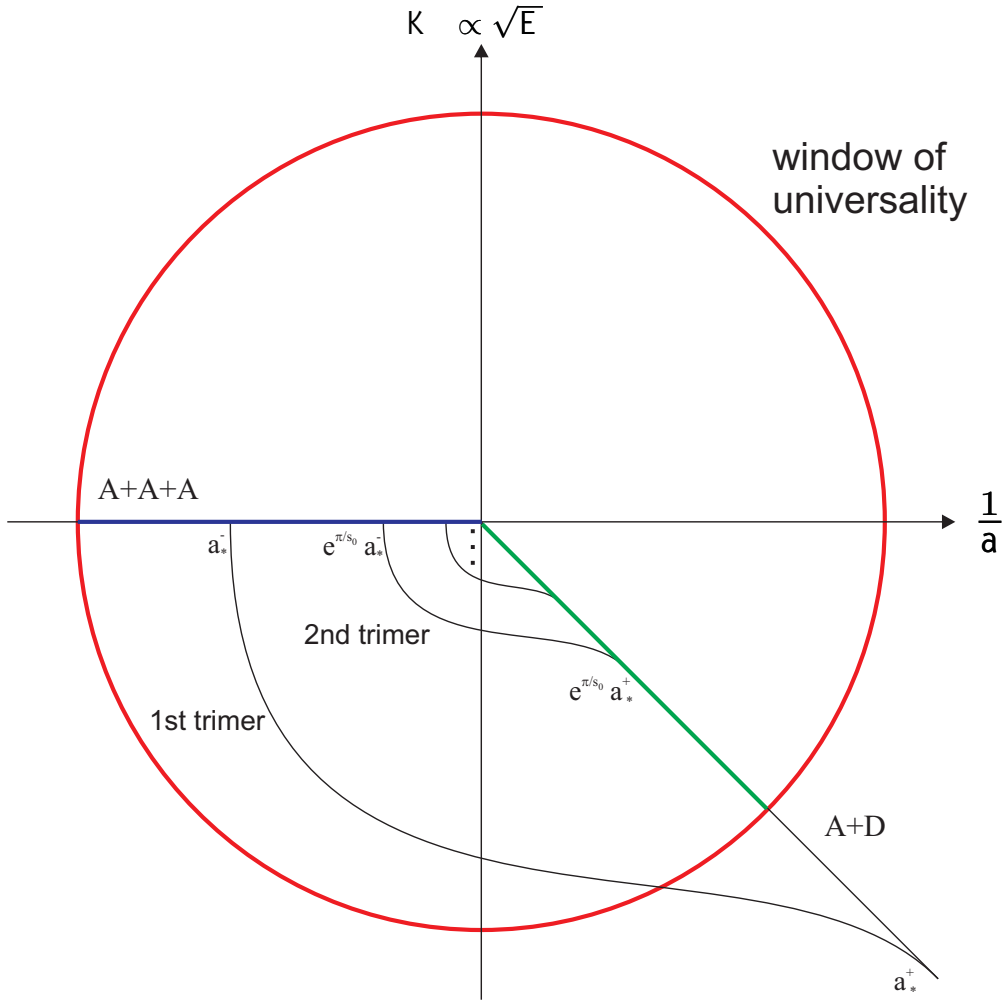


Figure 3.1: Sketch of Efimov's scenario for the case of three identical bosons. The wavenumber K (which is proportional to the square root of the total energy of the system, see Eq. 3.3) is plotted against the inverse scattering length $1/a$. The dissociation threshold of the Efimov trimers at the three-atom continuum at $K = 0$ is indicated by the blue line. The red circle shows the border of the region where universal theory is applicable. The binding energy of the universal dimer, which also marks the beginning of the atom-dimer continuum is given by the green line. The binding energies of the trimer states are shown as solid back lines. The first trimer state intersects with the three-atom and atom-dimer thresholds at critical scattering lengths a_*^- and a_*^+ ; for the second trimer these critical scattering lengths are larger by the universal scaling factor $e^{\pi/s_0} \approx 22.7$. Due to this geometric scaling there is an infinite number of trimer states for $1/a \rightarrow 0$. To better visualize the trimer states the scaling factor was reduced to ~ 2 in this sketch.

it applies is given by the condition

$$\sqrt{K^2 + (1/a)^2} \leq 1/r_0, \quad (3.2)$$

where

$$K = \text{sign}(E) \sqrt{\frac{m|E|}{\hbar^2}} \quad (3.3)$$

is a wavenumber corresponding to the kinetic or binding energy of the particles. Therefore all theories describing the Efimov effect contain a cutoff at a small distance of order r_0 .²

One important question is how these trimer states affect an ultracold gas. Let us first look at the points where the energy of a trimer becomes degenerate with the atom-dimer continuum. Close to these points, the trimer looks like a weakly bound state of a dimer and a third atom. In this case the binding energy of this atom-dimer system is given by Eq. 2.14. If we only consider elastic scattering we can turn Eq. 2.14 around and use the difference between the trimer and dimer binding energies ($E_T - E_D$) to calculate the atom-dimer scattering length

$$a_{AD} = \sqrt{\frac{\hbar^2}{2\mu(E_T - E_D)}}, \quad (3.4)$$

where μ is the reduced mass of the atom-dimer system. At the point where the trimer crosses into the atom-dimer continuum $E_T = E_D$ and there is a zero-energy scattering resonance in the atom-dimer scattering. One should note that this is not a Feshbach resonance, but a zero-energy scattering resonance as it was discussed in Sect. 2.4.

As there are deeply bound dimer states in our system, the universal dimers can relax into these deeply bound dimers in atom-dimer collisions.³ In the vicinity of an atom-dimer scattering resonance the rate constant for this process is enhanced, which can serve as an experimental signature for the crossing of an Efimov state with the atom-dimer continuum.⁴

At the point where the trimer hits the three-atom threshold there is a resonance in the three-body scattering, which leads to an enhanced rate of three-body collisions. Some fraction of these three-atom collisions lead to recombination into deeply bound dimer states. This causes an enhancement of inelastic three-body collisions, which was used to make the first observation of an Efimov state [Kra06].

²In some theories the description actually depends on the value of this cutoff, in this case the cutoff takes the role of the three-body parameter.

³A deeply bound dimer is a dimer whose size is smaller than r_0 and which is consequently not described by Eq. 2.14.

⁴In principle it should also be possible to observe this resonance in the elastic scattering, this will be discussed in Section 7.1.

While we have given a phenomenological introduction of the Efimov effect in this section, understanding its origin requires a closer look at the theory of three-body collisions. This will be done in the following sections.

3.2 Hyperspherical treatment of the three-body problem

While the Efimov effect can be described in many different theoretical frameworks, such as effective field theory or functional renormalization group methods, we will focus on the hyperspherical approach in this chapter. This approach has the advantage that it allows for a quite instructive description of the three-body problem in terms of hyperspherical potentials. In our description of this approach we will follow the excellent review by E. Braaten and H. W. Hammer [Bra06]. In principle, solving the quantum-mechanical three-body problem can be done by solving the Schrödinger equation

$$\left(-\frac{\hbar^2}{2m} \sum_{i=1}^3 \nabla_i^2 + V(\mathbf{r}_1, \mathbf{r}_2, \mathbf{r}_3) \right) \psi(\mathbf{r}_1, \mathbf{r}_2, \mathbf{r}_3) = E\psi(\mathbf{r}_1, \mathbf{r}_2, \mathbf{r}_3) \quad (3.5)$$

for the wavefunction of three particles $\psi(\mathbf{r}_1, \mathbf{r}_2, \mathbf{r}_3)$ which interact via an interaction potential $V(\mathbf{r}_1, \mathbf{r}_2, \mathbf{r}_3)$. This problem has nine degrees of freedom, which can be reduced to six by separating the center of mass motion.

This rather difficult task can be simplified by a transformation into a set of coordinates more appropriate to the problem. These are the so-called hyperspherical coordinates which we will define below.

3.2.1 The hyperspherical coordinates

After transformation into the center of mass frame, the system depends only on the relative positions of the three atoms. These can be described by the Jacobi coordinates

$$\mathbf{r}_{ij} = \mathbf{r}_i - \mathbf{r}_j \quad \text{and} \quad \mathbf{r}_{k,ij} = \mathbf{r}_k - \frac{1}{2}(\mathbf{r}_i + \mathbf{r}_j); \quad (3.6)$$

an example for one possible set of these coordinates is given in Fig. 3.2.

Using hyperspherical coordinates allows to express these relative coordinates in a way that directly shows some key properties of the three-body system, which greatly simplifies the theoretical description. The first coordinate is the hyperradius R , which is defined as the root-mean-square separation of the atoms

$$R = \frac{1}{3} \sqrt{r_{12}^2 + r_{23}^2 + r_{13}^2}. \quad (3.7)$$

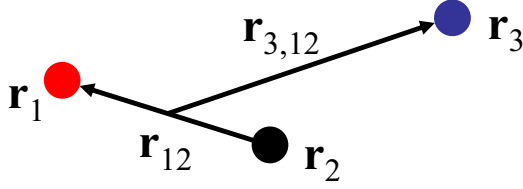


Figure 3.2: One of the three possible sets of Jacobi coordinates for a three-particle system. \mathbf{r}_{12} describes the relative positions of particles 1 and 2, while $\mathbf{r}_{3,12}$ gives the position of the third particle relative to their center of mass.

This is a very useful quantity, as it gives an intuitive measure of the extension of the three-particle system: If R is large, the particles are generally farther apart, but if R is small the particles are close together.

The second parameter is one of the Delves hyperangles [Del60]

$$\alpha_k = \arctan \frac{\sqrt{3}r_{ij}}{2r_{k,ij}} \in [0, \pi/2), \quad (3.8)$$

which contains information about the position of one particle relative to the center of mass of the other two particles. For a configuration where the particles i and j are close together and the third is far away from this pair the hyperangle $\alpha_k \rightarrow 0$.⁵ If the third particle sits close to the center-of-mass of the other two particles, $\alpha_k \rightarrow \pi/2$.

After defining these two coordinates we still need four more parameters to fix the relative positions of the particles. These are the unit vectors $\hat{r}_{i,j}$ and $\hat{r}_{k,ij}$ of the Jacobi coordinates defined in Eq. 3.6.⁶ Together with α_k they form a set of five hyperangular variables which are denoted by $\Omega = (\alpha_k, \hat{r}_{i,j}, \hat{r}_{k,ij})$.

Rewriting the Schrödinger equation 3.5 in these coordinates yields

$$\left(T_R + T_{\alpha_k} + \frac{\Lambda_{k,ij}^2}{2mR^2} + V(R, \Omega) \right) \psi(R, \Omega) = E\psi(R, \Omega), \quad (3.9)$$

where T_R and T_{α_k} are the kinetic energy operators for R and α_k respectively, while $\Lambda_{k,ij}$ is a generalized angular momentum operator acting on $\hat{r}_{i,j}$ and $\hat{r}_{k,ij}$. For the definitions of these operators see [Bra06]. Except for the separation of the center of mass motion, this equation is still equivalent to Eq. 3.5. In the next section we

⁵This situation is similar to an Efimov trimer crossing the $|1\rangle - |23\rangle$ atom-dimer threshold as described in chapter 5, where the atoms $|2\rangle$ and $|3\rangle$ are close together while the atom in state $|1\rangle$ is far away from this two-body cluster.

⁶As the unit vectors give the direction but not the length of the vectors defined in Eq. 3.6, each one fixes two degrees of freedom.

will begin to apply simplifications to the three-body problem, which finally lead to the low-energy Faddeev equations.

3.2.2 The Faddeev equations

The first simplification we apply is the assumption that the interaction potential

$$V(\mathbf{r}_1, \mathbf{r}_2, \mathbf{r}_3) = V(\mathbf{r}_{12}) + V(\mathbf{r}_{13}) + V(\mathbf{r}_{23}) \quad (3.10)$$

between the particles can be expressed as a sum of three independent two-body potentials V_{ij} . This neglects any intrinsic three-body interaction between the particles which cannot be expressed as a sum of three pairwise interaction potentials. For a low-energy problem this is a reasonable simplification, as we will later see that the effects of a short-range three-body interaction can be described by a single non-universal constant.⁷

This allows to define a solution of the Schrödinger equation 3.9

$$\psi(\mathbf{r}_1, \mathbf{r}_2, \mathbf{r}_3) = \psi^{(1)}(\mathbf{r}_{23}, \mathbf{r}_{1,23}) + \psi^{(2)}(\mathbf{r}_{13}, \mathbf{r}_{2,13}) + \psi^{(3)}(\mathbf{r}_{12}, \mathbf{r}_{3,12}) \quad (3.11)$$

as the sum of three functions $\psi^{(i)}(\mathbf{r}_{jk}, \mathbf{r}_{1,23})$, which are solutions to the three Faddeev equations

$$\left(T_R + T_{\alpha_k} + \frac{\Lambda_{k,ij}^2}{2mR^2} \right) \psi^{(k)} + V(\mathbf{r}_{ij})(\psi^{(k)} + \psi^{(i)} + \psi^{(j)}) = E\psi^{(k)}. \quad (3.12)$$

As we are interested in a low-energy system, we can safely neglect all terms which involve angular momenta other than zero, which allows us to eliminate the dependence of Eq. 3.12 on the angular momentum operator $\Lambda_{k,ij}$. The wavefunction then reduces to

$$\psi(\mathbf{r}_1, \mathbf{r}_2, \mathbf{r}_3) = \psi(R, \alpha_1) + \psi(R, \alpha_2) + \psi(R, \alpha_3), \quad (3.13)$$

which depends only on R and α_k . As the different hyperangles α_k are not independent of each other we have reduced the number of degrees of freedom by four. The three Faddeev equations can then be combined into a single integro-differential equation depending on R and one of the hyperangles α

$$(T_R + T_\alpha - E) \psi(R, \alpha) = -V(\sqrt{2}R \sin \alpha) \times \left(\psi(R, \alpha) + \frac{4}{\sqrt{3}} \int_{|(1/3)\pi - \alpha|}^{(1/2)\pi - |(1/6)\pi - \alpha|} \frac{\sin(2\alpha')}{\sin(2\alpha)} \psi(R, \alpha') d\alpha' \right), \quad (3.14)$$

⁷By using Eq. 3.10 one loses some information about the system, which in the final description of the Efimov scenario is put back in by experimentally determining the three-body parameter.

which is called the low-energy Fadeev equation [Fed93].

The solution $\psi(R, \alpha)$ to this equation can be expanded into a series of hyperangular functions $\Phi_n(R, \alpha)$ of the form

$$\psi(R, \alpha) = \frac{1}{R^{5/2} \sin(2\alpha)} \sum_n f_n(R) \Phi_n(R, \alpha). \quad (3.15)$$

These functions $\Phi_n(R, \alpha)$ are solutions to an eigenvalue equation

$$\begin{aligned} & - \frac{\partial^2}{\partial \alpha^2} \phi_n(R, \alpha) + \frac{2mR^2}{\hbar^2} V(\sqrt{2} R \sin \alpha) \\ & \times \left(\phi_n(R\alpha) + \frac{4}{\sqrt{3}} \int_{|\pi/3-\alpha|}^{\pi/2-|\pi/6-\alpha|} d\alpha' \phi_n(R, \alpha') \right) = \lambda_n(R) \phi_n(R, \alpha) \end{aligned} \quad (3.16)$$

in α , where we can treat R as a parameter and $\lambda_n(R)$ as a function of this parameter. The R -dependence of these eigenvalues defines a set of potential curves

$$V_n(R) = (\lambda_n(R) - 4) \frac{\hbar^2}{2mR^2}. \quad (3.17)$$

These potential curves $V_n(R)$ describe the scattering potentials that belong to each hyperradial function $\Phi_n(R, \alpha)$.

If we neglect the coupling between different hyperspherical potentials the system is described by a radial Schrödinger equation in the hyperradius R

$$\left[\frac{\hbar^2}{2m} \left(-\frac{\partial^2}{\partial R^2} + \frac{15}{4R^2} \right) + V_n(R) \right] f_n(R) \approx E f_n(R), \quad (3.18)$$

with the hyperradial wavefunctions $f_n(R)$ [Bra06]. With this we have reduced the three-body problem to a one-body problem with one parameter R . All that is left to be done before one can solve this equation is to obtain the eigenvalues $\lambda_n(R)$ by solving Eq. 3.16. The difficulty of this task depends on the form of the interaction potential between the atoms. In the next section we will discuss this for the case of three particles with short-range two-body potentials described by a scattering length $a \gg r_0$.

3.2.3 Hyperspherical potentials and the Efimov effect

If the two-body interactions between the three particles are described by a scattering length $a \gg r_0$, the hyperspherical potentials $V_n(R)$ needed to solve Eq. 3.18 can be calculated numerically [Bra06]. The three lowest hyperspherical potentials for $a < 0$ and $a > 0$ are plotted in Fig. 3.3 as a function of R/a . Only

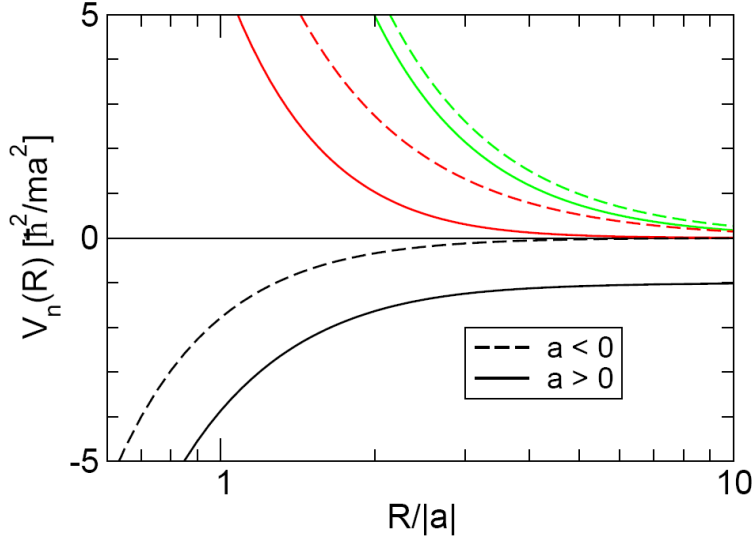


Figure 3.3: Hyperspherical potential curves $V_n(R)$ for $n \leq 2$ as a function of R/a . Only the lowest potential $V_n(R)$ (black) is attractive and supports bound states. All potentials except for the attractive potential for $a > 0$ go to zero energy for $R \rightarrow \infty$, which corresponds to the scattering continuum of three free particles. For positive scattering length the lowest hyperspherical potential converges to the energy of the universal dimer \hbar^2/ma^2 . This can be understood as a scattering state of a dimer and a free atom. Figure taken from [Bra06].

the lowest potentials are attractive, while all potentials with $n \geq 1$ are repulsive. Consequently, only the lowest potentials can support three-body bound states. One should note that Eq. 3.18 only gives a good description of the system if $r_0 \ll R \ll a$. At short distances $R < r_0$ there is high-energy physics, which we neglected in the derivation of Eq. 3.15. For $R \sim a$ the coupling between the different hyperspherical potentials can no longer be ignored and Eq. 3.18 becomes invalid.

Let us consider a system in the zero-range ($r_0 \rightarrow 0$) and resonant ($a \rightarrow \infty$) limits. For $R/a \rightarrow 0$ the eigenvalues $\lambda_n(R)$ of Eq. 3.16 approach a constant value, which for the lowest potential has been calculated to [Bra06]

$$\lambda_0(R) \rightarrow -s_0^2 \left(1 + 1.897 \frac{R}{a} \right). \quad (3.19)$$

Inserting this eigenvalue into Eq. 3.17 and putting the resulting potential into Eq. 3.18 leads to the following equation

$$\frac{\hbar^2}{2m} \left[-\frac{\partial^2}{\partial R^2} - \frac{s_0^2 + 1/4}{R^2} \right] f_0(R) = E f_0(R), \quad (3.20)$$

which has the form of a Schrödinger equation of a particle in a $1/r^2$ potential. Such an $1/r^2$ potential is long range, i.e. it supports an infinite number of bound states. The energy of these bound states is given by the solutions

$$E_T^{(n)} = \left(e^{-2\pi/s_0}\right)^{n-n_*} \frac{\hbar^2 \kappa_*^2}{m} \quad (3.21)$$

of Eq. 3.20. Thus we have confirmed our claim from the previous section that in a three-particle system with infinite two-body scattering lengths there is an infinite series of three-body bound states, whose binding energies are spaced by a factor $e^{-2\pi/s_0} \approx 1/515$.

For a system with a finite r_0 , the three-body wavefunction depends on the details of the interaction potential at short distances, which is generally very complicated. Therefore one has to include a cutoff at a distance of $\sim r_0$. However, the solutions of Eq. 3.20 have to match this short-range part of the wavefunction, which can be achieved by choosing an appropriate value of the cutoff. This value defines the position of the lowest Efimov trimer. This short-range cutoff is therefore the origin of the three-body parameter, which describes the effect of the short-range physics on the series of Efimov trimers.

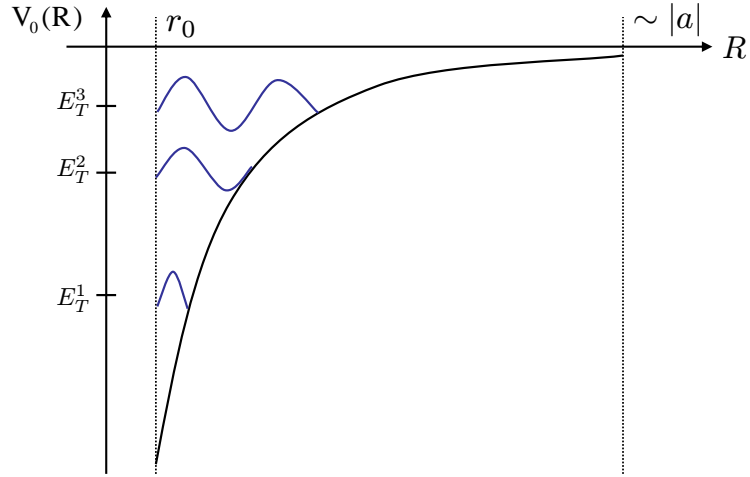


Figure 3.4: Sketch of the Efimov states in the the lowest hyperspherical potential. The borders of the validity of Eq. 3.18 at $R \sim r_0$ and $R \sim a$ are marked by the dotted lines. For $a \rightarrow \infty$ there is an infinite number of bound states in this $1/r^2$ potential. To enhance visibility, the scaling factor was reduced from ~ 515 to ~ 2 .

3.3 Efimov's radial law

In the previous section we have looked at the situation in the resonant limit $a \rightarrow \infty$. Now we will discuss Efimov's radial law [Ef79], which allows to calculate quantities such as the trimer binding energy and rates for three-body recombination in the whole resonant region $a \gg r_0$. This law is based on simple arguments of probability conservation. We will first discuss the case of a system without deeply bound dimer states and include the effects of deep dimers later on.

As a first step it is useful to separate the problem into four regions depending on the value of the hyperradius R :

- The first is the asymptotic region $R \gg |a|$: In this region the effect of the interaction potential vanishes. Therefore it is straightforward to write down free-particle three-atom and atom-dimer wavefunctions $|AAA\rangle$ and $|AD\rangle$ which describe the asymptotic behavior of the particles for $R \rightarrow \infty$
- In the long-distance region $R \sim |a|$ the wavefunction can be quite complicated and is not easy to solve. It is in this region where the couplings between the different hyperspherical potentials are most important (see Sect. 3.2.2).
- In the scale-invariant region $r_0 \ll R \ll |a|$ the wavefunction is well-approximated by a hyperradial wave according to Eq. 3.18, which is straightforward to solve.
- Last is the short-distance region $R \sim r_0$, where the wavefunction depends on the short-range characteristics of the interaction potential. These are usually not known well enough to calculate the wavefunction in this region.

In conclusion, we have two regions ($R \gg |a|$ and $r_0 \ll R \ll |a|$) where we know the structure of the wavefunction, and two where we do not ($R \sim |a|$ and $R \sim r_0$). Let us consider a scattering event which begins with either three incoming atoms with a wavefunction $|AAA\rangle_{in}$ or an incoming atom and dimer with wavefunction $|AD\rangle_{in}$. As we have assumed elastic scattering, it is possible to describe the scattering process by a unitary 2×2 s-matrix

$$S = \begin{pmatrix} S_{AAA,AAA} & S_{AAA,AD} \\ S_{AD,AAA} & S_{AD,AD} \end{pmatrix}, \quad (3.22)$$

which gives the probability for incoming three-atom and atom-dimer states $|AAA\rangle_{in}$ and $|AD\rangle_{in}$ to turn into outgoing three-atom and atom-dimer states $|AAA\rangle_{out}$ and $|AD\rangle_{out}$ according to the equation

$$\begin{pmatrix} S_{AAA,AAA} & S_{AAA,AD} \\ S_{AD,AAA} & S_{AD,AD} \end{pmatrix} \begin{pmatrix} |AAA\rangle_{in} \\ |AD\rangle_{in} \end{pmatrix} = \begin{pmatrix} |AAA\rangle_{out} \\ |AD\rangle_{out} \end{pmatrix}. \quad (3.23)$$

Here $S_{AAA,AAA}$ and $S_{AD,AD}$ give the probability for elastic three-atom and atom-dimer scattering, while the off-diagonal elements $S_{AD,AAA} = S_{AAA,AD}$ give the probability for forming and dissociating shallow dimers in three-atom and atom-dimer collisions.⁸

To calculate these matrix elements one could in principle calculate the evolution of the wavefunction as it passes through the long-distance, scale-invariant and short-distance regions. While this can be done for the scale-invariant region, it is very hard for the long- and short-range regions. However, as probability has to be conserved one can simply consider the evolution of the wavefunction in the long-distance region as a unitary 3×3 matrix

$$s_{ij} = |i, out\rangle \hat{U} \langle j, in|, \quad (3.24)$$

whose entries are given by the transition probabilities between

(i,j = 1): hyperradial waves in the scale-invariant region

(i,j = 2): asymptotic atom-dimer states

(i,j = 3): asymptotic three-atom states.

These are determined by a unitary evolution operator \hat{U} , which describes the effect of the long-distance region on the wavefunction. s_{11} , s_{22} and s_{33} describe the reflection of hyperradial waves, atom-dimer and three-atom states at the long-distance regions, while the off-diagonal elements describe the couplings between the different in- and outgoing states.

For the short-distance region things are even simpler: In the absence of deep dimers, hyperradial waves entering the short-distance region can only acquire a phase shift θ_* .

From these considerations we can now write down the different elements of S :

$$S_{AAA,AAA} = s_{33} + s_{31} e^{2i\theta_*} \frac{1}{1 - e^{2i\theta_*} s_{11}} s_{13} \quad (3.25)$$

$$S_{AD,AD} = s_{22} + s_{21} e^{2i\theta_*} \frac{1}{1 - e^{2i\theta_*} s_{11}} s_{12} \quad (3.26)$$

$$S_{AD,AAA} = s_{23} + s_{21} e^{2i\theta_*} \frac{1}{1 - e^{2i\theta_*} s_{11}} s_{13} \quad (3.27)$$

In each of these equations the first terms originates from the direct reflection at the long-distance region, while the second term is the limit of a sum over multiple reflections of the hyperradial wave on the long- and short-distance regions. An

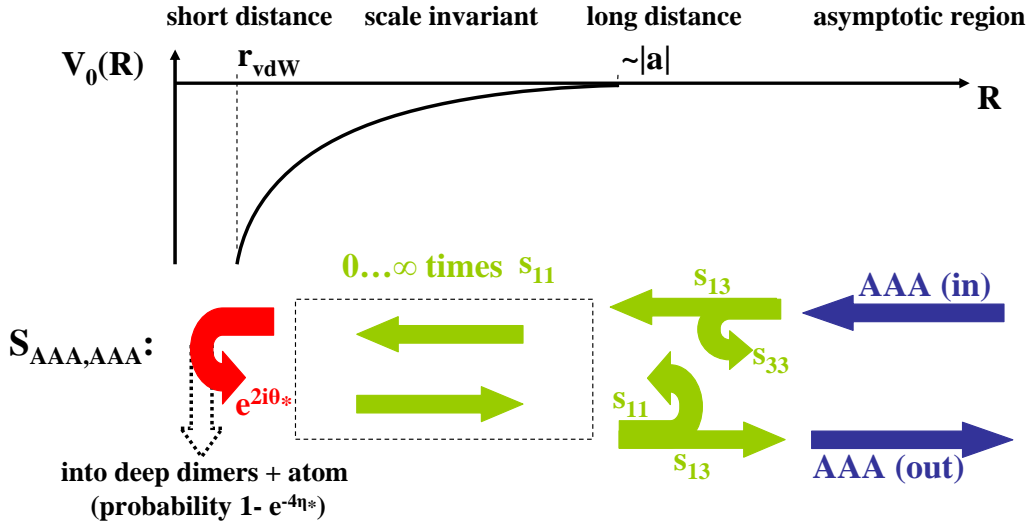


Figure 3.5: Illustration of the s-matrix element $S_{AAA,AAA}$ given in Eq. 3.25. The incoming three-atom state is either transmitted or reflected at the long distance region, the probabilities for these outcomes are given by the matrix elements s_{13} and s_{33} respectively. The transmitted part turns into a hyperradial wave in the scale-invariant region, which is reflected at the short-distance region. During this reflection the hyperradial wave acquires a phase shift θ_* . The returning hyperradial wave is either transmitted (s_{31}) or reflected (s_{11}) at the long-distance region. If there are deeply bound dimers in the system, the hyperradial wave can couple to these deeply bound dimers in the short-distance region, which leads to an inelastic decay into one of the deep dimers and a free atom. The strength of this coupling depends on the non-universal properties of the deep dimers and is described by a non-universal parameter η_* .

example for three-atom scattering at negative scattering length (i.e. without a shallow dimer state in the system) is shown in Fig. 3.5.

If one wants to describe a system of real atoms, one has to include inelastic decay into deeply bound dimers. As these dimer states are small, this decay can only occur in the short-distance region. The strength of the couplings to these deep dimers depends on short-range physics and is therefore not known. However, the effect of these inelastic processes on the three-body scattering can be included by adding a loss channel to the short-range region. This channel gives a probability of $1 - e^{-4\eta_*}$ to decay into a deep dimer on each reflection of the hyperradial wave at the short-range region. This parameter η_* , which is called the inelasticity

⁸In regions of Fig. 3.1 where three-atom or atom-dimer states are energetically forbidden, the corresponding matrix elements are necessarily zero.

parameter, usually has to be determined experimentally.

Using the result for the s-matrix elements given above, it is possible to determine scattering properties such as the formation rate for shallow dimers, the rate constant for three-body loss in three-atom collisions or the rate of elastic and inelastic atom-dimer collisions for the entire resonant region $|a| \gg r_0$ by calculating the phase θ_* and the matrix elements s_{ij} . It also allows to calculate properties not directly related to scattering, such as the binding energy of the Efimov trimers.

3.3.1 Binding energies of Efimov states

To calculate quantities like the binding energies of the Efimov trimers it is useful to introduce new coordinates H and ξ , which were defined by V. Efimov as [Efi79]

$$1/a = H \cos \xi, \quad K = H \sin \xi, \quad (3.28)$$

where K is the wavenumber defined in Eq. 3.3. The meaning of these coordinates can be understood best if one takes another look at Fig. 3.1: They are polar coordinates around the point $(1/a = 0, K = 0)$ with H as radial and ξ as angular coordinate.

In these coordinates, the phase shift θ_* acquired in the short-distance region only depends on H and a three-body parameter Λ_0 and is given by [Bra06]

$$\theta_* = -s_0 \ln(cH/\Lambda_0), \quad (3.29)$$

where c is a numerical constant and $s_0 \approx 1.00624$ is the scaling parameter introduced in Section 3.1. On the other hand, the matrix elements s_{ij} only depend on ξ . This means that in these coordinates calculating the matrix elements of S is reduced to calculating a few universal functions of ξ .

To determine the binding energies of the Efimov trimers one can use the condition that the phase obtained by a hyperradial wave during one round-trip between the long- and short distance region has to be a multiple of π for a standing wave - and therefore a bound state - to occur. As the bound states occur in a region of Fig. 3.1 where neither asymptotic three-atom or atom-dimer states are allowed, the hyperradial wave only acquires a phase shift $\Delta(\xi)$ during the reflection at the long-distance region. Consequently, the binding energy depends on the two phase shifts θ_* and $\Delta(\xi)$. It was calculated by V. Efimov to be

$$E_T + \frac{\hbar^2}{ma^2} = (e^{-2\pi/s_0})^{(n-n_*)} \exp(\Delta(\xi)/s_0) \frac{\hbar^2 \kappa_*^2}{m}. \quad (3.30)$$

The universal function $\Delta(\xi)$ has been calculated in numerous ways. A set of simple parameterizations for $\Delta(\xi)$ can be found in [Bra06].

By evaluating Eq. 3.30 at the value of ξ corresponding to the three-atom threshold one can find a universal relation

$$a_*^- \approx -1.56(5) \kappa_* \quad (3.31)$$

between the binding wavenumber of the Efimov trimer on resonance κ_* and the value a_*^- of the scattering length at which the trimer crosses into the three-atom continuum. For the crossing of the trimer states with the atom-dimer threshold one finds

$$a_*^+ \approx 0.0707645 \kappa_*. \quad (3.32)$$

This leads to a ratio

$$a_*^-/a_*^+ \approx 22.0. \quad (3.33)$$

For a finite value of η_* , the hyperspherical wave has a probability of $1 - e^{-4\eta_*}$ to decay into a deep dimer for each "bounce" off the short-range region. This finite lifetime leads to a finite width Γ_T of the trimer state. For very small values of η_* this width can be approximated by [Bra06]

$$\Gamma_T \approx \frac{4\eta_*}{s_0} \left(E_T + \frac{\hbar^2}{ma^2} \right). \quad (3.34)$$

From this equation we can directly see that the lifetime of Efimov trimers increases geometrically for shallower trimer states. This will become important for the RF-association of Efimov trimers discussed in chapter 6.

3.4 Scattering properties

The main observable for studying Efimov physics in ultracold gases has been the effect of the Efimov states on the (inelastic) scattering properties of the particles. In this section we briefly introduce some analytic formulas that have been calculated for three-atom and atom-dimer scattering in a system of identical bosons. While the situation is somewhat more complex for the case of three distinguishable particles we are studying in our experiments, it is useful to discuss these analytic results as the qualitative behavior of the system remains similar. Last, we will discuss the effect of a finite momentum of the colliding particles on the recombination rate, which is a major limiting factor in current experiments.

3.4.1 Three-body recombination

Three-body recombination is the process of forming a two-body bound state in a three-body collision. As this process requires three particles to occupy a certain

region of space at the same time, the rate for these events scales with the third power of the density n . The loss is described by the differential equation

$$\frac{d}{dt}n = -K_3 n^3, \quad (3.35)$$

with the three-body rate coefficient K_3 .⁹

Let us first consider the case $a > 0$, where a universal dimer with binding energy $E_B = \hbar^2/ma^2$ exists. In this region the dominant three-body loss process is recombination into this shallow dimer state. The rate constant for this process was calculated to be [Nie99, Esr99]

$$K_{3,\text{shallow}} \approx 67.1 \sin^2 [s_0 \ln(a/a_0^+)] \frac{\hbar a^4}{m}, \quad (3.36)$$

which drops to zero at certain values of the scattering length given by

$$a_0^+ = 0.32 \kappa_*^{-1}. \quad (3.37)$$

With the inclusion of inelastic processes this equation changes to

$$K_{3,\text{shallow}} \approx 67.1 e^{-2\eta_*} \sin^2 [s_0 \ln(a/a_0^+) + \sinh^2 \eta_*] \frac{\hbar a^4}{m}. \quad (3.38)$$

When one examines Eq. 3.36, one finds that $K_{3,\text{shallow}}$ shows a general a^4 scaling, which is modulated by a \sin^2 term with a log-periodic dependence on a (see Fig. 3.6). These modulations of the recombination rate are called Stückelberg oscillations. To find out what causes this surprising effect let us recall Section 3.3 and especially Fig. 3.5. As $a > 0$, the three-atom state has to come in on a repulsive hyperspherical potential (see Fig. 3.3). As it enters the long-distance region, it can either be directly reflected as a three-atom state or couple to the lowest hyperspherical potential. The part of the incoming wavefunction that has coupled into the lowest hyperspherical potential can either leave as an asymptotic atom-dimer state, or enter the scale invariant region as a hyperradial wave. This hyperradial wave is reflected at the short-distance region and can then be transmitted through the long-distance region into the asymptotic atom-dimer state. This part of the outgoing atom-dimer state can now interfere with the part that was directly reflected

⁹In this definition, K_3 describes the number of lost particles. There is an alternative parameter L_3 which gives the number of loss events. For a three-component Fermi gas the two parameters are equivalent, but for a gas of identical bosons they differ by a factor of 3.

¹⁰This equation gives the three-body loss rate for a thermal gas of distinguishable particles. For a thermal gas of identical bosons this rate is a factor of three higher due to Bose statistics, while for a BEC the rate is reduced by a factor of two. (recheck this)

at the long-distance region. This interference effect causes the log-periodic suppression of three-body recombination in Eq. 3.37. It also explains why the depth of the minima is reduced for a finite η_* : Hyperradial waves that are lost into deep dimers in the short-distance region cannot be transmitted into asymptotic states to interfere with the directly reflected part of the atom-dimer wavefunction.

A similar process can also be observed in atom-dimer exchange reactions in a three-component Fermi gas (see Sect. 5.5.3).

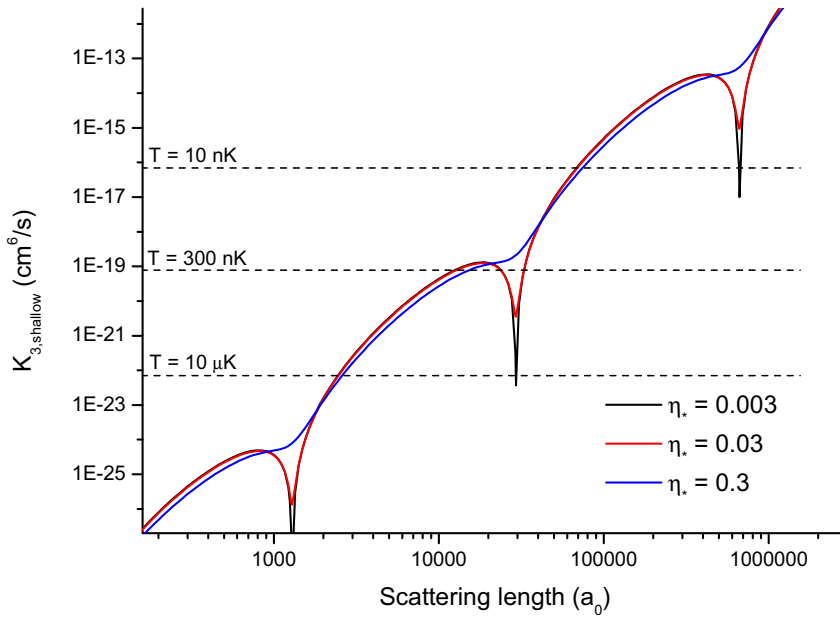


Figure 3.6: Recombination rate into the shallow dimer for a gas of (hypothetical) particles with identical scattering length $a > 0$ and the mass of ${}^6\text{Li}$ atoms as a function of a . Larger values of the inelasticity parameter η_* lead to a reduced contrast of the Stückelberg oscillations. For the calculation the three-body parameter a_*^+ was set to a value of $300 a_0$. The dashed lines show the temperature limit of the recombination rate according to Eq. 3.44 for different temperatures (see Sect. 3.4.3).

Now let us consider the case $a < 0$: As there is no universal dimer, the atoms have to recombine directly into the deep dimers. This is described by the formula

$$K_{3,\text{deep}} = \frac{4590 \sinh(2\eta_*)}{\sin^2(s_0 \ln(a/a_*^-)) + \sinh \eta_*} \frac{\hbar a^4}{m}, \quad (3.39)$$

which has maxima at $a = a_*^-$ where a trimer state crosses the three-atom continuum. Again, this can be understood from the considerations we made in Sect. 3.3: If there is a trimer state with zero energy, an incoming three-atom state with zero kinetic energy which is transmitted into the scale-invariant region is resonant with this trimer state. This leads to a three-body scattering resonance. The three-body recombination rate according to Eq. 3.39 is plotted in Fig. 3.7.

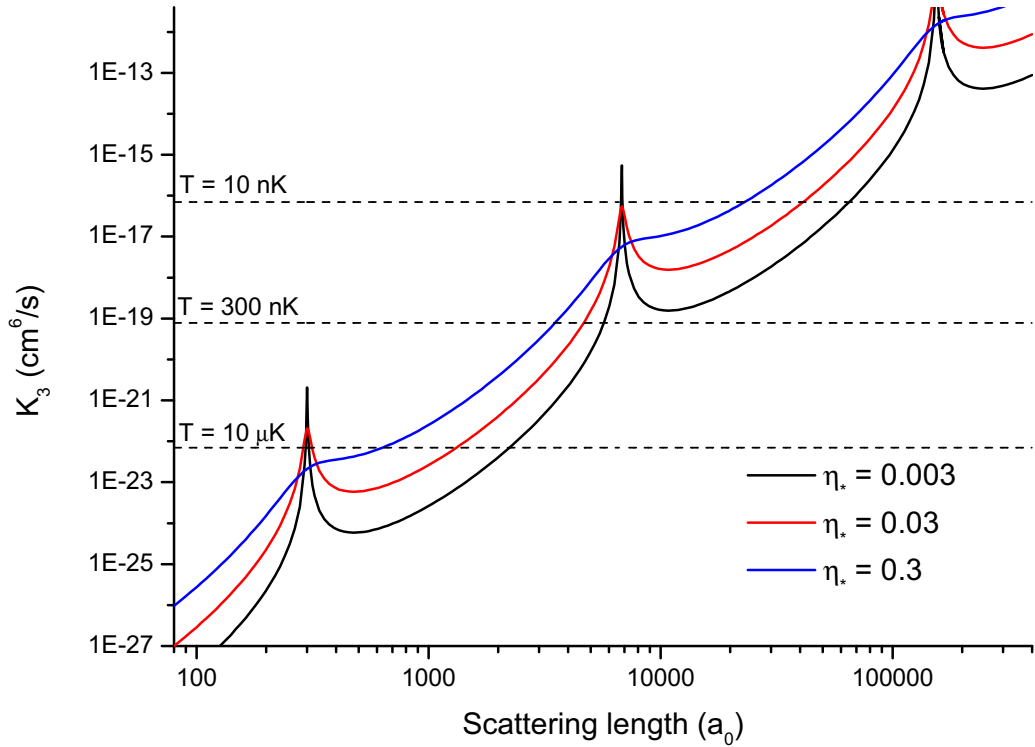


Figure 3.7: Three-body recombination rate for negative scattering length and a three-body parameter of $a_*^- = 300 a_0$. One can see that it is extremely difficult to observe more than two consecutive loss features at experimentally achievable collision energies.

3.4.2 Atom-dimer scattering

As mentioned in Sect. 3.1, atom-dimer scattering is resonantly enhanced by the crossing of a trimer state with the atom-dimer continuum. The atom-dimer scattering length is given by

$$a_{AD} = (1.46 + 2.15 \cot[s_0 \ln(a/a_*^+) + i\eta_*]) a; \quad (3.40)$$

it becomes resonant at scattering lengths a_*^+ where an Efimov trimer hits the atom-dimer threshold.

The imaginary part of a_{AD} describes inelastic atom-dimer collisions that lead to relaxation of the dimers into deeply bound states. The rate constant β for these processes is defined as

$$\frac{d}{dt}n_A = \frac{d}{dt}n_D = -\beta n_A n_D \quad (3.41)$$

with densities n_A and n_D for the atoms and dimers. This rate constant is given by

$$\beta = \frac{20.3 \sinh(2\eta_*)}{\sin^2(s_0 \ln(a/a_*^+)) + \sinh^2 \eta_*} \frac{\hbar a}{m}, \quad (3.42)$$

which is plotted in figure 3.8. Note that this relaxation rate scales linearly with a , in contrast to the a^4 scaling of the three-body loss.

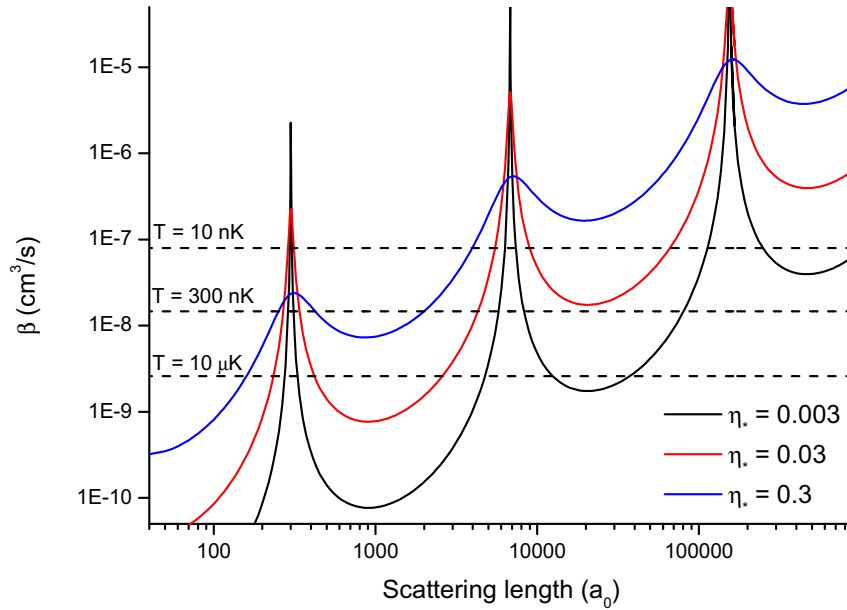


Figure 3.8: Rate constant for atom-dimer relaxation for a three-body parameter of $a_*^+ = 300 a_0$. The dashed lines give the unitary limit according to Eq. 3.45.

3.4.3 Effects of finite collision energy

The main (and until very recently the only) method to study Efimov states is the observation of structure (loss resonances and interference minima) superimposed on the general scaling of inelastic three-body and atom-dimer collisions with the scattering length. However, all of the results for collision rates given above were calculated for the limit of zero collision energy. This is a somewhat unrealistic assumption, as atoms with zero momentum cannot collide. Therefore all experiments have to be carried out with particles that have a finite momentum, which makes it essential to know up to which momenta the zero-energy theory gives a good description of the experiments.

The first condition is that the experiments have to stay inside the window of universality shown in Fig. 3.1. Otherwise critical approximations that could be made during the derivation of Efimov's radial law due to the low collision energy become invalid. However, as the momenta associated with the length scale of the van-der-Waals potential are much higher than the typical momentum of the particles in an ultracold gas this is usually not a problem.

Next let us examine the effect of a finite collision energy on a scattering resonance. For three atoms colliding with a finite collision energy, the resonance does not occur with a bound state at precisely zero energy, but with virtual state above the continuum.¹¹ For an atom-dimer resonance there is no virtual state as the trimer state does not cross the atom-dimer threshold, but merges into it (see [Kno09]). Therefore temperature shifts should be less pronounced for atom-dimer resonances. In addition to a shift of the resonance position, a thermal distribution of the colliding atoms also leads to a broadening of the resonance. However, these effects are only important if the kinetic energy of the particles is comparable to the width Γ_T of the trimer state that causes the resonance. In current experiments this is usually not the case, and one can neglect these effects.

The most important limitation caused by the finite collision energy is that the maximum cross section of the particles is limited by their momentum. This is called the unitary limit and was discussed in Section 2.3 in the context of two-body scattering. This limits the total number of collision events and therefore the maximum loss rate, which is reached when every collision leads to a loss event. Therefore the number of loss features that can be observed around a Feshbach resonance is limited by the particle momentum.

For a thermal gas the average momentum of the particles is given by the temperature. However, if the gas becomes quantum degenerate the temperature no longer sets the scale for the average kinetic energy of the particles. In a degenerate Fermi gas the momentum scale is set by the Fermi wave vector k_F , while in a BEC it

¹¹This is shown in Fig. 2.3, but note that this figure shows a Feshbach resonance, while Efimov states are detected by the observation of zero-energy scattering resonances.

is given by the inverse of the healing length $\xi = 1/\sqrt{8\pi an}$. The effect of this limit was studied in [D'I04]. For pure s-wave scattering they found that the three-body recombination rate for three distinguishable particles colliding with a fixed collision energy E is limited to

$$K_{3,max} = \frac{16\pi^2\hbar}{\mu k^4}, \quad (3.43)$$

where $\mu = m/\sqrt{3}$ is the three-particle reduced mass and $k = \sqrt{2\mu E/\hbar^2}$. For a thermal gas one has to average the collision energy over a Boltzmann distribution, which leads to a reduction of the maximum K_3 by a factor of two. This gives a maximum value of

$$K_{3,max} = \frac{2\pi^2\hbar^5}{\mu^3(k_B T^2)} \quad (3.44)$$

for a thermal gas in the unitary limit. The values of $K_{3,max}$ corresponding to different temperatures are plotted in Figures 3.6 and 3.7. Due to the overall a^4 scaling of the loss rate and the large scaling factor of 22.7 between the resonances it seems unlikely that it will ever be possible to observe more than three Efimov states of a single series in a system of identical bosons.¹²

The maximum loss rate for a collisions of atoms and dimers with a relative kinetic energy E can be derived from a formula given in [D'I08] to be

$$\beta_{max} = \frac{\pi}{\hbar^2 \mu_{AD} k_{AD}}, \quad (3.45)$$

with the atom-dimer reduced mass $\mu_{AD} = 2m/3$ and the momentum $k_{AD} = \sqrt{2\mu_{AD}E}$. The results of Eq. 3.45 for different temperatures are shown in Fig. 3.8.

3.5 The Efimov effect for distinguishable particles

Up to this point, we have restricted our discussion of the Efimov effect to the simple case of three identical bosons. Based on this example we have developed a formalism that allows us to describe the few-body physics of low-energy three-body systems. In the remainder of this thesis we will apply this formalism and especially the intuitive understanding we obtained by studying a simple system to the case of three distinguishable particles relevant for our experiments.

When one considers a three-body problem with distinguishable particles, there are two directions in which one can step away from the case of identical bosons: One is to consider particles with different masses, which among other things changes

¹²For particles with different masses, the scaling parameter can be much smaller, which should allow to observe longer series in such systems.

the value of the scaling parameter s_0 . Such a mass imbalance can have very interesting (and useful) effects [Mar08, Lev09, Bra06]. However, we will not discuss this case here as it is not relevant for our experiments, which use three different spin states of the same isotope.

The other knob one can tune with distinguishable particles is the relative size of the three different two-body scattering lengths. If only one scattering length is resonant, there is no Efimov effect. For particles with identical mass which have two resonant scattering lengths $a_{12} \approx a_{23} \gg r_0$ and one non-resonant scattering length $a \sim r_0$ there are Efimov states, but with a modified scaling factor of $e^{\pi/s_0} \approx 1985$. This makes it difficult to observe Efimov physics in such systems.

For three particles with identical masses and three different, but resonant scattering lengths $a_{12} \approx a_{23} \approx a_{13} \gg r_0$ the value of e^{π/s_0} is similar to the value of 22.7 for the case of identical particles. For the ${}^6\text{Li}$ system this condition is well fulfilled in a large magnetic field range. Therefore we will now examine this situation in more detail.

We start by examining how the considerations we made in Section 3.3 change for such a system. If the absolute values of the scattering lengths are of similar magnitude, the separation of the problem into four different regions we made in Section 3.3 is still valid. As there are three distinguishable particles there are now four asymptotic scattering states in the system: One three-atom state $|123\rangle$ and three atom-dimer states $|1, 23\rangle$, $|2, 13\rangle$ and $|3, 12\rangle$. Consequently the s-matrix S defined in Eq. 3.22 changes from a 2×2 matrix to a 4×4 matrix

$$S_3 = \begin{pmatrix} S_{|123\rangle,|123\rangle} & S_{|123\rangle,|1,23\rangle} & S_{|123\rangle,|2,13\rangle} & S_{|123\rangle,|3,12\rangle} \\ S_{|1,23\rangle,|123\rangle} & S_{|1,23\rangle,|1,23\rangle} & S_{|1,23\rangle,|2,13\rangle} & S_{|1,23\rangle,|3,12\rangle} \\ S_{|2,13\rangle,|123\rangle} & S_{|2,13\rangle,|1,23\rangle} & S_{|2,13\rangle,|2,13\rangle} & S_{|2,13\rangle,|3,12\rangle} \\ S_{|3,12\rangle,|123\rangle} & S_{|3,12\rangle,|1,23\rangle} & S_{|3,12\rangle,|2,13\rangle} & S_{|3,12\rangle,|3,12\rangle} \end{pmatrix} \quad (3.46)$$

whose off-diagonal elements describe the couplings between all these asymptotic states. These couplings still occur in the long-distance region and are described by an s-matrix defined analogous to Eq. 3.24. As this matrix also includes the couplings of the asymptotic states to hyperradial waves in the scale-invariant region it is a 5×5 matrix. One can now use the same method that was introduced in Sect. 3.3.1 to calculate the binding energies of the trimer states. However, the phase shift of the hyperradial waves - and therefore the binding energies of the trimer states - depends on all three scattering lengths.

If all scattering lengths are negative, no atom-dimer states are allowed and all elements of S_3 except for $S_{|123\rangle,|123\rangle}$ have to be zero, which greatly simplifies the theoretical treatment of the problem. For negative scattering lengths of similar magnitude the three-body loss rate can be described reasonably well by using an

effective scattering length

$$a_m = -\sqrt[4]{\frac{1}{3}(a_{12}^2 \cdot a_{23}^2 + a_{23}^2 \cdot a_{13}^2 + a_{13}^2 \cdot a_{12}^2)} \quad (3.47)$$

defined in [Wen09b] and the analytic formula Eq. 3.39 given in Sect. 3.4.1. This was done in [Wen09b, Wen09a, Ott10] and the results agree well with numerical calculations which explicitly consider three different scattering lengths [Bra09, Nai09, Flo09, Bra10].

For positive scattering lengths using an effective scattering length is not a viable choice, as the physics critically depend on the binding energies of the different dimer states, which are determined by the respective scattering lengths. If one scattering length a_{ij} is positive there is one dimer state in the system and the corresponding matrix element $S_{|i,jk\rangle,|ijk\rangle}$ becomes non-zero. This means that three-body recombination into this dimer is allowed.

If there are two positive scattering lengths a_{ij} and a_{jk} there are two dimer states available for three-body recombination. If we assume $a_{ij} < a_{jk}$, the matrix element $S_{|k,ij\rangle,|i,jk\rangle}$ is generally non-zero as well. This matrix element corresponds to an exchange reaction of the type $|i\rangle + |jk\rangle \rightarrow |k\rangle + |ij\rangle + E_{kin}$. Whether the inverse process $S_{|i,jk\rangle,|k,ij\rangle}$ is possible depends on the kinetic energy of the particles involved in the collision. For three positive scattering lengths there are three dimer states in the system, and the number of non-zero matrix elements increases further.

In a three-component gas of ${}^6\text{Li}$ all these cases can be realized, which makes it possible to study all the effects described above.

Actually calculating the rate coefficients for the different processes goes beyond our abilities, but this has been done by several theory groups [Ham10, Nak10b, Nai10]. We will discuss these results together with our measurements in chapter 5.

In this discussion we have neglected three-body recombination processes which include two identical fermions. However, as we have mentioned in Sect. 2.7 these processes are possible for large scattering lengths. We will briefly discuss this in Sect. 5.4.

3.6 Experimental observations of the Efimov effect

After V. Efimov had developed his scenario in the 1970s [Ef71, Ef70, Ef79], experimentalists began to look for physical systems which would allow to study this intriguing effect. For a long time, the most promising candidates were cold ${}^4\text{He}$ atoms, which have a large and positive scattering length. For this system, two trimer states with binding energies of $E_0 = k_B \times 125 \text{ mK}$ and $E_1 = k_B \times 2.3 \text{ mK}$

were predicted by theory. Measurements of the binding energy of the ground state trimer were consistent with the universal prediction, but this trimer is on the edge of the window of universality. Therefore it was questionable whether this trimer could be considered to be an Efimov state. The excited trimer state would definitely be universal, but unfortunately it was never observed and the Efimov effect remained unconfirmed for more than thirty years.

This changed when researchers began to create dilute gases of ultracold atoms [And95, Dav95]. These systems are in a regime where the low-energy assumption made in Efimov's scenario is fulfilled better than in any other system. Combined with the ability to control the interactions in these gases using Feshbach resonances [Ino98, Chi10] this gave researchers the possibility to create low-energy systems with tunable interactions. These systems were perfectly suited for studying Efimov physics.

In 2006 the group of R. Grimm observed resonances and interference minima in the three-body-recombination rate of a gas of ultracold Cesium atoms [Kra06]. These results provided the first convincing evidence for the existence of universal trimer states.

In 2008 researchers at LENS observed loss features in a mixture of ^{87}Rb and ^{41}K and in a different experiment also in a gas of ^{39}K [Bar09, Zac09]. In the latter experiment they observed multiple features around a Feshbach resonance, which provided evidence for the existence of a series of trimer states in the system. Additionally, the Innsbruck group observed a resonant enhancement of the atom-dimer relaxation rate in an atom-dimer mixture of ^{133}Cs [Kno09], which they interpreted as a signature of an Efimov trimer hitting the atom-dimer threshold. However, none of these experiments could verify the predicted scaling factors between the positions of these resonances (see eqs. 3.31, 3.32 and 3.37). It was – and to some extent still is – unclear what causes these discrepancies. One candidate are corrections caused by the finite range r_{vdW} of the interaction potential. Another possible explanation is a dependence of the short-range three-body physics on the magnetic field, which was varied in these experiments to tune the scattering length with Feshbach resonances. However, there could also be other currently unknown systematic effects.

Since then, loss features have been observed in a gas of bosonic ^7Li atoms which exhibit the expected scaling across the Feshbach resonance [Gro09, Gro10], although there are contradictory results by another group using the same system [Pol09]. However, there seem to be some problems with the calibration of the magnetic field dependence of the scattering length in [Pol09] which can probably explain this discrepancy.

In the spring of 2008 we managed to create our first three-component degenerate Fermi gas of ^6Li and observed two three-body loss resonances in the magnetic field region below 600 G [Ott08, Wen09a, Ott10]. These were subsequently in-

terpreted as signatures of an Efimov state [Wen09b, Bra09, Nai09, Flo09]. This observation was quickly confirmed by the group of K. O'Hara [Huc09], followed by their observation of another loss resonance above the Feshbach resonances at ~ 900 G [Wil09]. After this we studied the collisional behavior of different atom-dimer mixtures of ${}^6\text{Li}$ [Lom10a] (see also [Nak10b]) and developed a technique to directly probe Efimov states with RF-association [Lom10b], which was quickly adopted by the group of M. Ueda to verify our results [Nak10a]. Chapter 5 will describe our experiments on three-body recombination and atom-dimer scattering, while chapter 6 will describe the RF association experiments.

Chapter 4

Experimental Setup

When we began setting up our experimental apparatus four years ago, the goal was to create a machine which was robust, reliable and could produce molecular BECs or degenerate Fermi gases with high repetition rate and reproducibility. Our strategy for achieving these goals was to keep the machine as simple as possible. The reasoning behind this was that a more complicated setup contains more lasers, electronics and optics that can potentially break or become misaligned and is therefore less reliable. Additionally, more complex setups which contain e.g. multiple stages connected by optical or magnetic transport of atoms usually have longer cycle times. Last but not least, a simple machine can be set up faster, which allowed us to perform first experiments only a year after we began to build our machine. But this simplicity does not come for free: It is paid for by making sacrifices on other important aspects, such as the optical access to the atoms and the maximum particle number that can be achieved in the BEC or degenerate Fermi gas.

One of the first decisions one has to make when planning a new experiment with ultracold atoms is the choice of the atomic species. For fermions the selection of atoms that can easily be laser cooled is actually pretty limited: The only usable fermionic alkali atoms are ${}^6\text{Li}$ and ${}^{40}\text{K}$.¹ The main reasons ${}^6\text{Li}$ was chosen for our experiment were its broad Feshbach resonances, the exceptional stability of its Feshbach molecules and the fact that our principal investigator had already successfully worked with this species before.

In the past there have been two different approaches to creating degenerate Fermi gases of ${}^6\text{Li}$. One is to use a two species mixture consisting of ${}^6\text{Li}$ and a bosonic atom which serves as a coolant.² Examples for this approach are the experiments

¹While there are other non-alkali fermions that can be laser cooled, they either have no magnetic Feshbach resonances (e.g. ${}^{87}\text{Sr}$ or ${}^{171}\text{Yb}$) or are technically more challenging and much less well-understood (e.g. ${}^{53}\text{Cr}$).

²Remember that identical fermions do not interact at ultracold temperatures (see Sect. 2.3).

at Rice University (R. Hulet) and ENS (C. Salomon) [Tru01, Sch01], that use ^7Li as a coolant and the experiments at MIT (W. Ketterle, M. Zwierlein), which use a ^6Li - ^{23}Na mixture [Had03]. This strategy can lead to very large samples – degenerate Fermi gases with up to 10^7 atoms have been prepared in M. Zwierlein’s experiment in this way – but the second species certainly adds a lot of complexity to these experiments.

An alternative approach that was pioneered at Duke University (J. Thomas) [Gra02] and in Innsbruck (R. Grimm) [Mos01] is to use a spin mixture of the two lowest-energy Zeemann substates of ^6Li ($|1\rangle$ and $|2\rangle$) for evaporative cooling. As this spin mixture is stable for resonant interactions (see Sect. 2.7), evaporative cooling can be performed in a regime where the interparticle scattering length is large. This leads to a very fast and robust evaporation (see Sect. 4.6). For these reasons this approach was chosen for our experiment.

The setup of our apparatus has been described in detail in one PhD and several Diploma theses over the last years [Ser07, Lom08, Koh08, Wen09a, Zür09, Ott10]. Therefore this thesis gives only a rather broad overview over the experimental setup and refers to the above mentioned theses for details. The exception are aspects of the setup that have direct relevance to the experiments described in this thesis, which are discussed more exhaustively.

This chapter begins with a description of the vacuum chamber in which the experiments are performed. The next sections deal with the setup of the magneto-optical trap (MOT) and discuss the technique of resonant absorption imaging before describing the imaging setup. Afterward, we discuss the coils which generate the magnetic fields necessary for tuning the interparticle interactions and the optical dipole trap we use to trap our atoms. The chapter closes by introducing two "standard" experimental sequences that are the starting point for almost all of our experiments.

4.1 The vacuum chamber

Ultracold gases usually have temperatures which range from a few nK to a few hundred μK , yet these gases can be prepared in an experimental setup which is at room temperature. This is only possible if the ultracold gas has only negligible coupling to the environment. Therefore the gases are trapped in an ultra-high vacuum (UHV) environment using optical or magnetic traps. In this section we will describe our vacuum setup, the trapping of the atoms will be discussed in Section 4.3.

As the magnetic and optical traps used to hold ultracold gases usually have a depth of at most a few mK, collisions of a trapped atom with a particle from the rest gas in the vacuum chamber – which has a temperature of about 300 K –

invariably lead to the loss of this atom from the trap. Therefore the timescale at which such collisions depopulate the trap must be much longer than the duration of the experiments, which in our case is typically between five and fifteen seconds. Achieving such a low collision rate requires a background pressure on the order of 1×10^{-11} mbar or below, which is challenging to reach in a non-cryogenic system. Our vacuum chamber consists of two main sections. The first is the oven section, where Lithium is evaporated in a small oven at temperatures between 350°C and 400°C to create an atomic beam for the Zeeman slower (see Sect. 4.2). The outgassing of the hot oven limits the achievable pressure in this section to 1×10^{-10} mbar. The oven section is connected to the experiment chamber by the drift tube of the Zeeman slower, which also serves as a differential pumping stage.

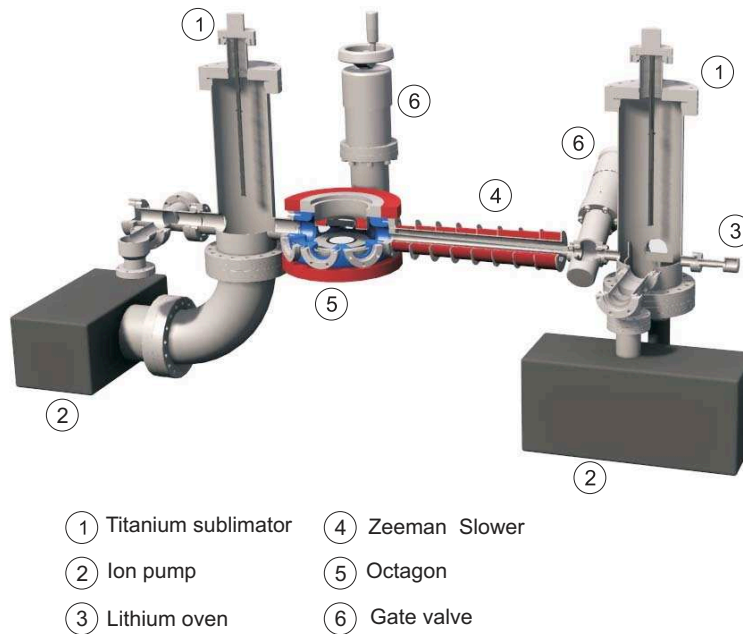


Figure 4.1: Cut through the vacuum chamber, the magnetic field coils for the MOT and Zeeman slower as well as the Feshbach coils are shown in red. The oven chamber on the right can be separated from the main chamber (left) by closing a gate valve, this allows to refill the Lithium oven without breaking the vacuum in the main chamber. The ion-getter pump in the experiment section is placed at some distance from the octagon to prevent stray magnetic fields from the pump's magnets from affecting the experiments.

The experiment chamber consists of a spherical octagon (MCF600-SO200800-A, Kimball Physics) with six CF40 viewports and two reentrant CF150 viewports. The numerical aperture (NA) achievable through the side viewports is about 0.15, while for the reentrant viewports $\text{NA} > 0.6$, which provides adequate optical ac-

cess . While a glass cell can in principle provide greater optical access, its inner surfaces cannot be anti-reflection coated. With a glass cell one is therefore more likely to run into problems with unwanted reflections or stray light, especially when trying to count individual atoms [Ser11]. Additionally, a steel octagon is much more robust than a glass cell. On the other hand, eddy currents in the steel chamber can limit the switching speed of magnetic fields applied to the atoms (see Sect. 4.4). So while both a glass cell and a steel chamber have their advantages, considering our experiences of the past four years we believe that using an octagon was a good choice.

Both the oven section and the experimental chamber are pumped by a combination of ion-getter and Titanium-sublimation pumps (see [Ser07, Ott10] for details). These have the great advantage that they work in a closed system and do not produce any noise or vibrations. Additionally we were able to obtain a non-evaporable getter (NEG) coating for our octagon, which pumps reactive gases right in the region where the experiments take place. The pressure in the experimental chamber is of order 1×10^{-11} mbar or below. We have measured the vacuum limited lifetime to be greater than five minutes [Ser07], which is more than enough for our experiments.

On one of the side flanges of the octagon there is a CF40 gate valve, which allows to add an additional section to the system without breaking the vacuum in the main chamber. This could be used to insert additional components such as for example an atom chip into the main chamber. However, so far no concrete plans have been made to add anything to the experiment through this valve.

4.2 Magneto-optical trap and Zeeman slower

To create an ultracold gas of ${}^6\text{Li}$ one first has to get the Lithium atoms - which form a solid at room temperature - into the gas phase. This is done by evaporating Lithium in an oven at a temperature between 350°C and 400°C . The Lithium atoms leaving the oven are then collimated into an atomic beam which passes through the experimental chamber. The first step to creating an ultracold gas is to slow a significant fraction of the beam ($\sim 1\%$), which has a mean velocity of ~ 1000 m/s down to a velocity smaller than about 50 m/s at which the atoms can be captured in a MOT.

4.2.1 The Zeeman slower

To slow down the hot atoms coming out of the oven we use the powerful technique of laser cooling, which was developed by S. Chu, C. Cohen-Tannoudji and W. Phillips in the 1980s [Met99]. The basic idea is to use a near-resonant laser

beam which is counterpropagating to the atomic beam. If an atom is excited by the laser beam, it absorbs a photon and its momentum is reduced by the momentum of this photon. When the excitation decays the atom spontaneously emits a photon into a random direction. If the atom primarily decays back to the initial state, this transition is called a closed (or "cycling") transition and the process can be repeated many times. As the total momentum transfer from the spontaneous emissions is zero in the limit of many cycles, this leads to a net force which slows down the atoms. While the momentum of a single photon is tiny compared to the initial momentum of the atoms, the scattering rate for a saturated D2 transition of a typical alkali atom is ~ 15 MHz. Therefore it is possible to reach decelerations of up to $10^5 g$ with this method, which allows to slow a ${}^6\text{Li}$ atom from a velocity of ~ 1000 m/s to almost a standstill over a distance of less than half a meter.

For atoms that are moving towards the slowing light the transition is blue-shifted by the Doppler effect, which has to be compensated by detuning the laser beam to the red of the cooling transition. However, as the atoms are slowed down their Doppler shift changes and they fall out of resonance with the slowing light. To prevent this, we apply a spatially varying magnetic field which creates a Zeeman shift of the cooling transition. With the right field geometry this compensates the changing Doppler shift of the slowed atoms. This device is called a Zeeman slower.

Our Zeeman slower is described in detail in [Ser07]. It has a decreasing field configuration, which allows to use the radial component of the MOT field as the last part of the Zeeman slower. Therefore the atoms reach their final velocity just as they enter the MOT. This alleviates the problem that the atoms tend to spread out and largely miss the capture radius of the MOT at the end of the Zeeman slower, as they are not cooled in the transversal direction during the slowing process.

4.2.2 The magneto-optical trap

By overlapping six red-detuned laser beams coming from all spatial directions it is possible to create a strong damping (or cooling) effect on the motion of the atoms. Therefore this setup is called an optical molasses. The temperature in this molasses is given by an equilibrium between the cooling force generated by the absorption of photons from the laser beams and the heating of the atoms by spontaneous emission. In the limit of low saturation the temperature

$$T_{molasses} = \frac{\hbar\Gamma}{4k_B} \frac{1 + (2\delta/\Gamma)^2}{|\delta|/\Gamma} \quad (4.1)$$

depends on the detuning δ from the resonance and the linewidth Γ of the cooling transition. The minimum temperature that can be achieved with this type of

cooling is given by the natural linewidth of the cooling transition: If the momentum of the particles becomes so low that their Doppler shift becomes smaller than the linewidth of the transition, the absorption of light from the counter- and co-propagating light beams becomes equally likely and this cooling mechanism breaks down. This is called the Doppler limit, the minimum achievable temperature is given by

$$T_D = \frac{\hbar\Gamma}{2k_B} \quad (4.2)$$

which is reached for $\delta = -\Gamma/2$ [Met99]. For some species this limit can be overcome by sub-Doppler cooling techniques such as polarization gradient cooling, which allow cooling down to the temperature

$$T_r = \frac{\hbar^2 k^2}{2k_B m}, \quad (4.3)$$

which corresponds to the recoil of a single photon with momentum $\hbar k$. Unfortunately the low mass and consequently high Doppler temperature of Lithium has – at least to our knowledge – prevented achieving sub-Doppler cooling in this system so far.

By adding magnetic field gradients in all spatial directions (i.e. a quadrupole field) and choosing the right polarizations for the light beams one can use the Zeeman effect to also create a spatial confinement for the atoms. This is called a magneto-optical trap (MOT) (see Fig. 4.2).

Our MOT consists of three retroreflected laser beams with a diameter of ~ 20 mm and a set of anti-Helmholtz coils placed around the flanges of the reentrant viewports to create a quadrupole field. The MOT coils generate a magnetic field gradient of ~ 40 G/cm in the strong axis. The laser light for the MOT and slowing beams is created on a separate table and brought to the experiment by optical fibers. As described above, the detuning of the lasers with respect to the atomic transition is critical for the success of laser cooling. Therefore the frequency of our lasers has to be controlled with a precision much higher than the linewidth of ~ 6 MHz of the ${}^6\text{Li}$ D2 transition we use for cooling the atoms.

Therefore we use narrowband light sources which consist of extended-cavity diode lasers (DL100, Toptica photonics) whose frequency can be stabilized by modulating the length of the laser cavity with a piezoelectric actuator. To create a frequency reference to which we can stabilize these lasers we lock one diode laser to the $F = 3/2 \rightarrow F = 5/2$ transition by Doppler-free spectroscopy of ${}^6\text{Li}$ in a vapor cell. All other 670 nm lasers in our lab are stabilized relative to this laser using beat offset locks (see [Sch99, Ser07, Lom08]).

To create sufficient laser power for our MOT we use a diode laser which is amplified by a tapered amplifier chip to an output power of ~ 400 mW (TA100, Toptica

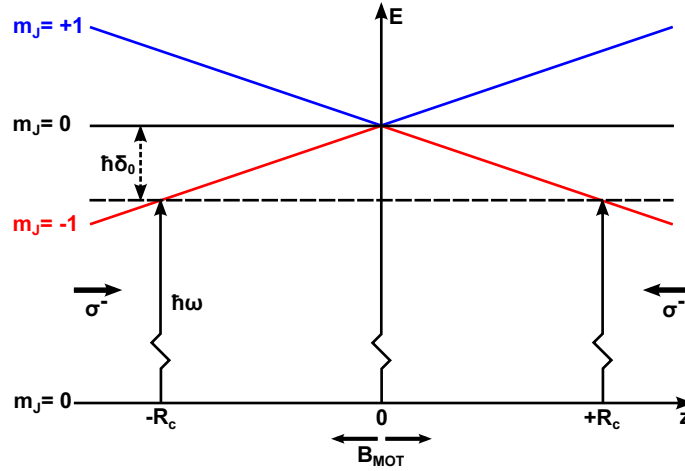


Figure 4.2: 1D-sketch of the spatial dependence of the transition frequency for a zero-velocity atom in a MOT. A magnetic field pointing outwards from the center creates a Zeeman splitting of the excited state. By shining in σ -polarized light one can selectively address the magnetic sublevels, in this case the $m_J = -1$ state. At a distance R_c from the center, which depends on the detuning δ and the strength of the magnetic field gradient, the transition becomes resonant and the atom is pushed back into the center. For a more detailed discussion see [Met99]

photonics). As the hyperfine splitting of the excited state is smaller than the natural linewidth of the transition, the cooling transition $F = 3/2 \rightarrow F = 5/2$ is actually not a cycling transition. Consequently a Lithium MOT requires an unusually large amount of repumping light. Therefore the TA is locked to the crossover between $F = 3/2 \rightarrow F = 5/2$ (cooler) and $F = 1/2 \rightarrow F = 3/2$ (repumper) transitions of the ${}^6\text{Li}$ D2 line (see Fig. 4.4) and the light is split up with a ratio of three to one between cooler and repumper. The two beams are then red (blue) shifted by 114 MHz with acousto-optic modulators (AOMs) to create the cooling (repumping) light. These AOMs are also used to control the intensity of the cooling and repumping light during the loading of the optical dipole trap (see Sect. 4.6). Then cooler and repumper are recombined and part of the light is coupled into three optical fibers for the MOT beams, while the rest is red-shifted by 70 MHz with another AOM to provide the light for the Zeeman slower (see Fig. 4.3). The total power that arrives on the experiment table is ~ 40 mW per MOT beam and ~ 70 mW for the slowing beam. In our experience this amount of power is completely sufficient to run a ${}^6\text{Li}$ MOT. We achieve loading rates of about 10^8 atoms/s at an oven temperature of 350°C , which is completely sufficient for our purposes. For a detailed analysis of the performance of our MOT see [Ser07].

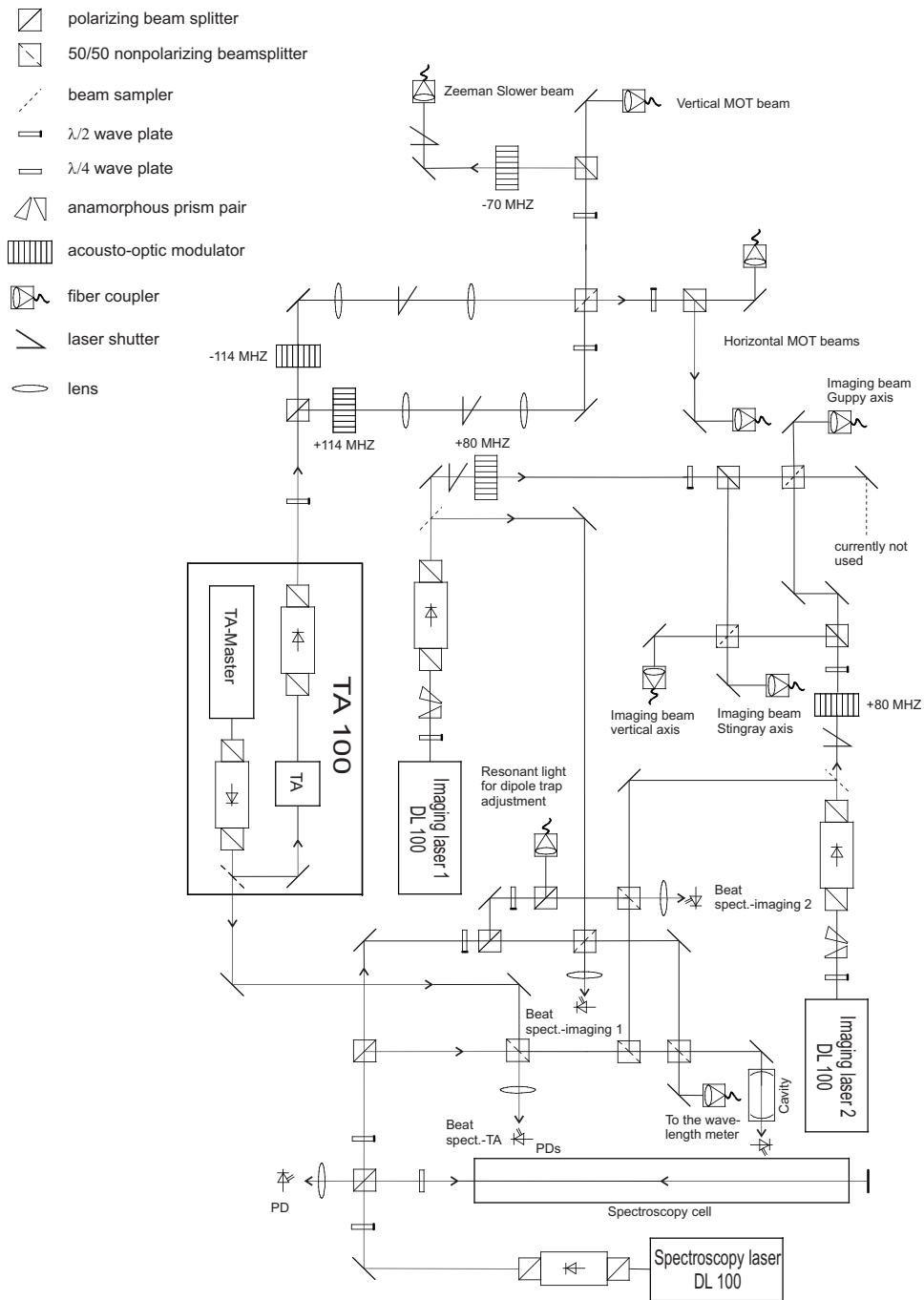


Figure 4.3: Drawing of the laser setup which creates the 670nm light for MOT and imaging systems.

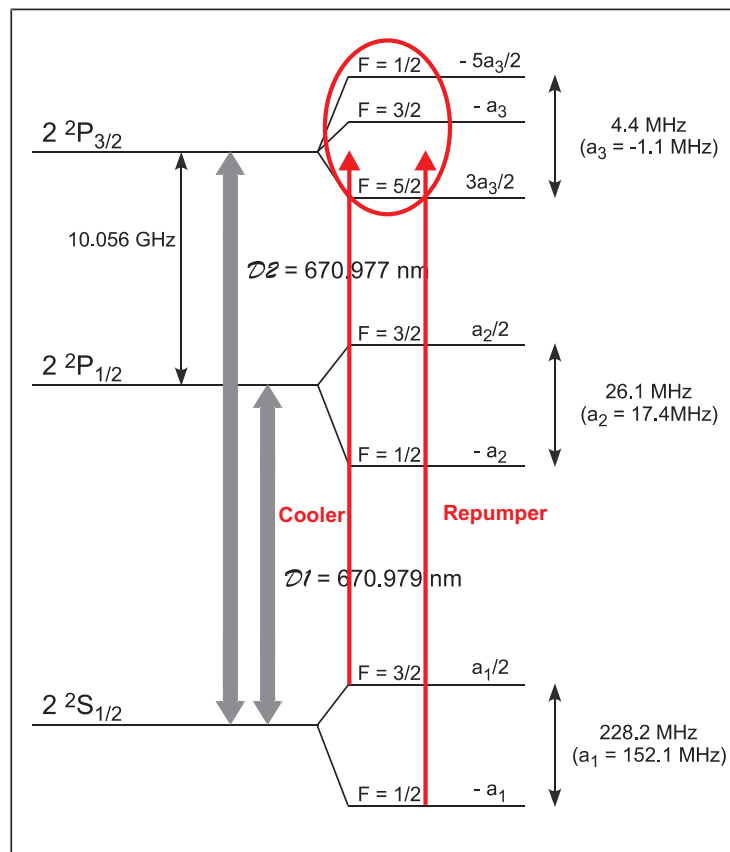


Figure 4.4: Level scheme of ${}^6\text{Li}$. Note that the excited state hyperfine splitting is not resolved, as it is smaller than the natural linewidth of 6 MHz of the transition.

4.3 Optical dipole trap

While laser cooling is an indispensable tool for creating ultracold gases, it is currently not possible to directly create quantum degenerate gases with this technique. The reason for this is that the maximum phase-space density in a MOT is usually limited to values of $10^{-5} - 10^{-3}$ by light-assisted collisions, in which two atoms form a molecule with the aid of a photon.

The solution to this problem is to transfer the atoms from the MOT into a conservative potential and perform evaporative cooling. This is the standard method for creating ultracold quantum gases and is used in almost all experiments. The technique is based on the fact that the trapping potential has a finite depth U . For a thermal gas in the trap this corresponds to a cut-off of the high-energy tail of the Boltzmann distribution as all atoms with a kinetic energy $E > U$ escape from the trap. Through this loss of high-energy particles and subsequent rethermalization of the sample via elastic collisions the temperature of the sample is reduced; this process is called plain evaporation. In principle this process can cool the sample down to zero temperature, but the fraction of escaping particles

$$\frac{N_{free}}{N_{trapped}} \propto e^{-\frac{U}{k_B T}} = e^{-\eta} \quad (4.4)$$

and therefore the cooling rate decreases exponentially with the ratio $\eta = U/k_B T$ between trap depth and temperature of the gas, which is called the truncation parameter. In experiments plain evaporation usually stagnates for values of η between five and ten, as the temperature of the sample reaches an equilibrium between evaporative cooling and residual heating caused e.g. by noise on the trapping potential. To bring a system to lower temperature one therefore performs forced evaporation by lowering the trap depth U as a function of time. The optimum evaporation trajectory $U(t)$ as well as the maximum efficiency of the process depend on the rate of elastic collisions, the heating rate and the vacuum limited lifetime of the atoms in a non-trivial fashion. However, the rule of thumb is that a reduction of the particle number by a factor of ten leads to an increase in phase space density by about three orders of magnitude. For a detailed discussion of the optimum evaporation scheme in optical traps see [O'H01, Luo06].

Creating the conservative potential is usually done in one of two ways. The first is to use traps which act on the magnetic moment of the atoms. These have the distinct advantage that they are relatively easy to realize - the simplest magnetic trap requires only a magnetic quadrupole field. However, using a magnetic trap severely limits the ability to tune the interparticle interactions with Feshbach resonances. Additionally, these traps can only be used for atoms in low-field seeking states, as Maxwell's equations forbid creating a maximum of the magnetic field in free space.

The other way to hold ultracold atoms in place is to use optical traps. For a laser which is far detuned from the atomic resonance the light can be viewed as an oscillating electric field $\mathbf{E}(\mathbf{r}, t)$ which induces a dipole moment $\mathbf{p}(\mathbf{r}, t)$ in the atoms. In the electric field of the laser this dipole has a potential energy

$$U_{dip} = -\frac{1}{2} \langle \mathbf{E}\mathbf{p} \rangle, \quad (4.5)$$

where the brackets denote a time average. The relative sign of the dipole moment and the electric field depend on the detuning of the electric field from the resonance frequency of the atom: If the driving frequency is below resonance (i.e. the laser is red-detuned from the atomic transition) the dipole oscillates in phase with the electric field and the potential is attractive. For blue-detuned light the dipole is out of phase with the driving field and the potential is repulsive. A trap can therefore either be created by a (local) intensity minimum of a blue-detuned or by a local maximum of a red-detuned light field. As an intensity maximum can be created by simply focussing a laser beam, red detuned traps are much easier to realize and therefore much more common.

The depth of the trapping potential

$$U_{dip}(\mathbf{r}) = -\frac{3\pi c^2}{2\omega_0^3} \left(\frac{\Gamma}{\omega_0 - \omega} + \frac{\Gamma}{\omega_0 + \omega} \right) I(\mathbf{r}) \quad (4.6)$$

is given by the natural linewidth Γ of the transition, the laser intensity I and the detuning $(\omega_0 - \omega)$ of the light from the resonance frequency ω_0 . An inherent disadvantage of optical traps is that the atoms can scatter the trapping light, which leads to heating or loss of atoms from the trap. However, while the trap depth scales linearly with the detuning of the light, the scattering rate

$$\Gamma_{sc}(\mathbf{r}) = -\frac{3\pi c^2}{2\omega_0^3} \left(\frac{\omega}{\omega_0} \right)^3 \left(\frac{\Gamma}{\omega_0 - \omega} + \frac{\Gamma}{\omega_0 + \omega} \right)^2 I(\mathbf{r}) \quad (4.7)$$

drops off quadratically with growing detuning. Therefore this problem can be reduced by using very far-detuned light. Of course, creating deep traps then requires very high laser intensity. For a detailed review of optical dipole traps see [RG00]. Let us now take a look at the situation for a gas ${}^6\text{Li}$ atoms: All spin mixtures of low-field seeking states ($|4\rangle$, $|5\rangle$ and $|6\rangle$) are unstable against dipolar relaxation and therefore unusable. Consequently evaporative cooling of ${}^6\text{Li}$ in a magnetic trap cannot be done without using atoms of another species as a coolant. Therefore using a magnetic trap was incompatible with our goal of building a simple apparatus.

The alternative to using a magnetic trap is to load an optical dipole trap directly from the MOT. Loading a sufficient number of atoms into the dipole trap requires a large-volume trap which is significantly deeper than the temperature of

the atoms in the MOT. As the minimum temperature of a ${}^6\text{Li}$ MOT is $\sim 200 \mu\text{K}$ (see Sect. 4.2) one needs a trap with a depth of at least 1 mK. While this requires a huge amount of laser power, this is a problem for which a relatively simple solution exists in the form of high-power fiber lasers. Therefore this approach was chosen for our experiment.

For our dipole trap we use a 200 W fiber laser (YLR-200-LP, IPG Photonics) at a wavelength of 1070 nm, which is far red-detuned from the Lithium D line at 670 nm. Longitudinally the laser is multi-mode, with a spectral width of several nm, but transversally the beam is in an almost perfect TEM00 mode as it comes out of a single mode fiber. To create the optical dipole trap we use a configuration where we cross two beams with a waist of $\omega_0 \approx 40 \mu\text{m}$ under an angle of $\sim 7^\circ$. This creates a cigar-shaped trap with an aspect ratio of about 10 : 1 (see Fig. 4.6).

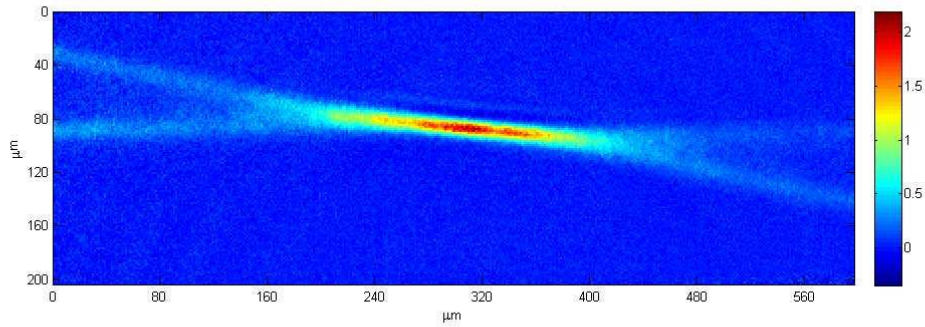


Figure 4.5: In-situ absorption image of atoms in the optical dipole trap taken from the vertical direction. To better visualize the shape of the trapping potential the image was taken with a cloud of "hot" atoms which also populated the outer regions of the trap.

We found that it is essential to precisely cross the polarizations of the counterpropagating beams when using a multi-mode laser in such a crossed configuration; if we did not do this we observed strong one-body losses which rapidly depopulated the trap (see [Lom08, Koh08]). Therefore we clean the polarization of the incoming beam with a brewster polarizer and rotate the polarization of the returning beam by 90° with a half-wave plate.

To control the laser power in the dipole trap we use two acousto-optical modulators (AOMs) (3110-197, Crystal Technology). We employ a digital feedback loop running on our experiment control system (Adwin Pro II, Jäger Messtechnik, see [Lom08, Ott10]) to stabilize the laser power by varying the RF-power in the AOMs. As we have to control the laser power over four orders of magnitude during the evaporation (from 40 W down to a few mW) we switch the input of the

servo loop between two photodiodes with different gain for operation at high and low laser power.

The major challenge in setting up and running the dipole trap turned out to be thermal effects in the optics, which create focus shifts and beam deformations at high laser power. However, we can circumvent this problem by using the full laser power only for short times (see [Lom08, Koh08]). For details on the setup of the optical dipole trap see [Lom08, Koh08, Ott10].

4.4 Feshbach coils

Control over the interparticle interactions is one of the key requirements for all of our experiments. As we have seen in Section 2.6 we can achieve this by applying magnetic offset fields between 0 G and 1500 G, which we create with a pair of magnetic field coils in an (almost) Helmholtz configuration. To obtain precise control over the interaction strength the current in these coils has to be stabilized to an accuracy better than 10^{-4} . This is achieved with a digital feedback loop running on our experiment control system, which acts on the voltage of the power supply of the coils (SM15-400, Delta Elektronika). The input for this servo loop is provided by measuring the current in the coils with a current transducer (Ultrastab866-600, Danfysik) and precision resistor (see [Koh08]). The Feshbach coils were designed to fit around the high-NA windows inside the reentrant viewports. This allows us to place the coils close to the atoms, resulting in small coils whose magnetic field fills only a small volume. This leads to a low inductance of the coils of only ~ 13 mH as well as minimizing the effects of eddy currents in the octagon. However, the limited space available in the reentrant viewports made the design and manufacture of the coils quite challenging; it took two years and three generations of Feshbach coils until we had achieved a fully satisfactory result (see [Ser07, Lom08, Zür09]). Our current coils consist of fifteen windings of 5×1 mm copper wire glued to a water-cooled heatsink with a diamond-filled epoxy. The maximum field is about 1450 G at a power dissipation of about 2.5 kW per coil.

The coils are placed slightly closer to each other than in a Helmholtz configuration. This leads to a magnetic field saddle which has a field maximum in the radial direction, while in the axial direction there is a field minimum at the center. As the atoms used in our experiments are high-field seekers, this creates a confining potential in the radial direction, while the atoms are anticonfined in the axial direction. This has the advantage that the magnetic confinement is aligned with the weak axis of the optical trap, which greatly simplifies the creation of very shallow optical potentials. Due to the small displacement of the coils from the Helmholtz configuration the saddle is very weak, for a magnetic field of 800 G the confinement is only about 15 Hz. This corresponds to a change in magnetic field of only

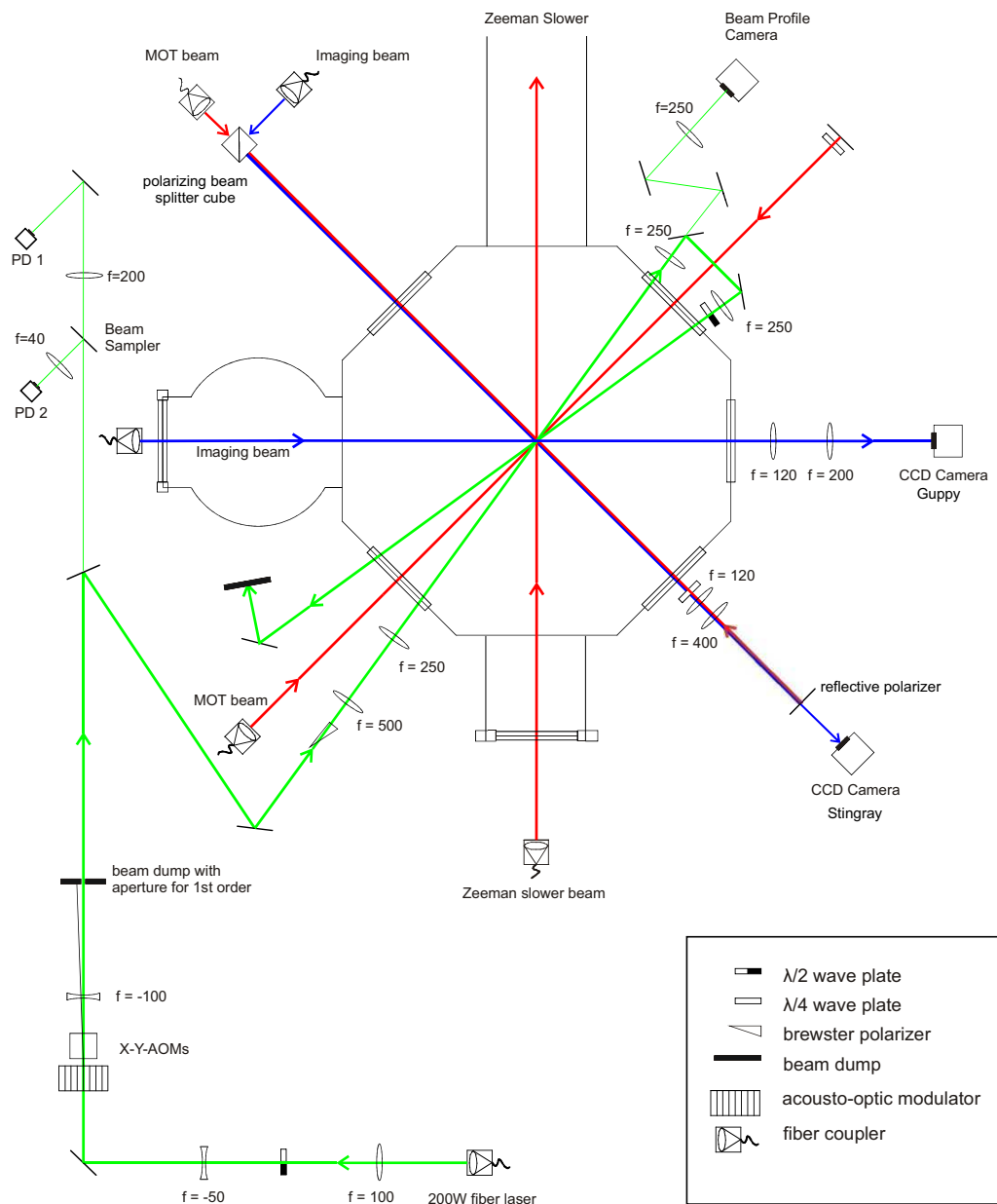


Figure 4.6: Sketch of the optics around the octagon. The beam path of the laser creating the optical dipole trap is shown by the green line, the MOT and Zeeman slowing beams are red and the imaging beams are drawn in blue.

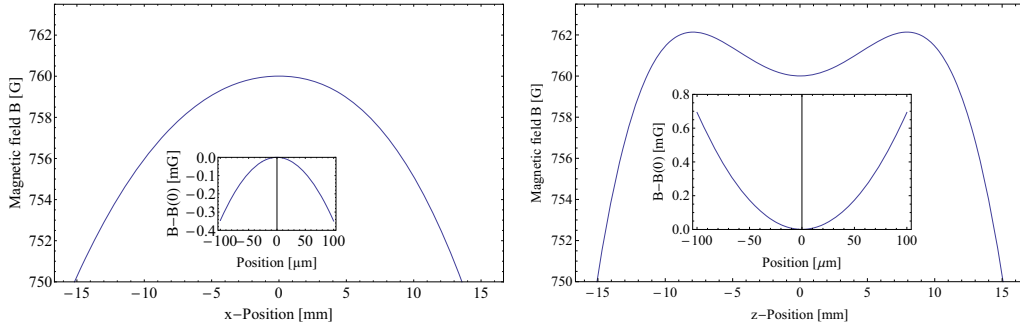


Figure 4.7: Simulation of the magnetic field created by the Feshbach coils. The left panel shows a radial cut through the center of the coil assembly. As ${}^6\text{Li}$ atoms in states $|1\rangle$, $|2\rangle$ and $|3\rangle$ are high-field seekers, the atoms feel a confining potential in the radial direction. In the axial direction (right panel) the magnetic field has a minimum in the center, which leads to an anti-confinement in this direction.

~ 35 mG over a distance of 1 mm, which makes this saddle very sensitive to any disruption of the rotational symmetry of the coils. Such distortions can for example be caused by a number of turns on the coil which is not exactly an integer value, which creates a magnetic field gradient and displaces the saddle. In our first and second generation coils these effects were so strong that there was no saddle but a magnetic field gradient in the radial direction, which pulled the atoms out of the optical trap at very low trap depth. In our current coils, we greatly reduced this problem by using overlapping leads on the coils, but the saddle was still displaced by ~ 1 mm. We will describe how we overcame this problem in Sect. 5.3.1.

4.5 Imaging systems

The primary method to probe ultracold gases is to use the scattering of near-resonant light by the atoms. One way is to illuminate the atoms and measure their fluorescence, but this method has the disadvantage that the atoms emit into the whole solid angle and all fluorescent light not captured by the imaging system is lost. Therefore it is usually better to shine a light beam onto the atoms and observe the shadow cast by the cloud of atoms with a CCD camera, as in this case the signal consists of all photons scattered out of the aperture of the imaging system. This technique is called resonant absorption imaging.³

Here we will only look at the case of an imaging beam which is so weak that one can neglect the population of the excited state (for a discussion of other cases see

³One should note that in either case the sample is destroyed by the imaging light, as the recoil of the scattered photons blows the atoms away.

[Ott10]). In this case the absorption is described by the Lambert-Beer law

$$I(x, y) = I_0(x, y) \int e^{-\sigma n(x, y, z)} dz, \quad (4.8)$$

where z is the imaging direction and the cross-section is given by

$$\sigma = \frac{3\lambda^2}{2\pi} \quad (4.9)$$

for a closed transition driven with σ -polarized light along the quantization (i.e. magnetic field) axis.⁴ In principle one could directly compute $n(x, y)$ from a single image, but this would require precise knowledge of $I_0(x, y)$. Unfortunately creating homogeneous imaging beams is very difficult, as laser light is prone to interference effects. However, if the interference pattern on the imaging beam evolves slowly, which is usually the case, one can solve this problem by taking two images in quick succession. By taking one image with and one without the atoms one obtains the intensity of the imaging beam before (I_{ref}) and after (I_{abs}) it has passed through the atomic cloud. After subtracting a background image from these two images to remove the dark signal of the CCD one can divide the absorption by the reference image and obtains the relative transmission

$$T(x, y) = \frac{I_{abs} - I_{bg}}{I_{ref} - I_{bg}} = \frac{I(x, y)}{I_0(x, y)} = \int e^{-\sigma n(x, y, z)} dz \quad (4.10)$$

of the sample. From this we obtain the column density

$$n(x, y) = \int n(x, y, z) dz = -\frac{1}{\sigma} \ln T(x, y). \quad (4.11)$$

Thus the number of atoms imaged onto a single pixel of the CCD chip is given by

$$N_{pix}(x, y) = -\frac{A}{\sigma M^2} \ln T(x, y), \quad (4.12)$$

where A is the pixel size and M is the magnification. In our experiment we usually fit the transmission profile first (e.g. with a Gaussian for a thermal cloud) and then calculate the atom number from the area under the fitted curve. This eliminates offsets caused by a variation of the total intensity of the imaging beam between the absorption and reference image.

⁴When imaging perpendicular to the magnetic field one drives a π -transition with linearly polarized light, which reduces the cross section by a factor of two. Imaging with σ -polarized light in this direction reduces the cross section by a factor of four.

For the experiments described in this thesis we have used two different imaging setups in two different axes (see Fig. 4.6).⁵ The first setup images the dipole trap under an angle of 45° to its long axis onto an AVT Guppy F038B NIR CCD camera ("Guppy"). The second axis images the atoms along the MOT beam perpendicular to the long axis of the dipole trap onto a AVT Stingray F033B CCD camera ("Stingray"). For technical reasons (see [Ott10]) the imaging beam in this direction is circularly polarized, which reduces the cross section by a factor of four compared to Eq. 4.9.

The two imaging setups have been optimized for slightly different tasks. The Guppy axis with a higher cross section, lower magnification and a larger pixel size on the CCD chip has a higher signal to noise ratio than the Stingray axis. It is therefore well-suited for determining the atom number of low-density clouds and consequently it has been used for taking all data shown in chapters 5 and 6. The stingray axis has a higher resolution and is perpendicular to the long axis of the dipole trap, therefore it is much better suited to resolving structure in the atomic cloud (e.g. Fig. 2.8). It has also been used to determine trap frequencies with in-situ observation of the compression mode of a thermal gas in the trap as described in [Ott10]. Combining both imaging axes allows to triangulate the absolute position of the cloud, which is important for overlapping the dipole trap with the center of the magnetic field (see Sect. 5.3.1) or the microtrap (see [Zür09, Ott10]).

4.6 Standard experiment cycles

In this section we will describe our standard procedures for creating a molecular BEC or a weakly interacting two-component Fermi gas. These procedures were established in [Lom08, Koh08] more than three years ago and have remained largely unchanged since then.

4.6.1 Creating a molecular BEC

Our experimental cycle starts with loading the MOT for one second, after which the MOT contains $\sim 1 \times 10^8$ atoms.⁶ During the loading stage the MOT is relatively far detuned ($\sim 7 \Gamma$), which leads to a large capture radius and consequently optimizes the loading rate (see Sect. 4.2). However, at this detuning the MOT is

⁵There is a third high-NA imaging setup in the vertical axis, which can be used for high-resolution imaging and creating an optical microtrap (see [Zür09, Ott10, Ser11]), but this setup was not used in the experiments described in this thesis.

⁶A higher oven temperature could easily reduce this time by a factor of five, but the Lithium in the oven is used much more efficiently at lower temperature.

quite large and "warm" (about 1 mK), which is very bad for transferring atoms into the optical dipole trap. For the transfer we therefore ramp the detuning close to resonance, which causes the MOT to become cold and dense (see Eq. 4.1 and Fig. 4.2). However, the high density and the presence of near-resonant light result in high losses through light-assisted collisions, which can rapidly depopulate the MOT. Therefore the transfer of the atoms from the MOT into the optical dipole trap has to be done on a timescale of a few milliseconds.

To load the optical dipole trap we ramp the detuning of the MOT beams close to resonance over ~ 10 ms, while reducing the intensity of the MOT beams at the same time to reduce losses due to light-assisted collisions. This results in a cold and dense MOT ($T \sim 200 \mu\text{K}$, phase space density $\rho \sim 1 \times 10^{-5}$), from which we load the optical dipole trap. During the intensity ramp we switch off the repumper slightly faster to achieve optical pumping of the atoms to the $F = 1/2$ state. This state consists of two magnetic sublevels (states $|1\rangle$ and $|2\rangle$ in our notation) which are stable against two-body collisions in the dipole trap.

By ramping the dipole trap laser up to full power in the last five milliseconds of the MOT compression we load about 2×10^6 atoms into the optical dipole trap. As the $F = 1/2$ state consists of two magnetic sublevels we directly obtain the spin mixture we need for evaporative cooling.

To optimize the evaporation efficiency one would like to hold these atoms in the trap until plain evaporation stagnates before beginning forced evaporation. Unfortunately this is not possible in our case, as the high laser power of more than 200 W creates thermal lensing effects in the optics, which cause the shape of the trapping beam to deteriorate on a timescale of a few tens of milliseconds. Therefore we switch on the interparticle interactions immediately after the transfer of the atoms into the dipole trap by jumping to a magnetic field of $B = 760$ G and then ramp down the power of the fiber laser to ~ 40 W over a few hundred milliseconds. Further details concerning the transfer and initial evaporation procedure can be found in [Lom08].

After this reduction in laser power thermal effects are no longer an issue and we can perform further evaporative cooling by lowering the laser power in the dipole trap with an AOM. For the evaporation ramp we use a scheme for evaporative cooling of resonantly interacting Fermi gases developed in the group of J. Thomas [Luo06]. As soon as $k_B T \sim E_B$ molecules are formed by three-body collisions, and for $k_B T \ll E_B$ the gas consists almost entirely of molecules. After a total evaporation time of ~ 3 s these molecules condense into an almost pure BEC of $\sim 1 \times 10^5$ molecules (see Fig. 4.8). This shows that our evaporation is extremely efficient: We gain five orders of magnitude in phase space density, while only losing about a factor of ten in particle number. This is due to the high thermalization rate in our sample, which is caused by the large scattering cross section of the resonantly interacting particles. This also makes evaporation extremely robust: Even

reducing the initial particle number by a factor of ten does not prevent us from reaching a BEC at the end of the evaporation.

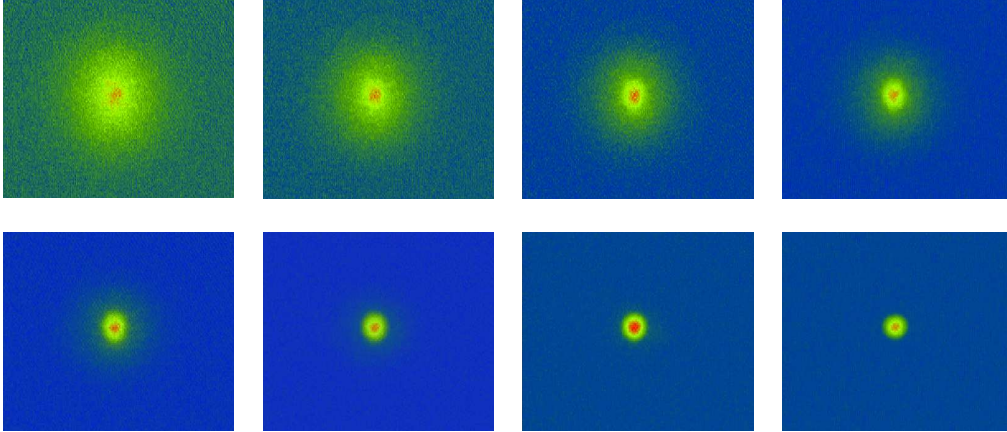


Figure 4.8: Time of flight images of a molecular cloud showing the transition from a thermal gas to a BEC. Observing the bimodal distribution of condensate and thermal cloud is difficult for ${}^6\text{Li}_2$ molecules, as the strong mean-field interaction lets the condensate expand almost as quickly as the thermal atoms. Therefore the interactions were switched off just after releasing the molecules from the trap by jumping to a magnetic field far below resonance. After the cloud had expanded the magnetic field was ramped back up to image the molecules.

Creating imbalanced gases

After loading the dipole trap from the MOT the sample contains a little more atoms in state $|1\rangle$ than in state $|2\rangle$. During evaporation the relative imbalance in the sample grows, as atoms from the two states are lost at the same rate. Therefore we usually apply an RF-pulse on the $|1\rangle$ - $|2\rangle$ transition during the initial evaporation. Due to the strong interactions in the gas there is strong decoherence and we quickly obtain a balanced mixture of atoms in the two spin states. If we want to create samples with a certain imbalance we simply vary the strength and/or duration of this RF-pulse. We have found this to be a well-defined procedure which allows us to tune the relative imbalance of the sample with an accuracy better than 10%. An example of such an imbalanced cloud can be seen in Fig. 2.8.

4.6.2 Creating a weakly interacting Fermi gas

While a molecular BEC can be a starting point for many fascinating experiments, most of our experiments actually start from a cold (but not necessarily very de-

generate) Fermi gas with weak interactions.⁷ In principle converting a molecular BEC into a weakly interacting Fermi gas is simple: One just has to ramp the magnetic field across the Feshbach resonance and dissociate the molecules (see Sect. 2.5). However, in ${}^6\text{Li}$ the scattering length converges to the triplet background scattering length $a_{tr} \approx -2200 a_0$ for high magnetic fields (see Sect. 2.6), which makes it impossible to create a weakly interacting Fermi gas above resonance.⁸ The only magnetic field region where the regime of weak interaction can be accessed is around $B = 550 \text{ G}$, where all scattering lengths cross zero (see Fig. 4.9). However, starting from a molecular BEC or a degenerate Fermi gas above resonance and decreasing the magnetic field always leads to an adiabatic ramp into the molecular state, as the resonance is too broad to perform non-adiabatic jumps across it.

To create a weakly interacting degenerate Fermi gas we therefore have to modify our evaporation scheme. We follow the same approach as for the creation of a molecular BEC up to the point where $k_B T \gtrsim E_B$, but before the temperature becomes so low that the sample begins to contain a significant fraction of molecules we stop the evaporation and jump to a magnetic field of $B = 300 \text{ G}$. There the scattering length a_{12} has a value of $-300 a_0$, so no weakly bound dimer state exists. This scattering length is still large enough to perform efficient evaporation, but as the scattering rate is much lower than at a magnetic field of $B = 760 \text{ G}$ the evaporation takes longer (up to ten seconds for the entire evaporation procedure). A more serious limitation is that the cooling rate decreases strongly as the gas reaches quantum degeneracy. As the temperature is reduced, the Fermi sphere fills up and the number of unoccupied states decreases. Therefore the number of final states available for scattering particles decreases as well. This severely reduces the probability that a particle scatters into one of these holes in the Fermi distribution and therefore slows down thermalization. This is a direct consequence of the Fermi statistics of the particles. In our case, this causes evaporative cooling to stagnate at $T/T_F \approx 0.2$. This is quite warm compared to the values of $T \lesssim 0.05 T_F$ which can be reached by evaporative cooling of molecules or resonantly interacting pairs, which can thermalize via collisions of bosonic pairs.

However, for the studies of few-body physics discussed in this thesis having a degenerate gas is actually not helpful, as the resulting many-body effects complicate the evaluation of the results. For these experiments we therefore usually stop evaporation at $T/T_F \approx 1$ where the effects of degeneracy are practically non-existent. Typical parameters are $N_1 \approx N_2 \approx 10^5$ atoms, $T \approx 1 \mu\text{K}$ and trap

⁷At the time of writing this thesis we have not felt the need to create a molecular BEC in our lab for more than a year.

⁸This is actually one of the very few inconvenient properties of ${}^6\text{Li}$, but without this resonant background scattering length the ${}^6\text{Li}$ Feshbach resonances would not have such an exceptional width.

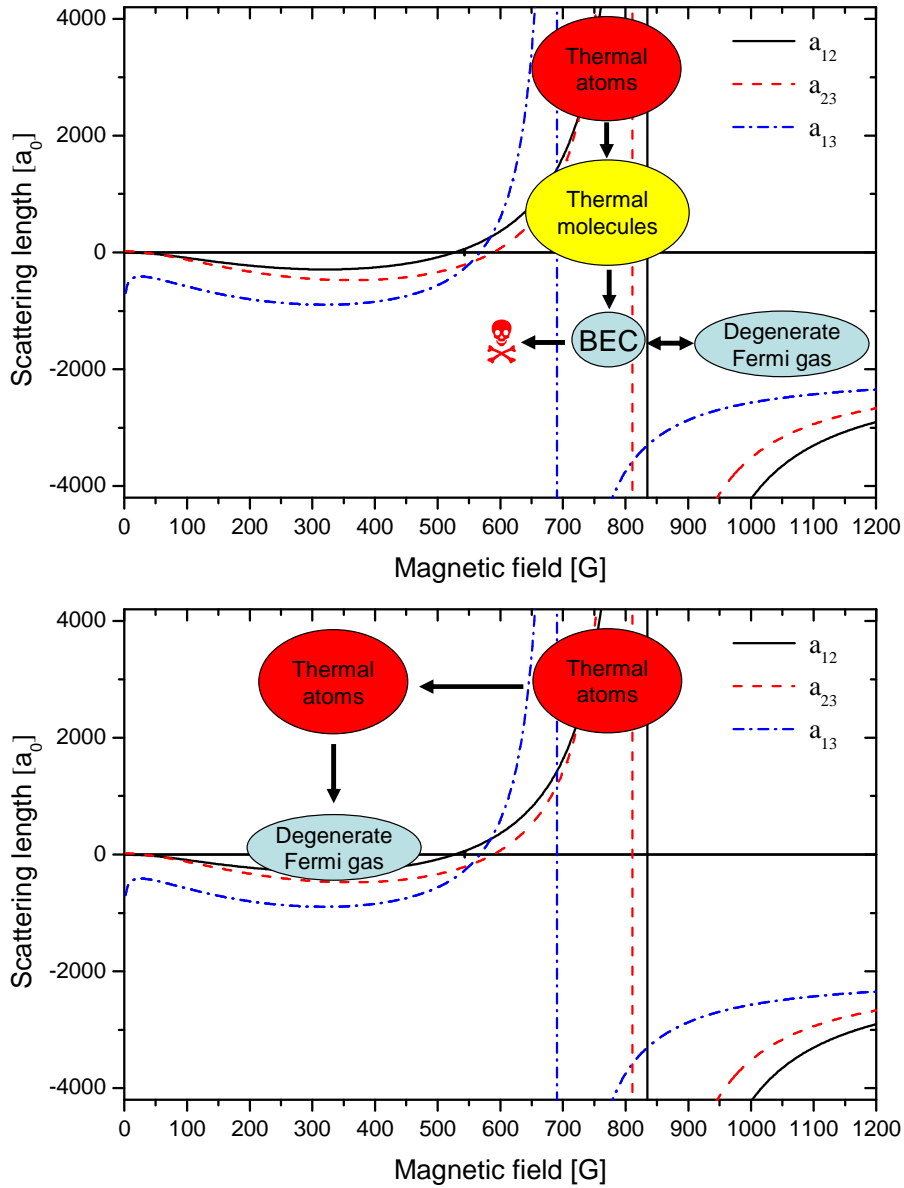


Figure 4.9: Sketch of the different evaporation schemes used to create molecular BECs (top) and weakly interacting degenerate Fermi gases (bottom). To create a BEC, atoms are evaporatively cooled until they form molecules, which after further evaporation eventually condense into a molecular BEC. This BEC can be converted into a degenerate Fermi gas by ramping across the Feshbach resonance, but for low magnetic fields the molecules become non-universal and rapidly decay in inelastic two-body collisions. To create a weakly interacting degenerate Fermi gas the atoms are cooled to a temperature $k_B T \gtrsim E_B$ close to resonance, then the magnetic field is switched to $B = 300$ G and the atoms are cooled to degeneracy.

frequencies of $\omega_{rad} \approx 820$ Hz and $\omega_{ax} \approx 75$ Hz. Temperature and particle number are measured by absorption imaging of the cloud after time-of-flight, while the trap frequencies are determined by exciting a compression mode in the cloud with a sudden change in trap depth and measuring its oscillation frequency with in-situ absorption imaging (see e.g. [Ott10]).

Chapter 5

Studying Efimov physics by observing collisional loss

As mentioned in Sect. 3.6 Efimov states are usually observed via their effects on three-atom and atom-dimer collisions. The simplest experimental approach to studying these effects in ultracold gases is to hold a sample of atoms and/or dimers in a trap, vary the scattering properties of the particles with a Feshbach resonance and measure the rate at which the particles are lost from the trap. In this chapter we present the studies of the Efimov physics of ${}^6\text{Li}$ we performed using this method, before moving on to the new technique of RF-association spectroscopy in chapter 6.

The first section describes how we create a three-component Fermi gas. This is followed by a brief summary of the results we obtained by studying the collisional properties of this gas in the magnetic field region below $B \approx 500$ G, which we will call the "low-field region" (see Fig. 5.1). The second part of the chapter focuses on the "high-field region" above $B \approx 600$ G, where we performed measurements of three-body recombination in a three-atom gas and studied the collisional behavior of the different atom-dimer mixtures. In both of these regions the scattering lengths are generally much larger than the range of the ${}^6\text{Li}$ interaction potential, so the few-body physics in these regions should be universal.

For the sake of readability we will not recount our measurements and the interpretation of their results in chronological order. Instead we will rearrange and group results to allow a clear and concise presentation. We will begin with a description of our three-body recombination measurements in the low- and high-field regions, followed by a discussion of the measurements we performed on the different atom-dimer systems. The chapter closes with an overview of the spectrum of Efimov states in ${}^6\text{Li}$ as it was determined from these collision experiments.

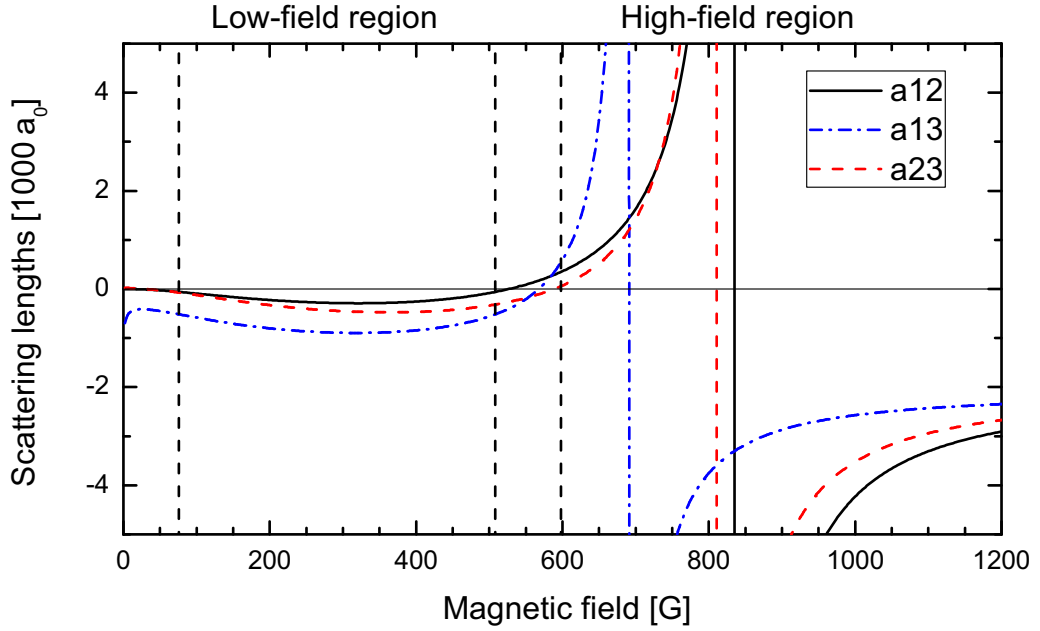


Figure 5.1: Scattering lengths in the low- and high-field region. The dashed lines mark the borders of the areas where the absolute values of all scattering lengths are larger than the van-der-Waals range $r_{vdW} \approx 60 a_0$ of ${}^6\text{Li}$.

5.1 Creating a three-component Fermi gas

To create a three-component Fermi gas we first prepare an imbalanced two-component Fermi gas which contains twice as many atoms in state $|1\rangle$ as in state $|2\rangle$ at a magnetic field of 300 G using the methods described in Sect. 4.6. To turn this two-component mixture into one with three components we need to change the internal state of a certain fraction of the atoms to state $|3\rangle$. As described in Sect. 2.6 the internal state of our atoms is determined by the projection of their nuclear spin on the magnetic field (see Fig. 2.5). This spin can be flipped by applying an oscillating magnetic field with frequency ν , where $h\nu$ is the energy splitting between the different spin states. This effect is called nuclear magnetic resonance (NMR). In our case, the levels have energy splittings of $\nu_{12} \sim 75$ MHz and $\nu_{23} \sim 82$ MHz, so the coupling of these levels is done with radio-frequency (RF) fields. As the splittings depend only weakly on the magnetic field, the transitions can be addressed with sub-kHz precision. Aside from allowing the preparation of ultracold atoms in different spin states, these transitions can also be used to probe the properties of ultracold gases. This will be discussed in chapter 6.

To create a three-component Fermi gas we first ramp the magnetic field to a value of 563 G, where all three scattering lengths are small. As three-body losses scale

with a^4 , the three-component gas has a long lifetime in this magnetic field region (see Sect. 5.2). In our first experiments [Ott08] we started with a balanced two-component Fermi gas and applied an RF-signal on both the $|1\rangle - |2\rangle$ and $|2\rangle - |3\rangle$ transitions. This causes Rabi oscillations between the states, which dephase due to collisions and magnetic field inhomogeneities. Thus we could create balanced three-component Fermi gases.

In later experiments we used a more elegant preparation technique based on rapid adiabatic passages, which allow us to coherently transfer population between different spin states. To perform such a passage between e.g. states $|1\rangle$ and $|2\rangle$ we switch on a coupling between the states which is far detuned from resonance and adiabatically sweep the frequency across the resonance. The coupling creates an avoided crossing between the two states, which leads to a transfer of the atoms from state $|1\rangle$ to state $|2\rangle$ and vice versa. The great experimental advantage of this technique is that the exact position of the resonance is uncritical, as the passage starts and ends at a large detuning. This makes this technique much less sensitive to drifts of experimental parameters than e.g. a π -pulse.

The adiabaticity criterion is given by comparing the sweep rate to the square of the Rabi frequency Ω . For a sudden jump across the resonance, the system remains in its initial state. If the sweep rate is comparable to the Rabi frequency the atoms can be brought into superposition states of the form $\alpha|1\rangle + \beta|2\rangle$ and $\beta|1\rangle - \alpha|2\rangle$, where the values of the coefficients depend on the sweep rate. For very slow sweep rates the population of state $|1\rangle$ is completely transferred to state $|2\rangle$ and vice versa.

Our preparation process consists of two passages: The first is a slow passage between states $|2\rangle$ and $|3\rangle$ which transfers all particles from state $|2\rangle$ to state $|3\rangle$ (see Fig. 5.2). Then we perform a faster passage between states $|1\rangle$ and $|2\rangle$ which puts the atoms from state $|1\rangle$ into an equal superposition of states $|1\rangle$ and $|2\rangle$. One should note that particles in identical superpositions are still identical fermions, so after such a semi-adiabatic passage the sample is still a two-component Fermi gas. However, in the presence of collisions and magnetic field inhomogeneities these superpositions quickly decohere, leading to a three-component Fermi gas.



Figure 5.2: Preparation of a three-component Fermi gas from an imbalanced two-component gas using a series of rapid adiabatic passages.

Another important condition for performing an efficient adiabatic passage is that the collision rate between the particles must be so low that only a negligible

amount of collisions occurs during the sweep, otherwise decoherence will reduce the transfer efficiency. This is easy to achieve for a weakly interacting gas close to the zero-crossings of the scattering lengths, but can be quite challenging in the high-field region where the scattering lengths are large.

5.2 Three-body recombination in the low-field region

After creating our first three-component gases we measured the rate constant for three-body recombination K_3 as a function of magnetic field in the low-field region where the scattering lengths are generally negative and have a local maximum in $|a|$ at $B \approx 300$ G (see Fig. 2.6). To measure K_3 at each magnetic field value we first recorded the fraction of atoms remaining in each of the spin states after different hold times. We then fitted the resulting loss curves by numerically solving a set of coupled differential equations which describe the evolution of density and temperature in the system (for details on the fitting procedure see [Ott08, Wen09a, Ott10]). The results are plotted in Fig. 5.3.

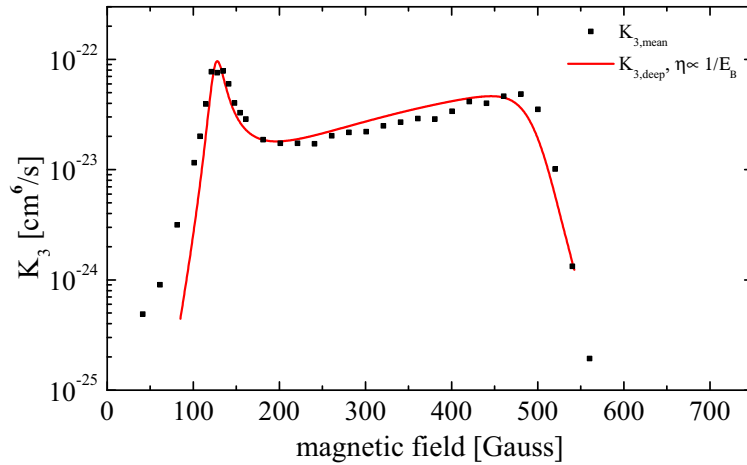


Figure 5.3: Three-body loss rate coefficient K_3 in the magnetic field region below 600 G. There are two distinct loss maxima at 127 G and 500 G, which are caused by the crossings of an Efimov state with the continuum. The red line is a fit to the data according to Eq. 3.39 using the effective scattering length from Eq. 3.47, leaving the normalization free. The difference in the width of the resonances is caused by a variation of the coupling of the trimer state to the deep dimers with the magnetic field. This is taken into account in the fit by varying the elasticity parameter η_* .

We found two loss resonances at magnetic fields of 127 G and 500 G. By defining the effective scattering length given in Eq. 3.47 we were able to fit both features using the formula derived for identical bosons. We found very similar three-body parameters of $a_*^- \approx -300a_0$ for both features, but the inelasticity parameters η_* were quite different. We therefore introduced a magnetic field variation of the inelasticity parameter, which was motivated by the fact that the binding energy of the deep dimers closest to the continuum changes drastically in this magnetic field region (see [Wen09a, Wen09b, Ott10]). This heuristic approach allowed us to obtain good quantitative agreement with the data and was later confirmed by a more careful theoretical study [Rit10].

5.3 Going to the high-field region

After obtaining an understanding of the three-body physics in the low-field region, it was the natural next step to study the Efimov physics occurring in the vicinity of the Feshbach resonances in the high-field region. As the situation can be quite complicated if one or more of the scattering lengths are positive (see Sect. 3.5), we decided to start with magnetic fields $B > 834$ G where all scattering lengths are once again negative. However, there were some significant technical challenges that had to be overcome before we could study the three-body loss in this region.

5.3.1 Lowering the collision energy

To get an idea what to expect in the high-field region, we assumed that the three-body parameter was the same in the high- and low-field region. One should note that it was by no means clear that this would be the case, a change of the three-body parameter with the magnetic field had for example been observed in [Kra06]. However, we considered it a reasonable assumption as we found no significant change of a_*^- between the two low-field resonances, which were almost 400 G apart.

For this three-body parameter, the lowest Efimov trimer would remain bound above the resonances due to the large background scattering lengths of $\sim -2200 a_0$. The next trimer of the series would be expected to cross the three-atom threshold at a scattering length of $\sim 22.7 \times 300 a_0 \approx 6800 a_0$. At such large scattering lengths the fact that the temperature limit of the three-body loss rate can hide the resonances becomes a serious concern (see Sect. 3.4.3). If we take a look at Fig. 3.7, we see that a collision energy of $E \lesssim k_B \times 50$ nK is required to observe this loss feature, compared to a temperature limit of $E \lesssim k_B \times 20\mu$ K for our experiments in the low-field region. Additionally, if the experiments were done at

the same density, the loss would occur on a timescale comparable to the duration of the magnetic field ramps, which would smear out the resonances .

Time-averaged potentials

For our experiments in the low-field region we used a three-component Fermi gas with a temperature of $T \approx 215$ nK and a degeneracy of $T/T_F \approx 0.35$. Making this gas colder would not help to observe higher loss rates, as for a degenerate gas the average kinetic energy of the particles is given by the Fermi energy $E_F = (6N)^{1/3} \hbar\bar{\omega}$. Additionally, it is much harder to model three-body loss in a deeply degenerate Fermi gas compared to a thermal gas with a simple Gaussian density distribution. To reduce the kinetic energy one can therefore either reduce the particle number or the mean trap frequency $\bar{\omega}$.

Reducing the particle number leads to a linear loss in signal, but the reduction of the kinetic energy scales only with the third root of N . This is therefore not a good option.

The simplest way to reduce the trap frequency is to reduce the depth U of the potential by lowering the laser power in the optical dipole trap. However, this reduces the number of quantum states in the trap and leads to a spilling of atoms from the trap when $U \approx E_F$. Consequently, reducing the trap frequency at constant particle number requires increasing the size of the trap. However, the high density and collision rate in a tight trap are extremely helpful for fast and robust evaporative cooling (see Sect. 4.6). Therefore changing the setup of the optical dipole trap to achieve a larger focus is not desirable.

The solution to this problem is to use two crossed AOMs to deflect the trapping beams, which changes the position of the focus. By using the AOMs to move the trap around with a speed that is much larger than the trapping frequency one can create a time averaged potential that is much larger than the original trap. The limit of this technique is that the laser beam has to fulfill the Bragg condition when it is deflected by the AOM. Consequently, the orientation of the AOM defines the optimum deflection angle. Changing the deflection angle therefore reduces the diffraction efficiency. This can be compensated by creating a map of the diffraction efficiency versus deflection angle and applying more power at large deflection angles where the diffraction efficiency is low. This allows us to increase the radial trap size by a factor of four.¹ More details about the generation of time-averaged potentials can be found in [Lom08, Koh08, Ott10].

To prepare a low-energy three-component Fermi gas we first create a two-component Fermi gas as described in Sect. 4.6. Then we adiabatically increase the trap size

¹It is possible to reach larger deflections by using acousto-optic deflectors (AODs) instead of AOMs, but these have a lower peak diffraction efficiency, which makes them unsuitable for our setup.

using the AOMs, while adjusting the laser power to prevent further evaporative cooling that would lead to a degenerate gas. This results in a two-component Fermi gas with a temperature of $T \approx 50$ nK. The density of this gas is about an order of magnitude lower than it is in the tight trap. Typical trap frequencies of the time-averaged potential (which were measured by in-situ observation of a compression mode in the trapped gas) are $\omega_{rad} \approx 100$ Hz and $\omega_{ax} \approx 15$ Hz, where the axial trap frequency is dominated by the curvature of the Feshbach field.

To measure the temperature of such a cold gas we can no longer use the technique of time-of-flight imaging, as the effect of the magnetic potentials is comparable to the expansion energy of the gas. Instead, we use the size of the cloud in the harmonic potential to determine the temperature according to

$$T = \frac{m\sigma^2\omega^2}{k_B}, \quad (5.1)$$

where σ is the $1/\sqrt{e}$ radius of the cloud and ω is the trap frequency in the respective axis. This technique has the disadvantage that it requires the trap frequency as an additional input, which can lead to an increased uncertainty. However, in our case the axial trap is given by the magnetic field curvature, which is very smooth and allows for an accurate determination of this frequency.

Alignment of the dipole trap

One of the most critical aspects for creating very weak optical potentials is the position of the optical dipole trap relative to the magnetic field coils. While aligning the position of the dipole trap is a simple experimental procedure, it has to simultaneously fulfill several seemingly contradictory conditions:

During the transfer of the atoms from the MOT to the optical dipole trap, the dipole trap has to be overlapped with the center of the MOT to obtain a good transfer efficiency. The position of the MOT is defined by the zero of the magnetic quadrupole field, which we create by driving the Feshbach coils in anti-Helmholtz configuration. The position of the zero of the magnetic field is in the geometric center of the coil. Due to the steep magnetic field gradients at this point this position is largely insensitive to stray fields or imperfections of the coils.

After the transfer we switch the polarity of one of the Feshbach coils and use them to create magnetic offset fields. For very weak optical traps, the potentials caused by inhomogeneities in this offset field become important. To prevent the atoms from being pulled out of the dipole trap its center has to be overlapped with the saddle of the Feshbach field. Unfortunately, this saddle is very shallow and therefore highly sensitive to imperfections in the coils. Without compensation, it is about a millimeter away from the position of the MOT during transfer. Creating very shallow traps requires that the dipole trap is overlapped with both the zero (in

anti-Helmholtz configuration) and the saddle point (in Helmholtz configuration) of the Feshbach coils.

Let us first consider how difficult it is to move these points in different directions: Moving both the zero and the saddle point in axial direction can be easily achieved by superimposing a magnetic field gradient in this direction. During the experiments in the dipole trap we already use this technique to compensate for the effect of gravity, which would otherwise pull the atoms out of the trap much earlier than the magnetic field inhomogeneities. However, using the gradient to compensate for the displacement of the saddle would require to adapt the strength of the gradient to the strength of the Feshbach field. Therefore it is much more convenient to align the vertical position of the dipole trap with the saddle point of the Feshbach field and move the zero of the MOT field to the correct position. To achieve this, we add a bypass resistor to one of the coils, which we can activate with a MOSFET. This reduces the current in the coil and moves the center of the quadrupole field. Thus we can shift the vertical position of the MOT by simply changing the resistance of the bypass with a potentiometer. This setup has the additional advantage that the position of the MOT depends only on the ratio of the currents in the coils, so we can change the value of the MOT gradient without having to readjust the position.

In the radial direction, things are a little more tricky. As we need relatively strong gradients of ~ 30 G/cm to compress the MOT for the transfer, compensation coils that could move the MOT far enough would be bulky and therefore very annoying, as space close to the experimental chamber is limited. Moving the position of the saddle with compensation coils is even more impractical, as we would have to apply a correction perpendicular to an offset field of ~ 800 G, which would be quadratically suppressed. Therefore the best option seemed to be to improve the Feshbach coils to move the position of the saddle point closer to their geometric center.

However, designing and building a new set of coils would have required a great amount of work. Additionally, it was by no means clear whether new coils could completely solve the problem, as the imperfections of the current generation were already quite small. Therefore we came up with a method to compensate for the imperfections of our Feshbach coils.

To move the saddle point of the Feshbach field to the position of the dipole trap (which was overlapped with the position of the MOT) we first created molecular BECs in very shallow traps. We then released them from the trap to use them as a probe for the magnetic potential by triangulating their position after a time of flight using absorption images from two different directions (see Fig. 4.6 for the setup of the imaging systems).² We then placed small blocks of ferromagnetic

²The reason for using a molecular BEC is that in the same trap it has a much lower chemical

steel close to the Feshbach coils to locally enhance the magnetic field and thus move the position of the saddle point. To avoid moving the saddle in the vertical direction we always placed blocks at both coils simultaneously. In an iterative process this allowed us to overlap the positions of the zero of the MOT field and the saddle point of the Feshbach field with an error of less than a few tens of micrometers.

5.3.2 Predictions from theory

After we had established these techniques, we were ready to explore the high-field region. However, in the meantime the group of K. O’Hara had already observed a loss resonance in the high-field region at $B \approx 895$ G [Wil09].³ The three-body parameter extracted from the position of this resonance agrees very well with the value found in the low-field region. Using this parameter as an input, E. Braaten et al. soon calculated the binding energies of the trimer states as a function of magnetic field [Bra10] (see Fig. 5.4). They found that there were two Efimov states in the ${}^6\text{Li}$ system; the ground state trimer that was observed in the low-field region and the next higher trimer state, which was observed in [Wil09]. As the three scattering lengths do not diverge at the same magnetic field value, there is always a finite scattering length which cuts off the scale-invariant region before a third trimer state can fit into the hyperradial potential (see Fig. 3.4). Therefore the series of Efimov states in ${}^6\text{Li}$ ends after these two trimer states.

From these calculations of the trimer binding energy one can also extract the expected positions of the intersections of these Efimov states with the atom-dimer threshold, which are marked by the dashed vertical lines in Fig. 5.4. They also computed the expected three-body loss rate in the high-field region (see Fig. 5.5). We quickly set out to verify these predictions with collision experiments and renewed our efforts to observe the trimer states with RF-spectroscopy.

5.4 Three-body recombination in the high-field region

To measure the three-body recombination rate in the high-field region we first prepared an imbalanced two-component Fermi gas using the techniques described in Sect. 4.6. Then we created a three-component mixture using a series of rapid

potential than a degenerate Fermi gas and therefore expands more slowly after it has been released from the trap.

³We had also spent some time working on the preparation of few-fermion systems (see [Zür09, Ott10]), and had to rebuild part of the optical setup of the dipole trap after a small mishap with the high-power laser had destroyed the AOMs.

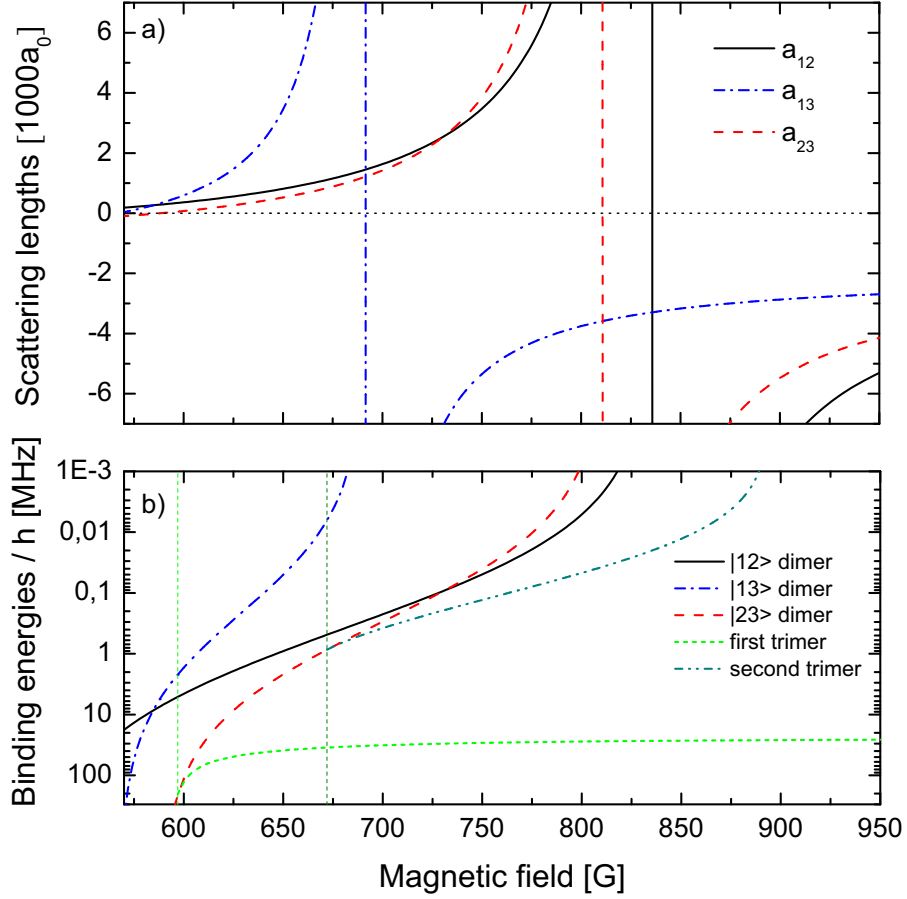


Figure 5.4: (a) Values of the scattering lengths in the high-field region. (b) Binding energies of the universal dimer and trimer states according to universal theory. There are three universal dimer states in the system ($|12\rangle$, $|23\rangle$ and $|13\rangle$), whose binding energies are calculated with Eq. 2.14 using the scattering lengths shown in the upper panel. The energies of the two universal trimer states were calculated in [Bra10] using universal theory. Due to the large background scattering length the first trimer state never becomes unbound above the resonance, while the second trimer crosses the three-atom threshold at $B \approx 895$ G. On the positive side of the Feshbach resonances the trimer states become unbound when their binding energies become degenerate with the binding energy of the most deeply bound dimer. For both trimer states this is the $|23\rangle$ dimer, they cross the $|1\rangle$ - $|23\rangle$ atom-dimer threshold at $B \approx 600$ G and $B \approx 672$ G.

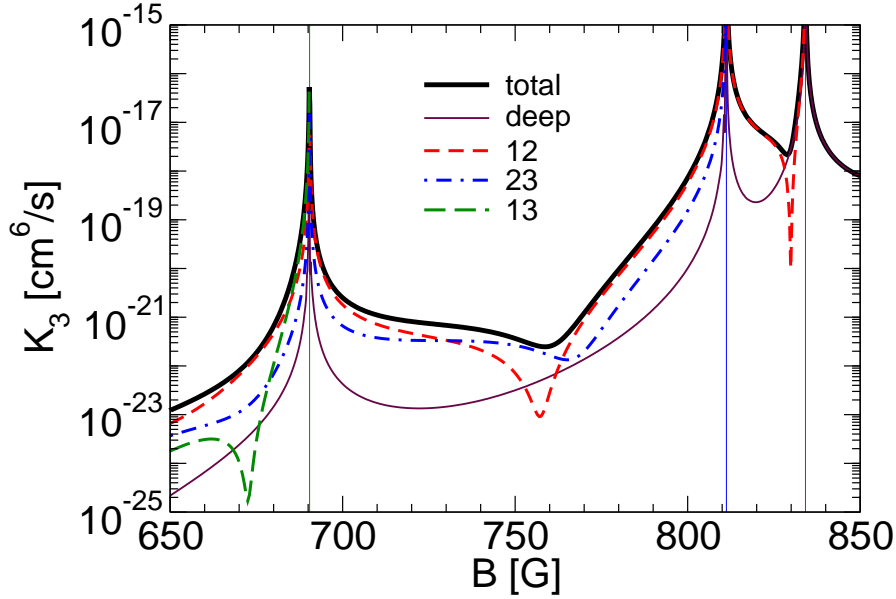


Figure 5.5: Predicted three-body recombination rate for a three-component Fermi gas of ${}^6\text{Li}$ as a function of magnetic field. The colored lines give the rates for recombination into the three different shallow dimers and the rate for direct recombination into deep dimers, while the thick black line shows the sum of all these recombination rates. The thin vertical lines mark the positions of the Feshbach resonances. One should note that the calculation only includes collisions involving three distinguishable fermions, while collisions involving two identical fermions are neglected. Figure taken from [Bra10].

adiabatic passages as described in Sect. 5.1. Finally we jumped to the magnetic field of interest, held the sample for different durations and recorded the number of remaining atoms in one spin state with absorption imaging. The loss curves were fitted according to equation 3.35. The results for two different runs are shown in Fig. 5.6. The red data points were measured in an extremely shallow trap with trapping frequencies of $\omega_{rad} \approx 40$ Hz and $\omega_{ax} \approx 13$ Hz, which was necessary for resolving the loss feature at $B \approx 900$ G. However, because of the low density three-body loss cannot be observed at small scattering lengths ($B \lesssim 650$ G) in this measurement. Due to the low density of the sample the signal-to noise ration of this measurement was too low to measure the temperature evolution of the cloud during the loss process. We therefore assumed a constant temperature for our analysis.⁴ Additionally there might be a slight systematic deformation of the

⁴This neglects the effect of heating by anti-evaporation, which lets the value of K_3 appear smaller than it actually is (see [Web03, Wen09a, Ott10]). To minimize this effect we only fitted

data, as the axial trap frequency - which is given by the curvature of the magnetic field - changes with the square root of the strength of the magnetic offset field, which was not taken into account. The blue data points are from measurements in somewhat tighter traps. To account for the different normalization in the different trapping geometries this dataset has been rescaled to coincide with the first one. While the data from these measurements is not suitable for a quantitative analysis without applying corrections for the issues mentioned above and fixing the absolute scale, it allows to get some valuable qualitative insight which we will discuss below.

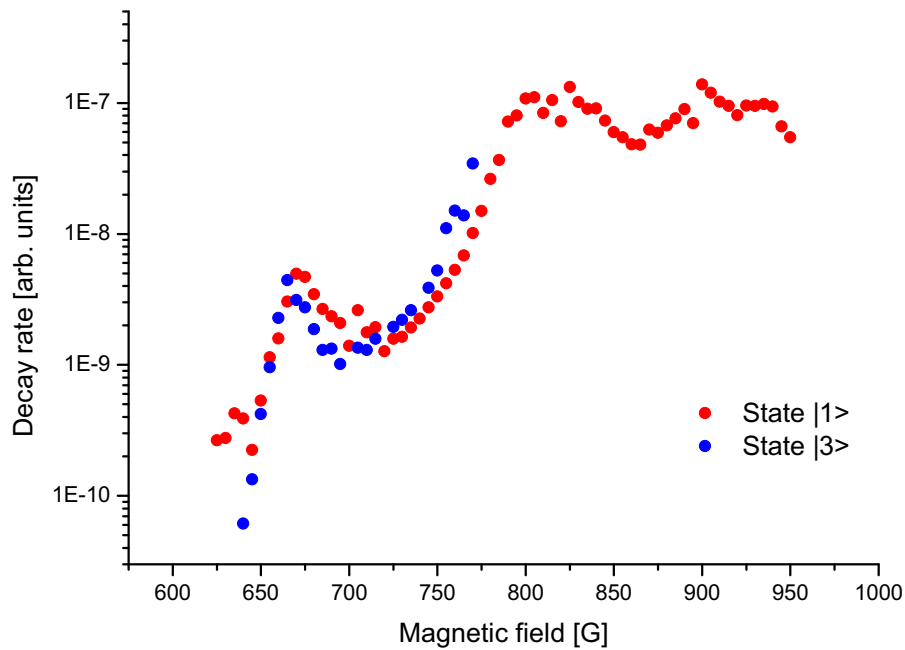


Figure 5.6: Decay rate of a three-component gas of ${}^6\text{Li}$ in the high-field region, measured by recording the atom number evolution in a shallow (red) and tighter (blue) traps. For the first dataset we measured the number of atoms in state $|1\rangle$, while for the second dataset state $|3\rangle$ was imaged. The loss resonance at $B \sim 900$ G observed first by [Wil09] is clearly visible, as well as an enhancement of the loss close to the $|12\rangle$ and $|23\rangle$ Feshbach resonances at 834 G and 812 G. Another – unexpected – loss maximum shows up at $B \approx 650$ G. The loss minimum predicted at $B \approx 760$ G (see Fig. 5.5) is not visible in the data.

The first observation is that we can reproduce the loss feature found at 895 G by J. R. Williams et al. [Wil09]. However, for magnetic fields below 834 G the data looks completely different than the prediction shown in Fig. 5.5. Neither the initial part of the loss curve where these effects are less important.

the predicted loss minimum at $B \approx 760$ G nor the maximum at the position of the $|1\rangle\text{-}|3\rangle$ Feshbach resonance at 690 G show up in the data. Instead, there is a clear maximum in the loss rate at a magnetic field of about 650 G, which is not predicted by theory.

To understand these differences we have to consider the effect of collisions involving two identical fermions. While these processes are usually strongly suppressed by Pauli blocking, the formation of weakly bound dimers is allowed for very large scattering lengths (see Sect. 2.7.2). In the magnetic field region just below the $|1\rangle\text{-}|3\rangle$ Feshbach resonance $a_{13} \gg a_{12} \approx a_{23}$. Therefore the formation of $|13\rangle$ -dimers in $|1\rangle\text{-}|1\rangle\text{-}|3\rangle$ or $|1\rangle\text{-}|3\rangle\text{-}|3\rangle$ collisions becomes the dominant loss process. If these dimers are not lost from the trap upon formation, they are lost in subsequent $|2\rangle\text{-}|13\rangle$, $|1\rangle\text{-}|13\rangle$ and $|3\rangle\text{-}|13\rangle$ atom-dimer collisions as well as $|13\rangle\text{-}|13\rangle$ dimer-dimer collisions. This dimer formation explains the increase in the loss rate at $B \approx 650$ G.

In the vicinity of the $|1\rangle\text{-}|3\rangle$ Feshbach resonance the $|13\rangle$ -dimers become stable against losses in collisions involving identical fermions (see Sect. 2.7.1). Therefore the only loss process for these dimers are $|2\rangle\text{-}|13\rangle$ atom-dimer collisions, which are also suppressed in the vicinity of the $|1\rangle\text{-}|3\rangle$ Feshbach resonance (see Sect. 5.5.4). This explains the absence of the predicted loss maximum at $B = 690$ G.

In the magnetic field region above $B \approx 730$ G all scattering lengths are large and of similar magnitude. Therefore the formation of shallow dimers is possible in a large number of processes. Under these circumstances it would not be surprising for the predicted loss minimum at 760 G to be masked by other processes.

So despite first appearances to the contrary, our data actually does not contradict the prediction from Fig. 5.5. Our measurements just probe a different quantity, as the loss processes involving three distinguishable particles shown in Fig. 5.5 are not the only ones occurring in our system.

After obtaining a qualitative understanding of these measurements, we have to ask ourselves whether they are a suitable tool to probe the physics we are interested in, namely the properties of the Efimov trimers. To do this would require extracting quantitative information about the rate of three-body collisions involving three distinguishable particles. This is only possible if we have information about the rates for three-body recombination involving identical fermions as well as all possible inelastic atom-dimer and dimer-dimer collisions (or at least convincing arguments why we could neglect a specific process). Under these circumstances it seemed much easier and a lot more elegant to directly obtain the desired information about the Efimov trimers in ${}^6\text{Li}$ by studying atom-dimer collisions in the $|1\rangle\text{-}|23\rangle$, $|3\rangle\text{-}|12\rangle$ and $|2\rangle\text{-}|13\rangle$ atom-dimer mixtures. These measurements are described in the next section.

5.5 Atom-dimer scattering

In this section we will describe our studies of atom-dimer collisions in the three different atom-dimer mixtures $|1\rangle$ - $|23\rangle$, $|3\rangle$ - $|12\rangle$ and $|2\rangle$ - $|13\rangle$. Creating these atom-dimer mixtures requires a rather elaborate preparation scheme which will be described using the $|1\rangle$ - $|23\rangle$ mixture as an example.

5.5.1 Creating atom-dimer mixtures

Our scheme for the preparation of a $|1\rangle$ - $|23\rangle$ atom-dimer mixture is shown in Fig. 5.7. We start with a thermal two-component gas with about twice as many atoms in state $|1\rangle$ as in state $|2\rangle$. We then expand the trap to create a low-temperature gas as described in Sect. 5.3.1. Then we perform two adiabatic passages at a magnetic field of 563 G where all scattering lengths are small. The first passage transfers the atoms in state $|2\rangle$ to state $|3\rangle$, the second drives the atoms in state $|1\rangle$ to state $|2\rangle$. This results in an imbalanced $|2\rangle$ - $|3\rangle$ mixture with more atoms in state $|2\rangle$.

Next, we jump to a magnetic field of 800 G, which is close to the $|2\rangle$ - $|3\rangle$ Feshbach resonance at 812 G. Then we lower the trap depth by a factor of two in a final stage of evaporative cooling. The final degeneracy of the gas is $T/T_F \approx 1$, which is well above the quantum degenerate regime.

At this field $a_{23} \approx 30000 a_0$, which leads to an extremely high rate for the formation of $|23\rangle$ dimers in $|2\rangle$ - $|2\rangle$ - $|3\rangle$ and $|2\rangle$ - $|3\rangle$ - $|3\rangle$ three-body collisions (see Sect. 2.7.2). According to Eq. 2.14 the binding energy $E_{23} \approx k_B \times 36$ nK, of these dimers is much smaller than the trap depth, so they remain in the trap and quickly form a chemical equilibrium with the atoms according to Eq. 2.44. Additionally, any atoms in state $|1\rangle$ left in the sample due to imperfect adiabatic passages are lost in inelastic collisions in this phase.

Subsequently we ramp the magnetic field down to values between 580 G and 740 G. We take care to choose a ramp speed which is slow enough that the sample stays in chemical equilibrium until almost all atoms in state $|3\rangle$ are bound in molecules. We verify this by jumping down to magnetic fields below 600 G where the molecules are tightly bound and therefore not visible with absorption imaging and imaging the number of atoms in state $|3\rangle$. These images showed that less than 5% of the atoms in state $|3\rangle$ remained unbound.

After the ramp to the magnetic field value of interest we end up with a $|2\rangle$ - $|23\rangle$ atom-dimer mixture containing roughly 5×10^4 state $|2\rangle$ atoms and 4×10^4 $|23\rangle$ -dimers at a temperature of $T = 60 \pm 15$ nK. The trapping frequencies in these experiments were $2\pi \times (102 \pm 5)$ Hz and $2\pi \times (112 \pm 5)$ Hz in the radial and $2\pi \times (15 \pm 1)$ Hz in the axial direction. One should note that while the molecules feel the same trap frequency as the atoms, the mass of the molecules is larger by

a factor of two. Therefore the extension of the molecular cloud is smaller by a factor of $\sqrt{2}$ (see Eq. 2.12), which reduces the overlap of atoms and dimers in the trap. Taking this effect into account, the final atomic and molecular densities were 1.5×10^{11} atoms/cm³ and 2×10^{11} molecules/cm³.

To prepare an atom-dimer mixture with a well defined ratio between atoms and dimers we first optimize the efficiency of this preparation scheme. Then we fine-tune the initial imbalance of state $|1\rangle$ and $|2\rangle$ after the initial evaporation. This can be done by changing the power and duration of the balancing pulse applied on the $|1\rangle$ - $|2\rangle$ transition during the first evaporation ramp until one obtains the desired ratio of atoms and dimers in the final mixture.

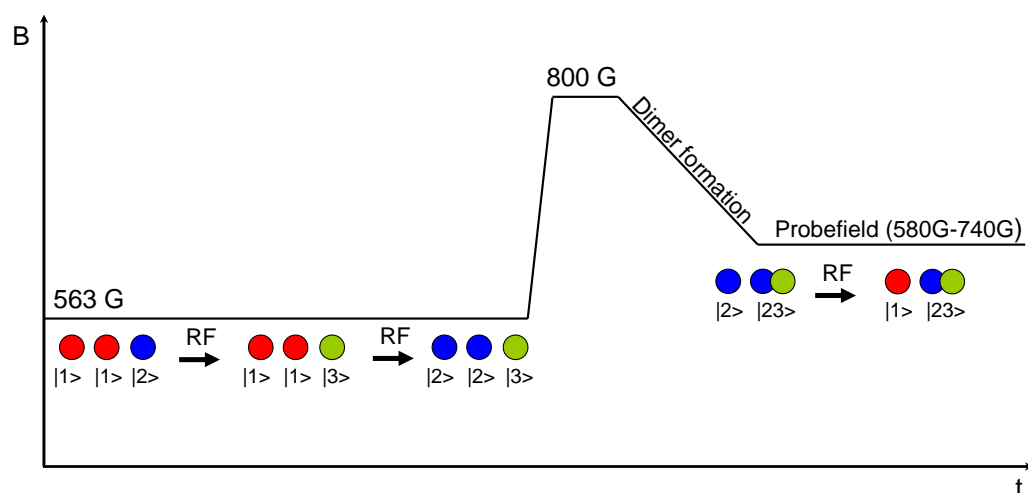


Figure 5.7: Sketch of the preparation scheme for the $|1\rangle$ - $|23\rangle$ atom-dimer mixture. Starting from an imbalanced $|1\rangle$ - $|2\rangle$ mixture close to the zero-crossings of the scattering lengths we prepare a $|2\rangle$ - $|3\rangle$ mixture with a series of rapid adiabatic passages. Then we jump to a magnetic field close to the $|2\rangle$ - $|3\rangle$ Feshbach resonance and slowly ramp to the desired magnetic field value. After this ramp all atoms in state $|3\rangle$ are bound in $|23\rangle$ dimers and we can drive the free atoms in state $|2\rangle$ to state $|1\rangle$ using another rapid adiabatic passage.

The last step of the preparation sequence is to populate the third state using an RF-transfer. As the transition frequency of the atoms bound in dimers is shifted compared to the free atoms, we can selectively address the unbound atoms in state $|2\rangle$ and drive them to state $|1\rangle$ using a rapid adiabatic passage. In the magnetic field region of interest the scattering lengths for both the initial and final mixture can be large. Therefore we have to perform this RF-transfer as quickly as possible to avoid decoherence. We achieved a maximum transfer efficiency of $\sim 90\%$ with a duration of the adiabatic passage of $500 \mu\text{s}$, compared to nearly 100% efficiency

with passage durations of tens of milliseconds in the low-field region.

As the frequency of the $|1\rangle$ - $|2\rangle$ transition depends on the magnetic field, it has to be recalculated for each magnetic field value. To simplify the data acquisition we modified our experiment control software such that the frequency range of the adiabatic passages was automatically calculated according to the magnetic field for each experimental run.

Using this scheme, we can create mixtures of free atoms in state $|1\rangle$ and $|23\rangle$ -dimers. The preparation of $|3\rangle$ - $|12\rangle$ and $|2\rangle$ - $|13\rangle$ mixtures follows the same scheme, but with a slightly altered sequence of adiabatic passages to produce the desired spin state combination.

One should note that this preparation scheme is unique to Fermi gases, as two-component Fermi gases are very stable against losses through atom-dimer and dimer-dimer collisions for large scattering lengths. For smaller scattering lengths the two-component system begins to decay via atom-dimer and dimer-dimer collisions, but the losses are low enough that we lose only a small amount of particles to these processes during the preparation.

5.5.2 The $|1\rangle$ - $|23\rangle$ mixture: Crossings of Efimov states

To study two-body loss in a $|1\rangle$ - $|23\rangle$ mixture as a function of magnetic field we first prepared samples at magnetic fields between 580 G and 740 G using the techniques described above. Then we recorded the number of remaining state $|1\rangle$ atoms over 120 ms using in-situ absorption imaging. To determine the two-body loss coefficient β_{1-23} from these measurements we have to fit the loss curves according to Eq. 3.41.

However, obtaining reliable values for the atomic and molecular densities is difficult for several reasons: The first is that for particle numbers below 10^4 the density is so low that the signal to noise ratio of the absorption images is insufficient to guarantee a reliable fit of the atomic density distribution.

A more serious problem is that both the inelastic collisions which lead to losses and the elastic collisions responsible for thermalization are two-body processes which scale with n^2 ; consequently the rates for both processes can be comparable (see Fig. 7.1). Additionally, for the highest loss rates the sample decays on a time scale of less than 10 ms, which is comparable to the mean trapping frequency of the system. Therefore it is questionable whether the sample stays in thermal equilibrium during the decay.⁵

As a quantitative treatment of such out-of-equilibrium effects is prohibitively complex, we only fitted the initial decay, where the effects of heating and anti-

⁵When measuring three-body loss this problem is much less severe, as the loss rate scales with n^3 .

evaporation should only be a small correction. If we assume that our sample is a thermal gas its density distribution is a Gaussian, which greatly simplifies the evaluation. To verify the assumption that out-of-equilibrium effects can be neglected for the initial decay we fitted the data up to different loss fractions of 0.3, 0.5 and 1. We found that fitting the data up to a loss fraction of 0.3 or 0.5 changes the result of the fit only by about 10%, which convinced us that this is a reasonable procedure.

In our experiment we are working with a gas of atoms and dimers in a harmonic trap. Consequently we have to average the differential equation 3.41 which describes the two-body loss over the density distributions of atoms and dimers in the trap, which leads to

$$\dot{N}_A = -\beta \int n_A(\mathbf{r}) n_D(\mathbf{r}) d\mathbf{r}^3. \quad (5.2)$$

In this equation we have neglected the effect of dimer-dimer collisions, which is a reasonable approximation if the rate constant for inelastic dimer-dimer collisions is much lower than the rate constant for atom-dimer loss. This condition is reasonably well fulfilled in the entire region where the scattering lengths are large enough that universal theory can be expected to make quantitatively accurate predictions (see Fig. 2.7). At fields below $B \approx 620$ G dimer-dimer collisions become more important, and can lead to a systematic shift of the measured atom-dimer loss rates to lower values as the fit overestimates the dimer density.

The differential equation 5.2 has the analytical solution

$$N_A(t) = \frac{(N_{D0} - N_{A0})}{\frac{N_{D0}}{N_{A0}} e^{(N_{D0} - N_{A0})\gamma t} - 1} \quad (5.3)$$

with $\gamma = \beta/(\sqrt{27}\pi^{\frac{3}{2}}\sigma_x\sigma_y\sigma_z)$, where σ_x , σ_y and σ_z are the $1/\sqrt{e}$ radii of the atomic cloud and N_{A0} (N_{D0}) is the initial atom (molecule) number at $t = 0$. To determine the values of the rate coefficients we first fitted the loss curves up to a loss fraction of 0.5 using Eq. 5.3. To obtain a value of N_{D0} for the fit we measured the initial number of molecules for each magnetic field value in a separate experiment. This was done by performing the same preparation sequence as for the loss measurement, but recording the number of dimers instead of transferring the free atoms to the third state. As the dimers are invisible to absorption imaging at low fields this required a jump close to the Feshbach resonance where the atoms bound in dimers can be imaged.

From the values of γ resulting from the fits of the atom-dimer loss curves we then computed the value of β_{1-23} for each magnetic field. The results are plotted in Fig. 5.8

The data shows two distinct loss features at magnetic fields of ~ 600 G and ~ 685 G, which is in good qualitative agreement with the prediction from [Bra10].

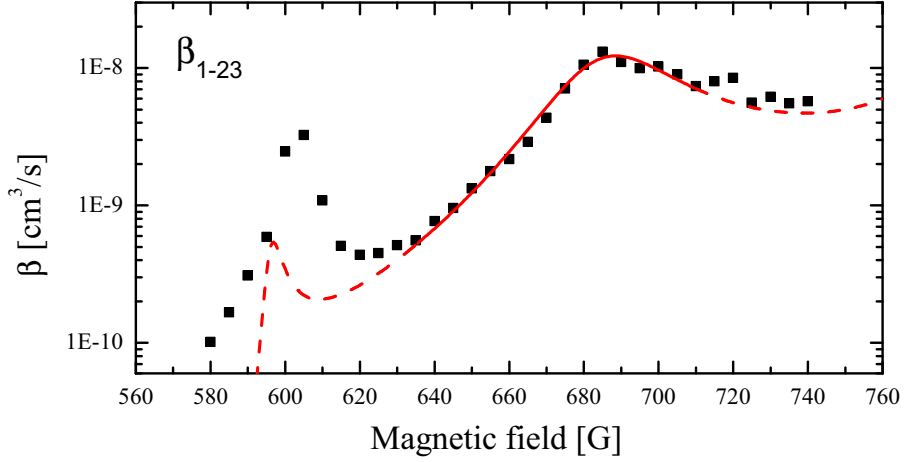


Figure 5.8: Atom-dimer loss coefficient β_{1-23} as a function of the magnetic field. There are two clear loss maxima at $B = 603$ G and $B = 685$ G, which we identify as the intersections of two Efimov trimers with the $|1\rangle$ - $|23\rangle$ atom-dimer threshold (see Fig. 5.4). The red line is a fit to the data according to Eq. 5.4, where the solid part of the line marks the data points included in the fit.

However, the measured positions of the resonances differ from the prediction by about 10 G for the upper and about 5 G for the lower resonance. For the lower resonance one would actually expect the prediction to be inaccurate, as $a_{23} \approx 80 a_0$, which is not much larger than the range $r_{vdW} \approx 60 a_0$ of the interaction potential. However, for the upper resonance all scattering lengths are much larger than the range of the interaction potential and one would expect universal theory to be quantitatively accurate in this region.

The first step to understanding this discrepancy is to fit the loss maximum at 685 G to obtain quantitative information. For magnetic fields where the $|23\rangle$ -dimer is the energetically lowest universal dimer state in the system, the only possible loss process is decay into deep dimers. According to [Bra10], the loss rate in the vicinity of the crossing of the second trimer state is described by

$$\beta_{1-23} = \frac{6.32 C \sinh(2\eta_*)}{\sin^2(s_0 \ln(a_{23}/a_*^+)) + \sinh^2 \eta_*} \frac{\hbar a_{23}}{m}. \quad (5.4)$$

This formula is very similar to Eq. 3.42, except for a different normalization constant which was calculated for the values of the three scattering lengths at 672 G. We have added a normalization constant C to this formula to account for systematic shifts of the measured loss coefficients due to errors in our determination of the particle density. The first source of error is the uncertainty of our measurements of the particle number, which comes mostly from the uncertainty of

the magnification of the imaging system (see Eq. 4.12). The uncertainty of the trapping frequency affects the result for the density directly via Eq. 2.12 and indirectly through the measurement of the temperature, which depends both on magnification and trap frequency. We estimate the systematic uncertainty from these sources of error to be about 85%, where $\sim 25\%$ come from the errors of the trap frequencies and $\sim 60\%$ come from a 10% error of the magnification.

As Eq. 5.4 only describes the relaxation into deep dimers, we can only fit the magnetic field range below 725 G where $E_{23} - E_{12} \gg k_B T$ as otherwise the $|12\rangle$ -dimer becomes allowed as a final state. Additionally, we restrict our fit to data points where $a_{23} > 5 \times r_0$. The result is plotted as a red line in Fig. 5.8 and shows good quantitative agreement for all data points included in the fit. The fit parameters are $a_*^+ = 1076 (1042, 1110) a_0$, $\eta_* = 0.34 (0.29, 0.39)$ and $C = 0.52 (0.47, 0.57)$, where the values in parentheses give the 95% confidence bounds of the fit. This corresponds to a resonance position $B_* = 685 \pm 2$ G. These parameters show a significant difference from the values of $a_*^+ = 835 \pm 24 a_0$ and $\eta_* = 0.016$ obtained from the three-atom resonance at 895 G in [Wil09].

There are several possible explanations for this discrepancy. One is that it might be a purely experimental effect caused by the finite collision energy of the particles. Another reason could be corrections to the universal theory due to the finite range of the interaction potential. And finally, the three-body parameter might be different at the positions of the three-atom and atom-dimer resonance, which would be in violation of universal theory.⁶

Let us first consider the effects of the finite temperature. If we calculate the maximum value of the two-body loss coefficient for our temperature of $T = 60 \pm 15$ nK we obtain $\beta_{max} \approx 4 \times 10^{-8} \text{cm}^3/\text{s}$, which is only about a factor of three larger than the largest value of β_{1-23} we observed in our measurements. Therefore we can expect the resonance peak to be flattened by temperature effects, which can lead to an overestimation of the inelasticity parameter η_* . To get a feeling for the magnitude of this effect one can take a look at Fig. 3.8: The value of η_* does not only determine the height of the peak on resonance but also affects the observed two-body loss far away from the resonances where $\beta \ll \beta_{max}$ for our measurements. Our fit reproduces the data across the whole magnetic field region where it is applicable, which would not be the case if a part of this data was strongly altered by temperature effects. This lead us to the conclusion that finite temperature effects can only cause a small error in our determination of η_* .

Additionally, a finite collision energy can in principle shift the position of a scattering resonance. However, the collision energy of the particles in our experiment

⁶Another explanation would be an error in the determination of the scattering lengths, however the uncertainty of the scattering lengths could only explain a deviation of the three-body parameter by about 5% [Nak10a].

is of order $h \times 1$ kHz which can only create negligible shifts in the position of the resonance. Therefore the difference in the resonance position cannot be explained by the finite temperature.

This reasoning was later confirmed by a numerical calculation by H.-W. Hammer et al. [Ham10], which found that the reduction of β by thermal effects in our measurement should be only about 25%, which is smaller than the systematic uncertainty of our data. The result of their calculation is shown in Fig. 5.9.

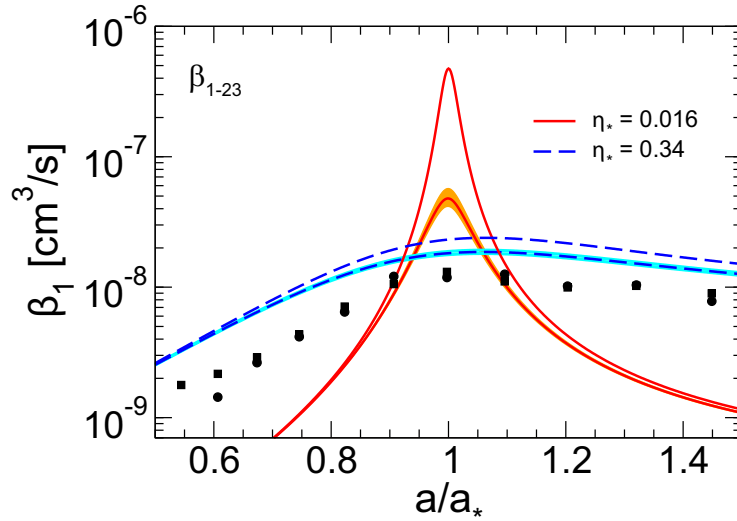


Figure 5.9: Finite-temperature calculations of β_{1-23} for two different values of η_* for a temperature of $T = 60 \pm 15$ nK. The upper curves give the zero-temperature result, while the lower curves show the finite temperature result. The shaded regions visualize the effect of the uncertainty in the temperature. The black squares show our data, while the circles are the results from [Nak10b]. Figure taken from [Ham10]

The question of finite range effects was addressed by S. Nakajima et al. who also measured β_{1-23} and found results very similar to ours [Nak10b]. They performed coupled channel calculations of the dimer binding energy which took effective range corrections into account. They found that in the vicinity of the loss resonance at 685 G the binding energy E_{23} of the $|23\rangle$ -dimer differed by about 8% from the universal prediction. This correction seemed large enough to explain the observed shift in the position of the crossing of the trimer state with the $|1\rangle$ - $|23\rangle$ atom-dimer threshold. However, when they applied the effective range corrections to the trimer state as well, its energy was shifted by a similar amount. When calculating the point where the energy of the trimer state becomes degenerate with the atom-dimer threshold, they found that the effects of these corrections cancel

each other and the position of the atom-dimer resonance is unaffected by these effective range corrections.

This seemingly surprising result can be understood by considering the structure of the Efimov trimer in this magnetic field region. In the vicinity of the atom-dimer threshold an Efimov trimer consists of a two-body cluster and a third atom which is far away from this pair (i.e. one of the hyperangles α_k is large). If the mean distance between the two-body cluster and the third atom is much larger than the size of the pair, the third atom is so loosely bound that its momentum is too low to resolve the structure of the pair. In this case one can describe the trimer as a universal dimer of a dimer and an atom. If we apply this to the ${}^6\text{Li}$ system, we see that close to the atom-dimer resonance at 685 G the Efimov trimer looks like a weakly bound dimer consisting of a $|23\rangle$ -dimer and an atom in state $|1\rangle$. In this case, the binding energy of the trimer is simply the sum of the binding energies of the $|23\rangle$ -dimer and the "dimer" formed by the $|23\rangle$ -dimer and the third atom in state $|1\rangle$. Therefore an effective range correction of the binding energy of the $|23\rangle$ -dimer shifts the energy of the trimer state by exactly the same amount as it shifts the energy of the dimer state. Consequently the energy difference between the trimer state and the atom-dimer threshold stays the same, independent of the effective range corrections. This explains why these corrections do not affect the position of the atom-dimer resonance.

As we have seen above neither temperature effects nor effective range corrections can have a significant effect on the position of the atom-dimer resonance at 685 G. For the three-body loss resonance at 895 G the scattering lengths are so much larger than r_{vdW} that effective range effects are completely negligible, and the sample used in the measurement was cold enough that temperature effects should not play a significant role [Wil09]. Consequently, the most probable explanation for the discrepancy between these measurements is that these resonances are governed by different three-body parameters. This is in direct contradiction to Efimov's scenario, which states that one three-body parameter should describe all trimer states at all magnetic fields. The reason for this is still not entirely clear, we will discuss this further in Section 5.6.

5.5.3 The $|3\rangle$ - $|12\rangle$ mixture: Ultracold Chemistry

After observing the loss resonances in the $|1\rangle$ - $|23\rangle$ atom-dimer mixture we repeated the experiments with the other two possible atom-dimer mixtures. Let us first consider the $|3\rangle$ - $|12\rangle$ -system. In this mixture we have two possible decay channels: The first is direct decay into the deep dimers. The second process are exchange reactions of the type

$$|3\rangle + |12\rangle \rightarrow |1\rangle + |23\rangle + E_{\text{kin}}, \quad (5.5)$$

which are energetically allowed for magnetic fields below 731 G where $a_{23} < a_{12}$.⁷ For most magnetic fields the kinetic energy released in the reaction is significantly larger than the trap depth and the reaction products are immediately lost from the trap. In this case the measured loss rate is the sum of the rates for exchange reactions and relaxation into deep dimers.

The results for our measurements of β_{3-12} are shown in Fig. 5.10. We observe clear minima of the relaxation rate at magnetic fields of $B \approx 610$ G and $B \approx 695$ G. Both minima appear at fields slightly above the loss resonances in the $|1\rangle$ - $|23\rangle$ mixture, so it seems likely that these features are connected.

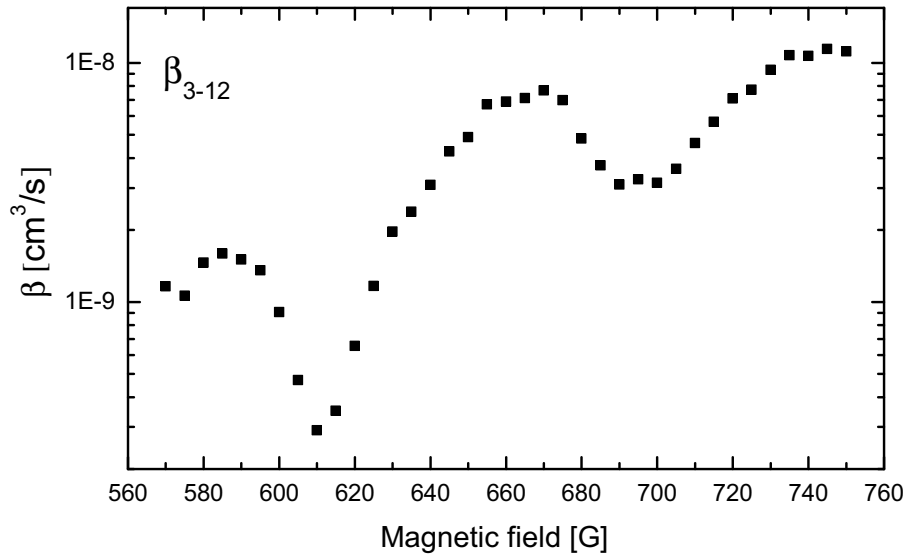


Figure 5.10: Two-body loss coefficient for the $|3\rangle$ - $|12\rangle$ atom-dimer mixture as a function of magnetic field. For fields below 730 G β_{3-12} is the sum of the decay into deep dimers and $|3\rangle + |12\rangle \rightarrow |1\rangle + |23\rangle$ exchange reactions. The rate for these exchange reactions has interference minima, which are clearly visible at $B \approx 610$ G and $B \approx 695$ G.

To understand the scattering processes in the $|3\rangle$ - $|12\rangle$ mixture it is helpful to recall the discussion of three-body scattering in Sections 3.3 and 3.5. If we look at Eq. 3.46 we see that we have already introduced the matrix elements $S_{|3,12\rangle,|3,12\rangle}$ and $S_{|1,23\rangle,|3,12\rangle}$ which describe the scattering in this atom-dimer mixture.⁸ The first matrix element describes elastic $|3\rangle$ - $|12\rangle$ atom-dimer collisions, while the second one describes exchange reactions according to Eq. 5.5. Additionally, both

⁷ Similar exchange reactions had already been observed in ultracold Cesium [Kno10].

⁸In the magnetic field region of interest the three-atom and $|2\rangle$ - $|13\rangle$ atom-dimer state are either non-existent or energetically forbidden.

matrix elements contain a loss channel into deep dimers, whose strength is given by the inelasticity parameter η_* .

Let us now consider how an incoming $|3\rangle-|12\rangle$ atom-dimer state evolves according to these matrix elements. When an asymptotic $|3\rangle-|12\rangle$ atom-dimer state enters the long-distance region it can end up in three different states: It can be directly reflected as a $|3\rangle-|12\rangle$ atom-dimer state, it can couple to the $|1\rangle-|23\rangle$ state and leave as an asymptotic $|1\rangle-|23\rangle$ atom-dimer state or it can be transmitted into the scale-invariant region and become a hyperradial wave (see Fig. 5.11). This hyperradial wave enters the short-distance region where it either decays into a deep dimer and a third atom or is reflected with a phase shift θ_* . When the reflected hyperradial wave arrives at the long distance region it can either be reflected back into the scale-invariant region or transmitted into the asymptotic region as a $|3\rangle-|12\rangle$ or $|1\rangle-|23\rangle$ atom-dimer state. These outgoing atom-dimer states have phase shifts ϕ_1 and ϕ_2 relative to the atom-dimer states which result from a direct reflection/exchange process in the long-distance region. These phase shifts can lead to destructive interference, which can cause a suppression of these processes.

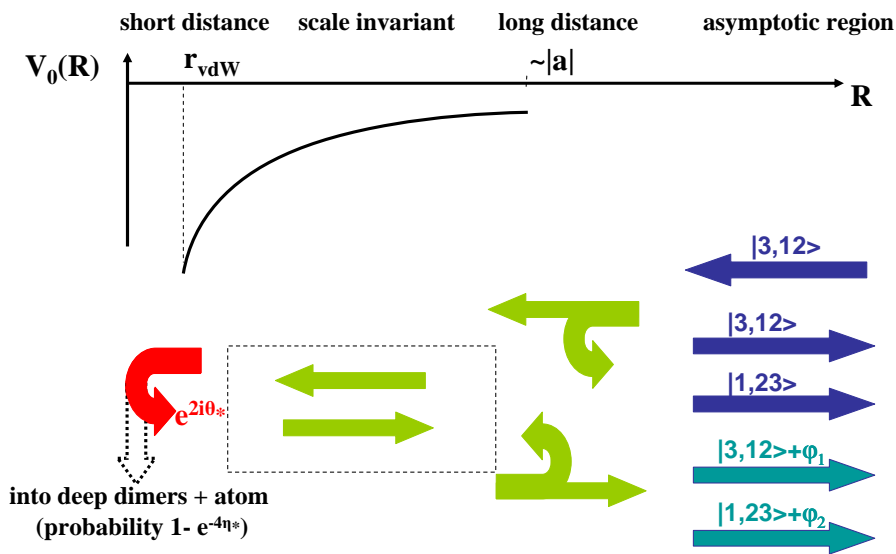


Figure 5.11: Sketch of a $|3\rangle-|12\rangle$ atom-dimer collision in the magnetic field region below 730 G. An incoming $|3\rangle-|12\rangle$ atom-dimer state can be directly reflected at the long-distance region or transmitted into the scale-invariant region as a hyperradial wave. If this hyperradial wave is transmitted back through the long-distance region the resulting atom-dimer states have a phase shift relative to the states directly reflected at the long-distance region. These phase shifts can lead to the suppression of a collision process by destructive interference.

The values of the phase shifts depend on the evolution of the wavefunction on

its way through the scale-invariant and short-distance regions. As the phase the hyperradial wave acquires during this evolution has to increase by a multiple of π for every additional Efimov state in the potential (see Sect. 3.3.1), these interference minima have to follow the same scaling as the loss resonances caused by the crossings of Efimov states. Thus the fact that the minima of β_{3-12} have similar relative positions to the maxima of β_{1-23} is indeed no coincidence.

In [D'I09], J. P. D'Incao calculated analytic formulas for the decay rates due to these processes for the special case $|a_{13}| \gg a_{12} \gg a_{23}$. He found a suppression of the rate of $|3\rangle + |12\rangle \rightarrow |1\rangle + |23\rangle$ exchange reactions whose position depends on the same three-body parameter as the loss maxima in β_{1-23} . While his results are qualitatively similar to our observation, we cannot use his formulas to fit our data as $a_{12} \approx a_{23}$ in our system.

After publication of our results two theoretical papers [Ham10, Nai10] were published which contained calculations of these rates for our system. Their results confirmed our qualitative analysis, but could not exactly reproduce our measurements.

After realizing the importance of the $|3\rangle + |12\rangle \rightarrow |1\rangle + |23\rangle$ exchange reactions we considered whether it might be possible to directly observe the reaction products. As mentioned above, this is only possible if the trap depth is much larger than the difference between the binding energies of the $|12\rangle$ - and $|23\rangle$ -dimer. As we have to use a very shallow trap, this condition is only fulfilled for magnetic fields just below 730 G, which is just the magnetic field region where the exchange reactions are suppressed by interference effects. Therefore a direct observation of the reaction products is not possible in our setup.

This could in principle be overcome by using a box-shaped trap whose volume is independent of its depth. However, creating a deep box with a flat bottom with optical potentials is an extremely challenging task, because it is hard to prevent interference effects that cause corrugations of the trapping potential. As our observation of interference minima at 610 G and 695 G already provided a clear signature for the existence of the $|3\rangle + |12\rangle \rightarrow |1\rangle + |23\rangle$ exchange reactions we decided against pursuing this project, and instead focused on our goal of direct observation of an Efimov trimer with RF-spectroscopy.

5.5.4 The $|2\rangle$ - $|13\rangle$ mixture: Suppression of two-body loss

The final measurement of atom-dimer loss we performed was to study the two-body loss rate in a $|2\rangle$ - $|13\rangle$ atom-dimer mixture for magnetic fields between 570 G and 650 G; the results are shown in Fig. 5.12. For this mixture the loss rate is given by the sum of the decay into deep dimers and $|2\rangle + |13\rangle \rightarrow |3\rangle + |12\rangle$ and $|2\rangle + |13\rangle \rightarrow |1\rangle + |23\rangle$ exchange reactions. In [D'I09] J. P. D'Incao predicted all of these processes to be suppressed with $1/a_{13}$ when approaching the $|1\rangle$ - $|3\rangle$

Feshbach resonance at 690 G.

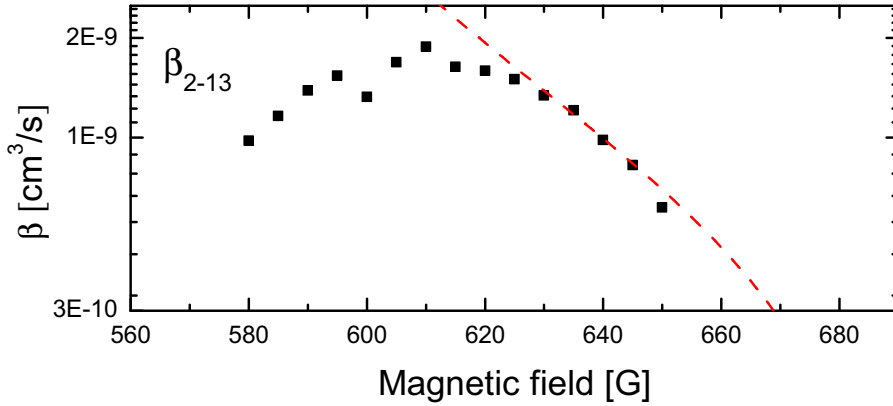


Figure 5.12: Measurement of β_{2-13} as a function of magnetic field. The red line shows a $1/a_{13}$ dependence, with the normalization adjusted to match the data points. For magnetic field above 620 G this $1/a_{13}$ dependence is in good agreement with our data.

This trend is clearly visible in our data. The measured loss rate monotonically decreases for magnetic fields above 610 G where the universal theory is applicable. For magnetic fields above 650 G, the binding energy of the $|13\rangle$ -dimer is no longer much larger than the temperature of the sample. According to Eq. 2.44 this leads to a decrease in the molecular fraction of the gas. Close to the $|1\rangle$ - $|3\rangle$ Feshbach resonance at 690 G the scattering length is so large that the sample contains only a small fraction of molecules at our temperature. Then atom-dimer collisions are no longer the dominant loss process and we cannot measure β_{2-13} .

The observed suppression of β_{2-13} is consistent with the decrease in K_3 observed for magnetic fields above 650 G (see Fig. 5.6). If $|13\rangle$ -dimers are formed in this magnetic field region they remain trapped and are relatively stable against decay in inelastic $|2\rangle$ - $|13\rangle$ collisions.

This measurement concludes our studies of inelastic collisions in a three-component Fermi gas of ${}^6\text{Li}$. We will sum up and discuss our findings in the following section.

5.6 The spectrum of Efimov states in ${}^6\text{Li}$

In the experiments described in this chapter we have found seven features in the three-atom and atom-dimer loss rates which are caused by the presence of Efimov states: Three maxima in the rate of three-body-recombination, two maxima in

the rate of inelastic atom-dimer collisions and two minima in the rate of atom-dimer exchange reactions (see Fig. 5.13). As the Efimov scenario has only two free parameters - the three-body parameter κ_* and the inelasticity parameter η_* - which can be determined from a single resonance these results should be more than enough to determine the spectrum of Efimov states in ${}^6\text{Li}$.

The first two three-body loss resonances are in the low field region at magnetic fields of 127 G and 500 G (see Fig. 5.3). They are caused by an Efimov state around a local maximum of $|a|$ at $B \sim 300$ G. The value of the three-body parameter κ_* is the same at both of these resonances, but the value of η_* differs by a factor of four. This difference in η_* can be explained by a change of the binding energy of the non-universal deep dimers with the magnetic field.

The trimer state observed in the low-field region is not expected to cross the three-atom continuum in the high-field region due to the large background scattering length, but the crossing of the second Efimov trimer was observed at a magnetic field of 895 G [Wil09]. While η_* is different again, the value of κ_* extracted from this resonance agrees with the value from the low-field region.

With this agreement between resonances at 127 G, 500 G and 895 G it was a big surprise when the three-body parameter extracted from our atom-dimer measurements showed a significant difference to the values obtained by studying three-body recombination. While the applicability of universal theory might be questionable for the resonance at 600 G where $a_{23} \approx r_0$, the shift of the resonance at 685 G (where universal theory should be applicable) cannot be explained by temperature effects or effective range corrections.

One possible explanation for this could be that a magnetic field dependence of the short-range three-body physics causes a change of κ_* with the magnetic field. However, this would mean that κ_* is roughly constant from 127 G to 500 G, changes to a different value at 685 G and then changes back to its low-field value at 895 G. Especially the return of κ_* to the low-field value at 895 G in this scenario looks like a rather unlikely coincidence.

The alternative is that the three-body parameter is independent of the magnetic field and something is still missing from our understanding of Efimov physics in ultracold gases. To check whether this is the case it is useful to consider the results from experiments on other atomic species. The only system besides ${}^6\text{Li}$ where the positions of three-body loss resonances have been compared over a wide magnetic field range is ${}^{133}\text{Cs}$, where the Innsbruck group observed maxima in the three-body recombination in the vicinity of Feshbach resonances at 500 G and 800 G [Ber11]. These loss resonances are described by the same three-body parameter as the first Efimov resonance measured at a magnetic field of 7.5 G in [Kra06]. This is in excellent agreement with our observation of identical three-body parameters for all three-atom resonances in ${}^6\text{Li}$.

${}^{133}\text{Cs}$ is also the only other system besides ${}^6\text{Li}$ where atom-dimer loss rates have

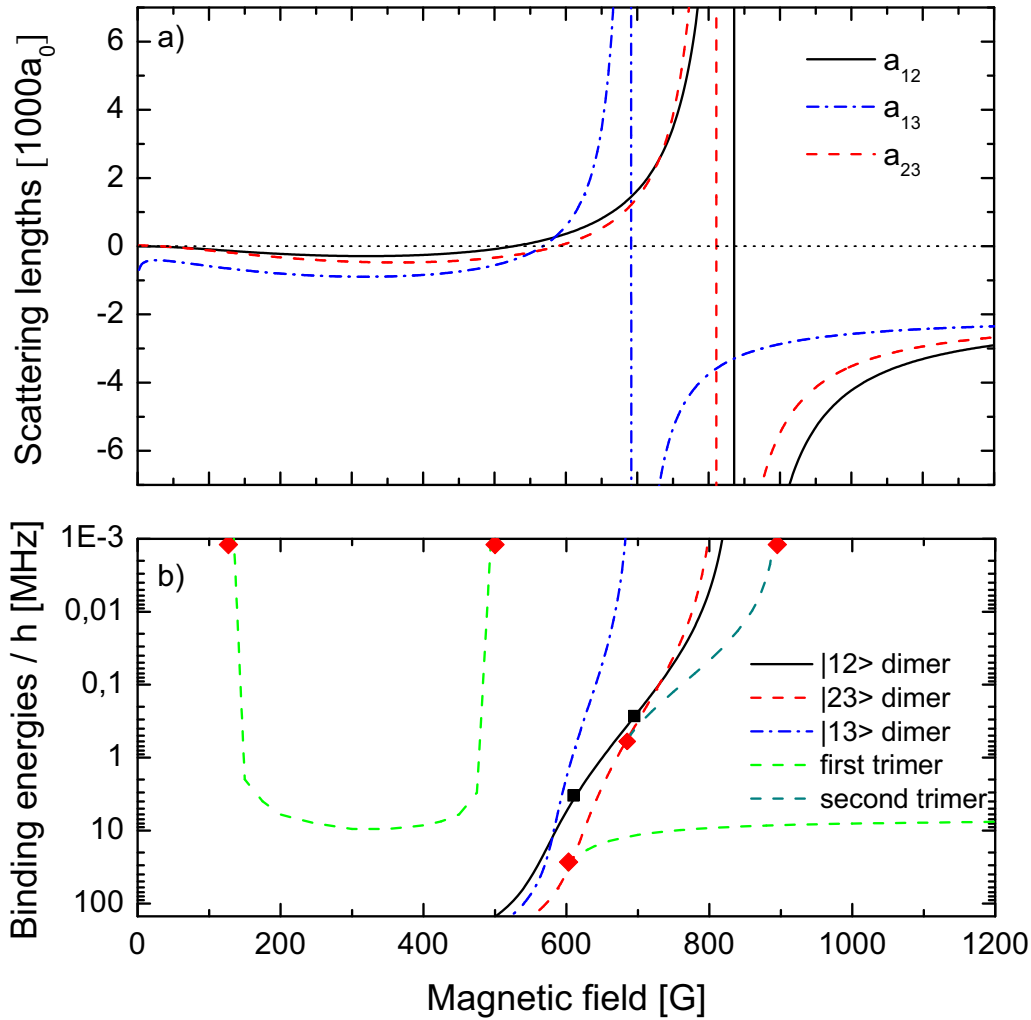


Figure 5.13: The spectrum of Efimov states in ${}^6\text{Li}$. The red diamonds mark the experimental observations of the intersections of the trimer states with the three-atom and atom-dimer continua, while the black squares show the positions of the interference minima in the $|3\rangle + |12\rangle \rightarrow |1\rangle + |23\rangle$ exchange reactions. The binding energies of the dimer and trimer states in the high-field region were calculated by P. Naidon including non-universal corrections and an energy-dependent three-body parameter. On the scale used in the graph the differences to the universal model shown in Fig. 5.4 are hardly visible.

been measured directly. In ^{133}Cs the three-body parameters extracted from three-atom and atom-dimer experiments do not agree either, but the difference is larger and goes in the opposite direction than in ^6Li [Kra06, Kno09]. However, it is not clear whether the ^6Li and ^{133}Cs atom-dimer experiments can be directly compared, as the three-atom and atom-dimer resonance measured in the ^{133}Cs experiments lie on opposite sides of a zero-crossing of a and also belong to different trimer states in the series. Therefore we are eagerly awaiting results on atom-dimer scattering at the ^{133}Cs high-field Feshbach resonances which we could directly compare to the shift of the atom-dimer resonances we observed in ^6Li .

While our studies of the few-body physics of three-component ^6Li show a very good qualitative agreement with the Efimov scenario, there are some quantitative differences which suggest that few-body physics beyond the Efimov effect might be important. A deeper understanding of the mechanisms altering the Efimov scenario in ultracold gases is certainly desirable, and our RF-experiments described in chapter 6 might prove to be an important step toward this goal. However, to obtain a description of the few-body physics of the ^6Li system which can serve as a basis for many-body experiments the results which were presented in this chapter are certainly sufficient. The easiest way to achieve this is to use universal theory with a varying three-body parameter extracted from the experiments. As the changes in κ_* are relatively small (about 30%) this interpolation should give quite reasonable results.

This approach was first taken by P. Naidon et al. [Nai10, Nak10b]. He used a model with an energy-dependent three-body parameter, which he extracted from the experimental data by fitting the evolution of the three-body parameter for the different loss resonances. Whether such an energy-dependence of κ_* is a physical reality is still an open question, but his model gives a decent description of the collision physics over the entire high-field region. His results for the binding energy of the trimer and its crossing with the dimer states (including effective-range corrections) are shown in Fig. 5.13.

The consequences of the results presented in this chapter for our planned studies of many-body physics of three-component Fermi gases will be discussed in chapter 7.

Chapter 6

RF-Association of Efimov Trimers

As soon as we had identified the maxima of three-body recombination in the we found in our first experiments as crossings of an Efimov state, we wondered whether one could use RF-spectroscopy to directly study the properties of the trimers. This technique had already been used extensively to study universal dimer states, so it seemed natural to apply it to trimer states as well. However, there are a number of differences between trimers and dimers which make RF-spectroscopy of trimers much more difficult. This chapter describes how we managed to overcome these challenges and performed the first spectroscopy of Efimov trimers.

We start with a brief introduction of the concept of RF-spectroscopy and describe some experimental techniques using a two-component Fermi gas as an example. This is followed by a discussion of the challenges we had to overcome before we could observe signatures of Efimov states in our RF-spectra. We then discuss how we used this technique to map out the binding energy of an Efimov state as a function of the magnetic field. The last section describes how RF-association can be used to address the questions about the behavior of the three-body parameter that were raised by the atom-dimer measurements discussed in chapter 5.

6.1 RF-spectroscopy in a two-component system

The concept of flipping the spin of an atom with an oscillating magnetic field has already been introduced in the context of the preparation of three-component samples in Section 5.1. Here we will discuss how this can be used for spectroscopy of universal dimer states.

The energy splittings between different hyperfine levels of an alkali atom – which depend on the strength of the magnetic offset field – can be calculated to very high precision using the Breit-Rabi formula. The frequency required to flip the spin of a free atom can therefore be used to calibrate the magnetic offset field in our ex-

periment. As the transitions between the different hyperfine levels of the ground state are electric dipole forbidden, they have extremely narrow natural linewidths. The minimum width of the transitions achievable in our experiment is therefore determined by the stability of the magnetic offset field. A great advantage of ${}^6\text{Li}$ is that in the high-field regime the transitions only tune weakly with the magnetic field (about 1 kHz/G for the $|1\rangle$ - $|2\rangle$ and 10 kHz/G for the $|2\rangle$ - $|3\rangle$ transition). Therefore a magnetic field stability of ~ 50 mG already allows to perform spectroscopic measurements with sub-kHz precision.

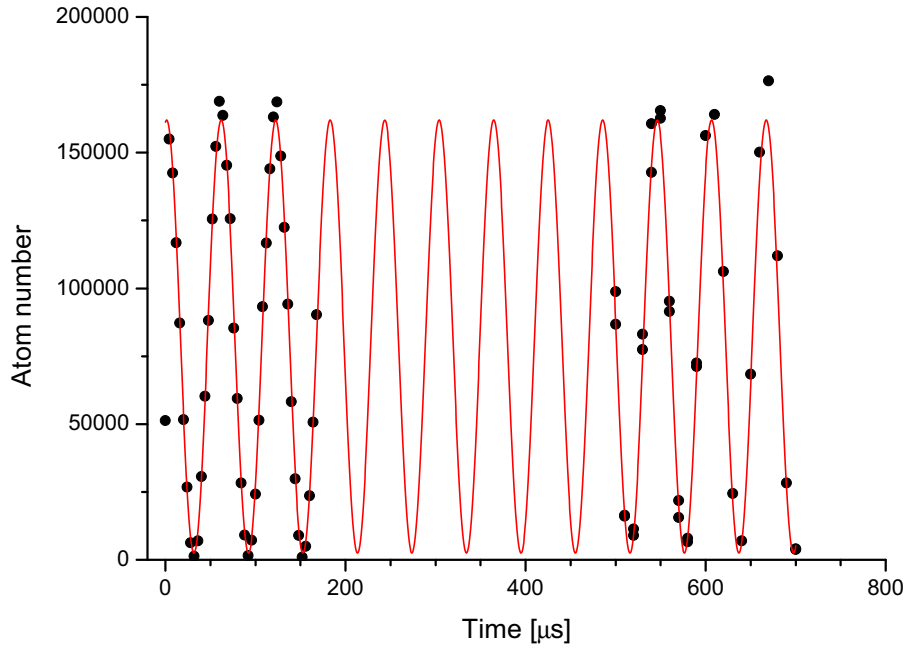


Figure 6.1: Rabi oscillations in an ideal Fermi gas. The population of state $|2\rangle$ is shown as a function of the duration of the RF-pulse. On the observed timescale the oscillations show no signs of damping.

The simplest spectroscopic measurement we can perform in our system is to take an ideal Fermi gas of atoms in state $|1\rangle$ and create a coupling between states $|1\rangle$ and $|2\rangle$ by applying an RF-field on the $|1\rangle$ - $|2\rangle$ transition. As the states form a two-level system, this leads to Rabi oscillations between states $|1\rangle$ and $|2\rangle$ as shown in Fig. 6.1. The Rabi frequency Ω depends on the strength of the oscillating magnetic field \mathbf{B} according to

$$\Omega \propto \mu \mathbf{B} \cdot \mathbf{S}, \quad (6.1)$$

where μ is the magnetic moment of the spin \mathbf{S} we want to flip. As we are trying to flip a nuclear spin one would expect μ to be on the order of the nuclear magnetic moment $\mu_N \approx 1/1836 \times \mu_B$. However, as nuclear and electronic spin are not

completely decoupled in our system the resulting spin still contains a small fraction ($\sim 1\%$) of the electron spin. This fraction increases the magnetic moment to about $\mu \approx 1/100 \times \mu_B$; it can therefore be viewed as a "lever" which we can use to flip the nuclear spin of the atom.¹

The Rabi oscillations shown in Fig. 6.1 are a purely single-particle effect. As each particle is exposed to the same RF-field all particles are in the same superposition state at any time. Therefore the system stays a one-component Fermi gas of identical particles until the Rabi oscillations of the individual particles dephase, for example through different trajectories in an inhomogeneous magnetic field.

Let us now move on to the more interesting case of a two-component mixture. We begin by considering a gas of atoms in states $|1\rangle$ and $|2\rangle$, where we apply an RF-field on the $|2\rangle$ - $|3\rangle$ transition (see Fig. 6.2). If there are finite scattering lengths between the particles the resulting collisions will lead to a much quicker decoherence of the Rabi oscillations. As soon as three non-identical atoms - i.e. one atom in state $|1\rangle$ and two atoms in different superpositions of states $|2\rangle$ and $|3\rangle$ - come together, they can be lost in a three-body recombination event. For small scattering length these three-body events are suppressed and after a sufficiently long pulse the system contains an equal number of atoms in states $|2\rangle$ and $|3\rangle$, which can be used to prepare three-component samples (see Sect. 5.1). However, if the scattering lengths are large the particles in the third state are quickly lost from the trap.

To measure the transition frequency between two states it is useful to use a weak RF-pulse which is longer than the decoherence time of the system. In this case the Rabi oscillations are damped out and the RF-spectra show a loss feature which is centered at the transition frequency (see upper panel of Fig. 6.3).²

If we do not start from a gas of free atoms in states $|1\rangle$ and $|2\rangle$ but a gas of $|12\rangle$ -dimers, creating a free atom in state $|3\rangle$ requires breaking the dimer. Therefore the frequency of the $|2\rangle$ - $|3\rangle$ transition is blue-shifted by the binding energy E_{12} of the $|12\rangle$ -dimer (see Fig. 6.2 and 6.3). If there is a $|13\rangle$ dimer state in the system, one can also drive a bound-bound transition from the $|12\rangle$ -dimer to the $|13\rangle$ -dimer; the frequency of this transition is shifted by the difference of the two dimer binding energies.

RF-Spectra showing the process of dimer dissociation are shown in Fig. 6.3.

¹The fraction of the electron spin is larger for the $|2\rangle$ - $|3\rangle$ transition, which is therefore easier to drive than the $|1\rangle$ - $|2\rangle$ transition.

²Depending on the properties of the RF-pulse, the width of this loss feature can be determined by the Rabi frequency, the Fourier limit of the RF pulse or the stability of the magnetic offset field.

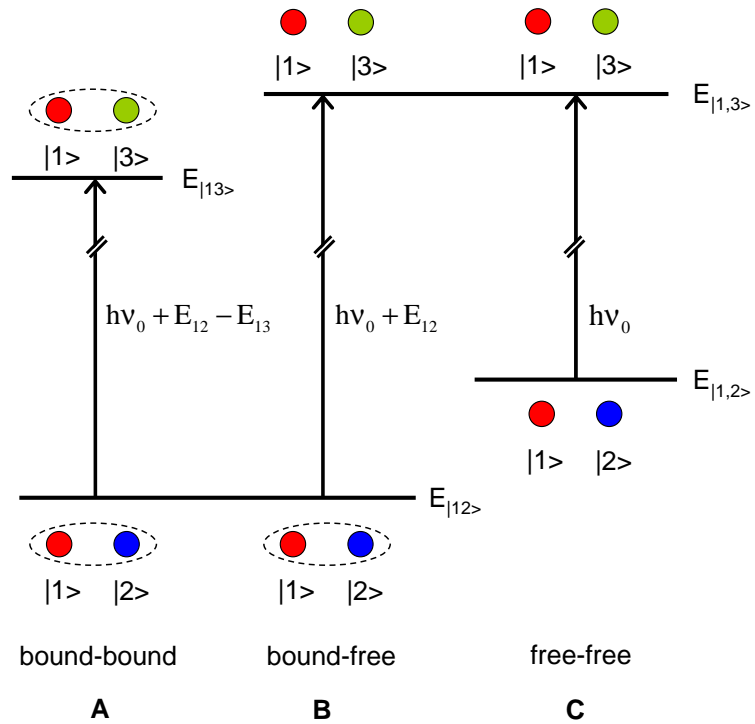


Figure 6.2: Sketch of the different RF-transitions starting from a $|1\rangle$ - $|2\rangle$ mixture. The bound-bound transition from a $|12\rangle$ - to a $|13\rangle$ -dimer (A) is shifted from the free-free transition (C) by the difference between the dimer binding energies E_{12} and E_{13} . For the dissociation of a dimer into two free atoms (B) the transition is blue-shifted by the binding energy of the $|12\rangle$ -dimer.

6.2 Finding an initial system for trimer spectroscopy

The key reason why RF-spectroscopy is more difficult for trimers than for dimers is the short lifetime of the trimer state. To perform spectroscopy of universal dimers one can simply prepare a sample of dimers using one of the methods described in Sect. 2.7 and measure their binding energy as shown in Fig. 6.2 and 6.3.

In contrast, Efimov trimers quickly decay into a deeply bound dimer and a free atom. In ${}^6\text{Li}$ the timescales for this decay have been predicted to be about 500 ns for the first and about $100\ \mu\text{s}$ for the second trimer state [Bra10]. This fast decay has so far prevented the preparation of macroscopic samples of Efimov trimers.³ Therefore dissociation spectroscopy of Efimov trimers is currently not an option.

³In Section 6.5 we will discuss the possibility of creating such macroscopic samples with RF-association techniques.

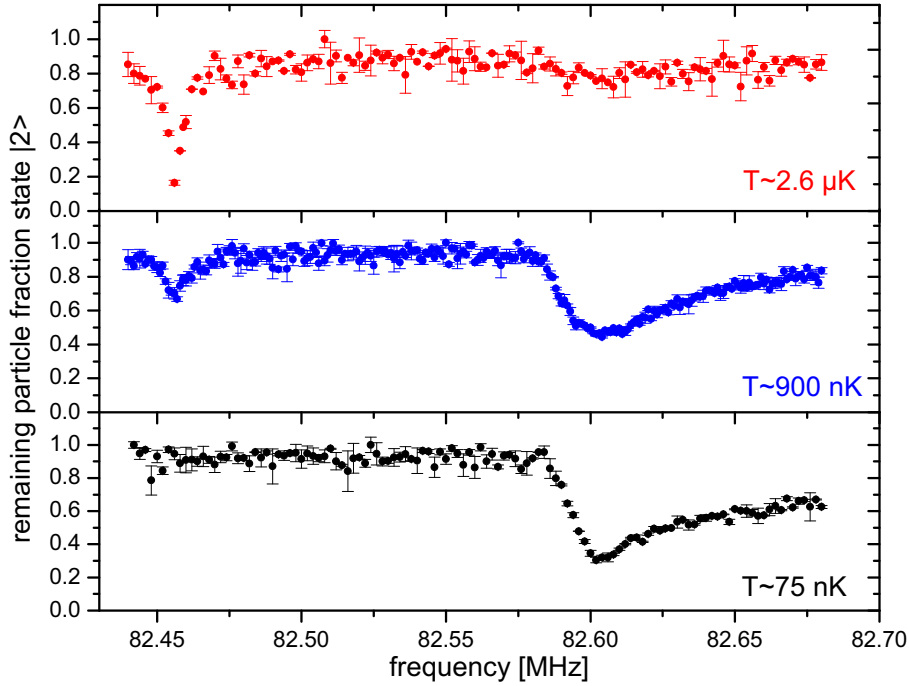


Figure 6.3: RF-spectra of a $|1\rangle$ - $|2\rangle$ mixture at different temperatures showing the free-free and bound-free transitions at a magnetic field of 720 G. The spectra show the fraction of atoms remaining in state $|2\rangle$ after the RF-pulse as a function of frequency. For high temperatures (upper panel) there are no molecules in the sample, and only the free-free transition is observable. In the middle panel $k_b T \approx E_B$ and the sample consists of both molecules and atoms. In the bottom panel $k_b T \ll E_B$ and only the dissociation of molecules is visible in the RF-spectrum. This measurement is a nice illustration of the chemical equilibrium between atoms and dimers discussed in Section 2.7.2

The alternative to this approach is to use the inverse process of RF-association, where two or more particles are associated into a bound state with the help of an RF-photon. An example for this would be the association of $|13\rangle$ -dimers from a gas of atoms in states $|1\rangle$ and $|2\rangle$, which can be easily done by shining in an RF-field red-detuned from the $|23\rangle$ -transition by the binding energy of the $|13\rangle$ -dimer.

To extend this to the association of a trimer consisting of atoms in states $|1\rangle$, $|2\rangle$ and $|3\rangle$ from three free atoms one would like to start with two atoms e.g. in states $|1\rangle$ and $|2\rangle$ and a third atom in a fourth state $|x\rangle$, where the atom in state $|x\rangle$ only interacts weakly with the other atoms. To associate the trimer one would then drive this atom from state $|x\rangle$ to state $|3\rangle$ with a detuning corresponding to the trimer binding energy. However, there is no suitable fourth state in the ${}^6\text{Li}$

system: Only the three states of the lower hyperfine manifold are stable against dipolar relaxation (see Sect. 2.6). Therefore we cannot use atoms in any states other than $|1\rangle$, $|2\rangle$ and $|3\rangle$.

Let us now consider whether we can find an initial system suitable for RF-association under this restriction. One option would be to start from an $|1\rangle$ - $|2\rangle$ - $|3\rangle$ mixture and modulate the magnetic offset field. This causes a time-dependent variation of the scattering lengths, which can create a coupling to a bound state in the vicinity of the continuum. If two atoms approach each other to a distance comparable to the size of the bound state, this coupling can lead to the formation of a dimer.

While this "magnetic field wiggling" technique has been used to associate universal dimers [Tho05, Gro10], it is not suitable for studying Efimov trimers. The difference is that the trimer has a finite lifetime, which causes a finite width of the trimer state. If three atoms come close together, they can therefore couple to the trimer state and decay into a deeply bound dimer and a free atom without needing an RF-photon to carry away the binding energy of the trimer. Consequently, it seems unlikely that it will be possible to create an observable enhancement of the loss rate in the three-component gas with this technique.

Another possible initial system would be an imbalanced two-component Fermi gas. An example for this would be to start with a $|1\rangle$ - $|2\rangle$ - $|2\rangle$ mixture and drive an RF-transition to the third state. However, as we have seen in Sect. 6.1 driving the atoms from state $|2\rangle$ to state $|3\rangle$ is a coherent process, so all atoms initially in state $|2\rangle$ will remain identical particles. Therefore this cannot lead to the association of Efimov trimers.

However, it is possible to overcome this problem by starting with a $|1\rangle$ - $|2\rangle$ - $|2\rangle$ or $|2\rangle$ - $|2\rangle$ - $|3\rangle$ system and binding half of the majority atoms into $|12\rangle$ - or $|23\rangle$ -dimers. In this case, the transition frequency of the atoms bound in dimers is shifted by the binding energy of the dimer and we can selectively address the free atoms in state $|2\rangle$. This approach will be discussed in the next section.

6.3 Challenges for trimer association

The first step to associate a trimer from an atom and a dimer is to prepare either a $|2\rangle$ - $|12\rangle$ or $|2\rangle$ - $|23\rangle$ atom-dimer mixture. This can be easily done using the methods we developed for our atom-dimer collision experiments described in chapter 5. The next step is to apply an RF-field which is detuned from the $|23\rangle$ - or $|12\rangle$ -transition by the difference of the dimer and trimer binding energies, as shown in Fig. 6.6 and Fig. 6.7. However, this RF-field can only lead to the association of a trimer if the wavefunction of the atom-dimer system has a finite overlap with the wavefunction of the trimer state. Let us first consider a trimer which is close to the atom-dimer threshold. In this case the trimer looks like a weakly bound pair of an

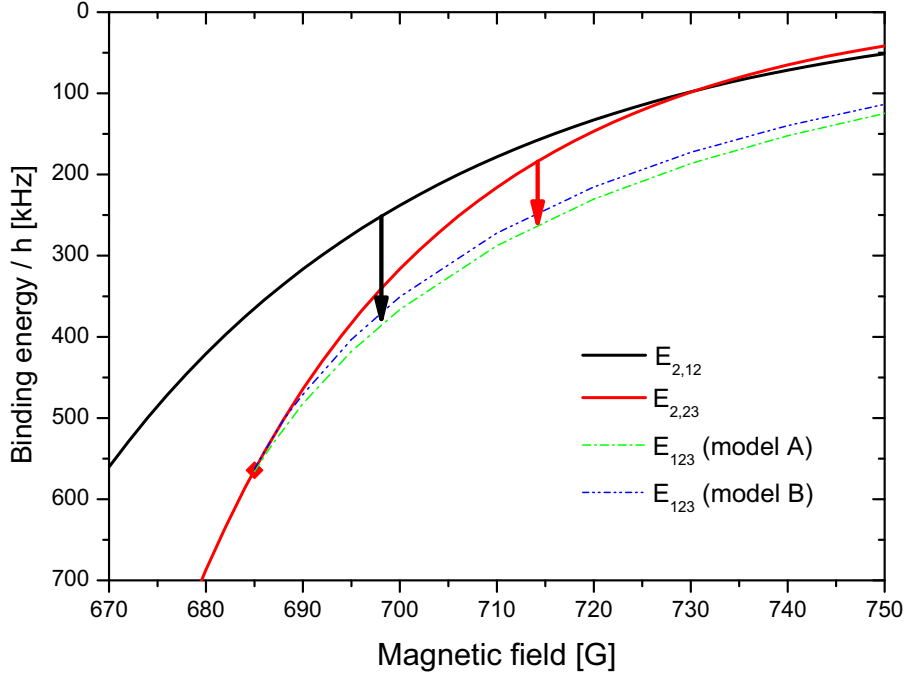


Figure 6.4: Scheme for trimer association from an atom-dimer mixture, the difference in $E_{2,12}$ $E_{2,23}$ due to the hyperfine energy of the atoms was neglected in this figure. Starting from a $|2\rangle$ - $|12\rangle$ or $|2\rangle$ - $|23\rangle$ mixture, one can associate trimers by driving the free atom to the third state. The frequency for this association process is detuned from the bare transition $|2\rangle$ - $|12\rangle$ or $|2\rangle$ - $|23\rangle$ by the difference of the dimer and trimer binding energies.

atom in state $|1\rangle$ and a $|23\rangle$ -dimer (see Sect. 5.5.3). Therefore the wavefunction of a $|2\rangle$ - $|23\rangle$ atom-dimer system should have a decent overlap with the trimer state if the atom approaches the dimer to a distance on the order of a_{1-23} .

To achieve high association rates one has to maximize the probability of finding an atom and a dimer close together, which is done by increasing the phase space densities of atoms and dimers. However, if the gas becomes quantum degenerate it spatially separates into a molecular BEC in the center of the trap which is surrounded by a shell of unpaired fermionic atoms (see Sect. 2.8.2) and the overlap between atoms and dimers is lost. Therefore we have to use thermal atom-dimer mixtures with $T/T_F \gtrsim 1$, which is one of the main limitations for the achievable association rate.

6.3.1 Maximizing the Rabi frequency

Another challenge for the RF-association of trimers is the short lifetime of the trimer state. To get a feeling for the effect of this finite lifetime let us assume that we have an atom-dimer state $|2, 23\rangle$ which we couple to a trimer state $|123\rangle$ using an RF-field. In a simple picture we can view this as a two-level system with a coupling Ω_{tr} . If both states are stable, the system will simply perform Rabi oscillations between the atom-dimer and trimer state. However, if the excited state $|123\rangle$ has a finite lifetime τ its population decays with a rate $\gamma = 1/\tau$.

To understand how this decay rate affects the system we take a look at the population of the excited state as a function of time. We assume that for $t < 0$ there is no coupling and the system is completely in the ground state. When the coupling is switched on at $t = 0$ the population of the excited state is (in the absence of decay) given by

$$P_{|123\rangle} = \sin^2\left(\frac{\Omega_{tr}t}{2}\right). \quad (6.2)$$

For a finite lifetime of the excited state the decay serves as a continuous measurement of the population of the excited state. If $\Omega_{tr} \ll \gamma$ we only have to consider the evolution of $P_{|123\rangle}$ on short timescales, for which we can make the approximation

$$P_{|123\rangle} \approx \frac{\Omega_{tr}^2 t^2}{4}. \quad (6.3)$$

In this case the the population of the excited state is proportional to Ω_{tr}^2/γ^2 . This suppression is analogous to the quantum-Zeno effect [Mis77], which has been observed in multiple experiments [Ita90, Str06].

For the trimer states in ${}^6\text{Li}$ the predicted decay rates in the vicinity of their intersections with the atom-dimer continuum are ~ 2 MHz for the first and ~ 10 kHz for the second trimer [Bra10]. Due to its lower decay rate the second trimer state is a much better candidate for RF-association than the first one.

While we do not know the exact value of the coupling strength Ω_{tr} in our RF-association experiments, it cannot be larger than the Rabi frequency of the bare atomic transition.

As described in Sect. 6.1 the Rabi frequency for flipping the nuclear spin of an atom depends on the magnetic moment μ of the spin and the strength of the oscillating magnetic field. As μ is fixed by nature, increasing the Rabi frequency is only possible by increasing the strength of the magnetic field. To create this field we use a single loop of copper wire (diameter ~ 1 mm) through which a current is driven by a 100 W RF-amplifier (ZHL-100W-52, Mini-Circuits).⁴ To match the

⁴While we sometimes use the term "antenna" for our RF-coil, the distance between the atoms and the loop is much smaller than the wavelength of the RF-signals. Therefore we want to maximize the amount of current running through our RF-coil, while at the same time trying to minimize

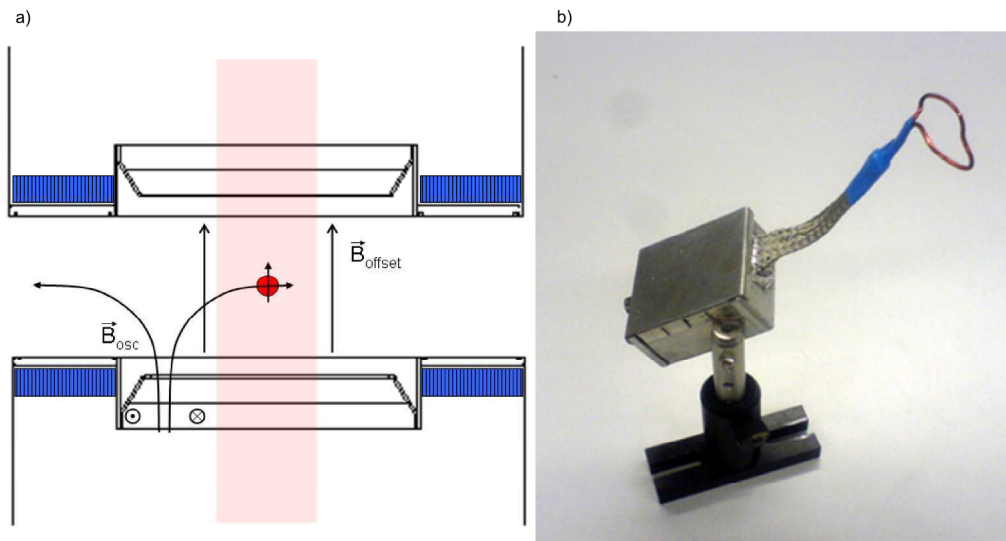


Figure 6.5: (a) Sketch showing the placement of the RF-coil at the reentrant view-port. The position of the atoms is marked by the red circle, the Feshbach coils creating the homogenous offset field are shown in blue. The extension of the vertical MOT beam is shown in red. (b) Image of the RF-antenna. The shielded box contains the impedance matching circuit.

output impedance of the amplifier (50Ω) to the much smaller impedance of the RF-coil and make the antenna resonant at the frequencies of about 80 MHz of the $|12\rangle$ - and $|23\rangle$ -transitions we use a matching circuit consisting of two ceramic capacitors. The details to this matching circuit can be found in [Wen09a]. With this RF-setup, which we used in our first experiments, we achieved Rabi frequencies of $\Omega \approx 2\pi \times 600 \text{ Hz}$ [Wen09a, Ott10], which is much less than the decay rates of the trimer state. Therefore we needed to improve the RF-setup by at least a factor of ten to have a realistic chance of observing the trimer state. We therefore designed a new RF-setup which is described below.

The conceptually simplest approach would have been to increase the current in the RF-coil by a factor of ten. However, this would have meant an increase in RF-power by a factor of one hundred to about 10 kW, which would have posed significant technical challenges.⁵ As our impedance matching circuits already reached efficiencies of $\sim 30\%$, improving the matching could also not create the required Rabi frequencies.

The only aspect of the RF-coil that could still be optimized was its position relative

the amount of RF-power that is sent out as electromagnetic waves.

⁵Even with only 100 W of RF-power parts of our antenna reach temperatures above 100°C during long pulses.

to the atoms. As the strength of a magnetic dipole drops off with $1/r^3$, this can have a large effect on the Rabi frequency. The point where we can get closest to the atoms is at the reentrant viewport on the bottom of the octagon.⁶ To flip the spin of the atoms, the oscillating magnetic field has to act perpendicular to the homogeneous offset field which defines the quantization axis. Therefore we built an RF-coil which is positioned close to the viewport and whose center is displaced from the center of the viewport. This maximizes the component of the RF-field perpendicular to the offset field at the position of the atoms, as shown in Fig. 6.5. At the full RF-power of 100 W we achieve Rabi frequencies of $\Omega_{12} \approx 2\pi \times 16$ kHz and $\Omega_{23} \approx 2\pi \times 7$ kHz with this antenna. The Rabi frequency is slightly higher for the $|12\rangle$ -transition, as the impedance matching was optimized for this transition frequency (~ 76 MHz) and the resonance of the matching circuit has a relatively narrow width (see [Wen09a]).

One particular challenge of the RF-association experiments was that we had to apply a huge amount of RF-power in close proximity to high-precision analog electronics. Applying a high-power RF-pulse can create large fluctuations of the ground in the entire lab, which can for example disrupt the frequency stabilization of the imaging lasers or the intensity stabilization of the dipole trap. To minimize these effects we added a grounded shielding to the matching circuit of the RF-antenna and built a grounded copper enclosure around the lower part of the octagon. This allowed us to reduce the cross-talk between the RF-setup and the rest of the lab by about a factor of ten.

While this was sufficient for the lasers, the stabilization of the current in the Feshbach coils was still affected by the RF-pulses. To eliminate this problem we deactivated the digital PID-loop stabilizing the Feshbach current shortly before the RF-pulse and set the experimental control to give out a constant value. This value was the average of the output values set in the last millisecond before the RF-pulse was applied. This led to a slight drift of the current of at most 1 G over 50 ms as the resistance of the Feshbach coils changes as the coils heat up. However, as the RF-transitions we used in our measurements only tune weakly with the magnetic field (see Sect. 6.1) this has only a small effect on our measurements.

6.4 Trimer Association from an atom-dimer mixture

As stated in Sect. 6.2 we can do RF-association of Efimov trimers in two different ways: We can either start from a $|2\rangle$ - $|23\rangle$ mixture and drive the free atoms from state $|2\rangle$ to state $|1\rangle$, or we can start from a $|2\rangle$ - $|12\rangle$ mixture and drive the free atoms to state $|3\rangle$. Close to the $|1\rangle$ - $|23\rangle$ atom-dimer threshold the Efimov

⁶At the top viewport the access is blocked by the high-resolution imaging setup.

trimer looks like a weakly bound pair of a state $|1\rangle$ atom and a $|23\rangle$ -dimer (see Sect. 5.5.2). Consequently one can expect the wavefunction of the trimer to have a good overlap with a pair of a state $|2\rangle$ atom and a $|23\rangle$ -dimer in this region. Therefore we performed our first attempts at trimer association with a $|2\rangle$ - $|23\rangle$ mixture.

The first step of the experiments was to prepare a thermal ($T/T_F \approx 1$) $|2\rangle$ - $|23\rangle$ mixture at magnetic fields between 660 G and 740 G. To achieve a higher density – and therefore a better signal to noise ratio during absorption imaging – the trap was not expanded as it was done for the collision experiments described in sections 5.4 and 5.5. Then we applied RF-pulses with frequencies around the $|12\rangle$ -transition and recorded the number of atoms remaining in state $|2\rangle$.⁷

As an atom and a dimer have to come close to each other (i.e. collide) to form a trimer and the wavefunction overlap between the atom-dimer and trimer states is limited, the association process is strongly suppressed. Therefore we need a lot of RF-photons to create an observable association signal, which requires long and intense RF-pulses. This completely saturates the peaks resulting from the bare atomic transition and dimer dissociation, which makes it harder to observe the dip caused by trimer association.⁸

The first signatures we observed are shown in Fig. 6.8. For $B \geq 685$ G there is a clear deformation of the RF-spectra on the blue-detuned side of the free-free transition. However, this observation did not match the predicted position of the atom-dimer resonance at 672 G. Additionally, the strong saturation made it impossible to extract quantitative information from those spectra. We attempted to improve the visibility of the features by reducing the saturation or changing the degeneracy of the sample, but had only very moderate success (see Fig. 6.10). Therefore we decided to try to resolve the discrepancy of our measurements to the predicted position of the trimer state by fixing the position of the intersection of the trimer state with the $|1\rangle$ - $|23\rangle$ atom-dimer threshold using collision experiments (see Sect. 5.5.2.). As soon as these measurements were completed we resumed our work on the RF-association.

As stated above the RF-association measures the difference between the dimer and trimer binding energies. For the $|2\rangle$ - $|23\rangle$ mixture this difference goes to zero as the trimer approaches the atom-dimer threshold at 685 G. Therefore the trimer feature gets lost in the broadened free-free transition. For the $|2\rangle$ - $|12\rangle$ mixture the situation is completely different: E_{12} is always significantly smaller than E_{123}

⁷If the dimers are weakly bound, the atoms bound in dimers are also detected by the absorption imaging, albeit with slightly reduced efficiency.

⁸When we first applied such long and intense RF-pulses, we used a direct digital synthesizer (DDS) whose sidebands were suppressed by only 30 dB-40 dB as an RF-source, which caused distortions of the RF-spectra. We solved this problem by switching to a different RF-source (Agilent E4432B, Agilent Technologies) with a sideband suppression of about 80 dB.

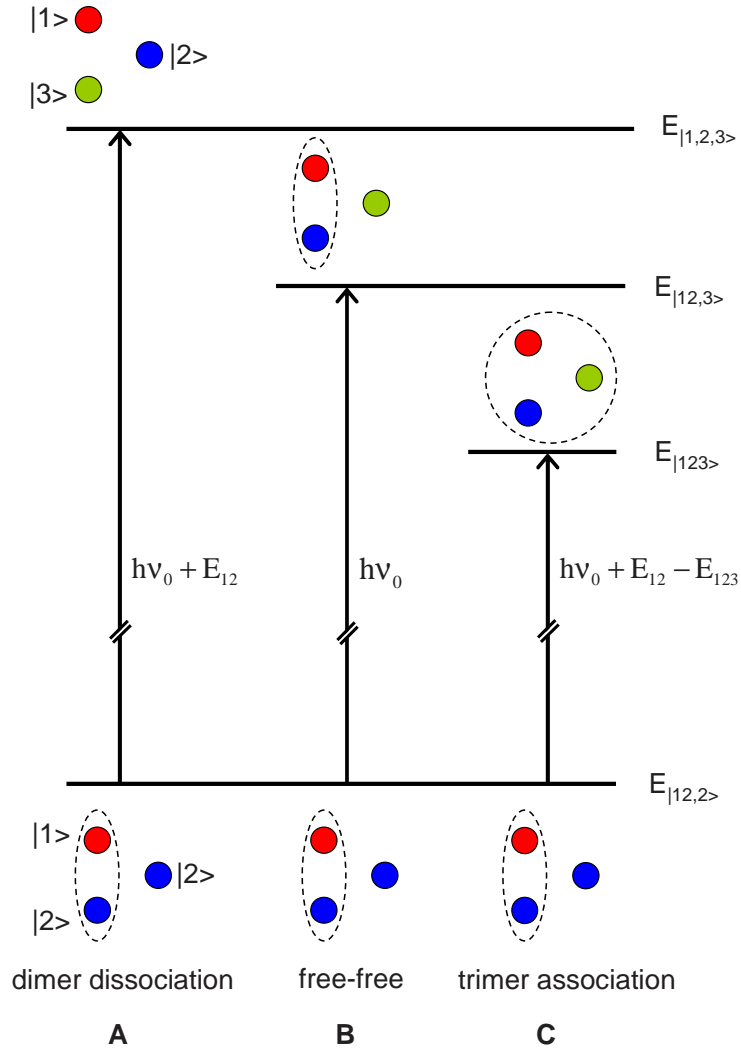


Figure 6.6: Relevant transitions and energy levels for the RF-association of trimers from a $|2\rangle$ - $|12\rangle$ mixture. The initial system has the energy $E_{|12,2\rangle}$ of a free atom in state $|2\rangle$ and a $|12\rangle$ dimer. The frequency ν_0 of the bare transition drives the unbound atoms from state $|2\rangle$ to state $|3\rangle$, leading to a $|3\rangle$ - $|12\rangle$ atom-dimer mixture (B). By using a frequency blue-detuned from the bare atomic transition by the dimer binding energy we can dissociate the dimer, leading to three unbound atoms in states $|1\rangle$, $|2\rangle$ and $|3\rangle$ (A). To associate a dimer and an atom into a trimer the frequency has to be red-detuned by the difference of the dimer and trimer binding energies (C).

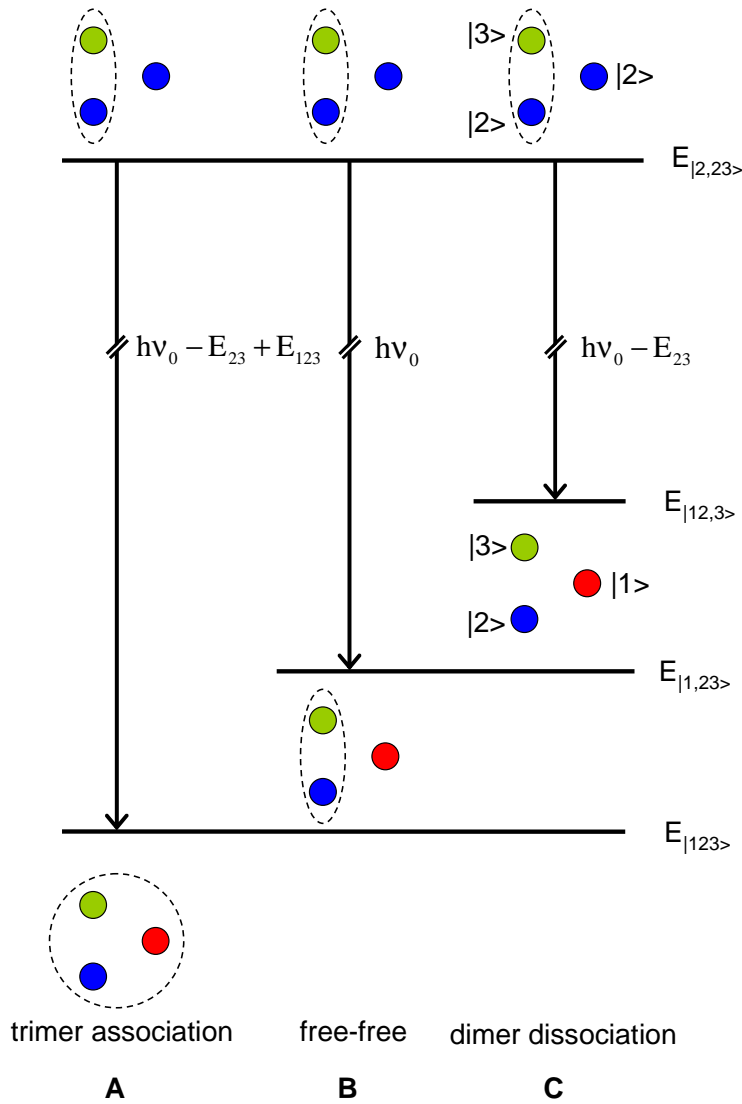


Figure 6.7: Scheme of the RF-association starting from a $|2\rangle$ - $|23\rangle$ mixture. As we drive the free atoms from state $|2\rangle$ to state $|1\rangle$ the energy of the final states is lower than the energy of the initial system. This inverts the order of the features compared to the $|2\rangle$ - $|12\rangle$ mixture. Therefore the trimer association (A) is blue-detuned from the bare transition (B), while the dimer dissociation is red-detuned (C).

(see Fig. 6.4). Therefore the trimer association peak is always offset from the bare $|1\rangle$ - $|2\rangle$ transition by at least the difference $E_{23} - E_{12}$ of the binding energies of the $|12\rangle$ - and $|23\rangle$ -dimer. Consequently the free-free and trimer association peaks should be separated much better for the $|2\rangle$ - $|12\rangle$ mixture. A sketch of the transitions for this mixture is shown in Fig. 6.6. For this mixture the order of the association peaks is reversed compared to the $|2\rangle$ - $|23\rangle$ mixture; the association peak is therefore red-detuned from the free-free transition.

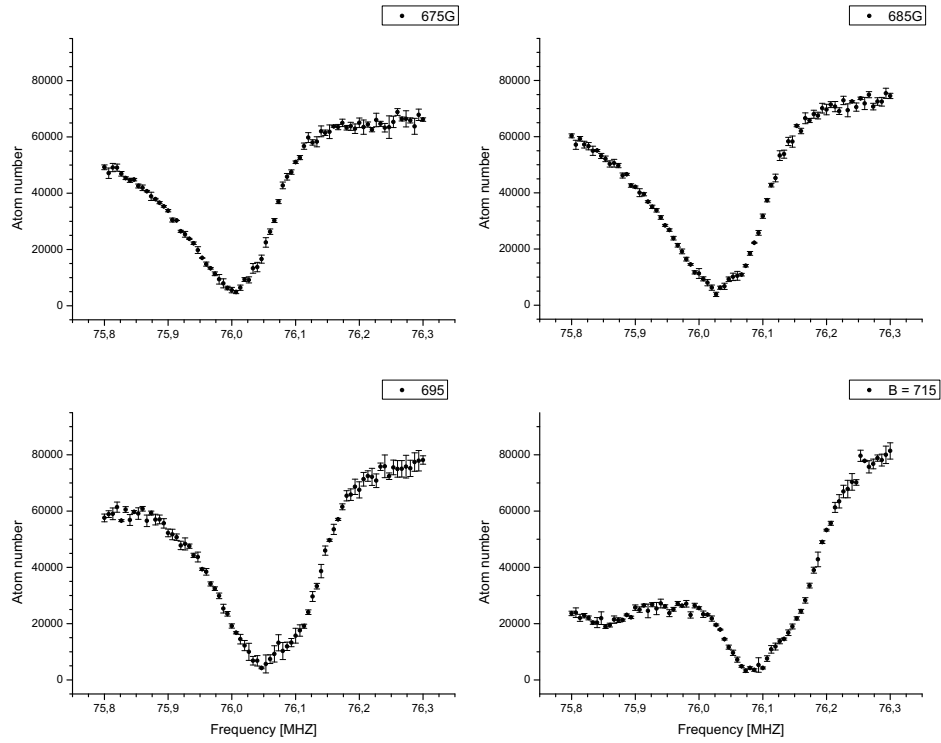


Figure 6.8: First signatures of trimer association observed after applying RF-pulses with a Rabi frequency of $(2\pi \times 16)$ kHz and a duration of 50 ms to a $|2\rangle$ - $|23\rangle$ atom-dimer mixture. The plots show the number of atoms remaining in state $|2\rangle$ after the RF-pulse as a function of frequency for different magnetic fields. The central feature is the saturated free-free transition, the broad feature red-detuned from is central peak visible for $B = 715$ G is caused by dimer dissociation. For magnetic fields $B \geq 685$ G the trimer association is visible as a deformation of the blue-detuned (right) side of the central dip. Each data point is the average of four independent measurements, the error bars show the standard error of the mean.

To measure the trimer association starting from this initial system we prepared a thermal $|2\rangle$ - $|12\rangle$ atom-dimer mixture containing about 8.5×10^4 atoms and

7.5×10^4 dimers in a trap with trapping frequencies of $(\omega_x, \omega_y, \omega_z) \approx 2\pi \times (820, 820, 75)$ Hz. The temperature of the sample was about $1 \mu\text{K}$, corresponding to $T/T_F \approx 1$. Sample spectra for this mixture are shown in Fig. 6.9.

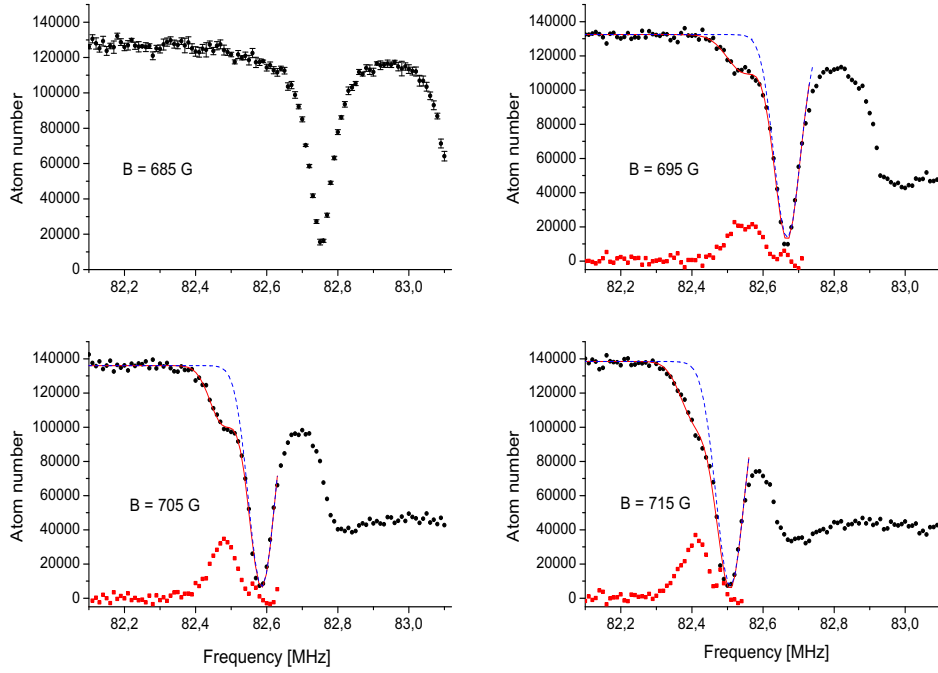


Figure 6.9: RF-spectra for RF-association from a $|2\rangle$ - $|12\rangle$ mixture. The central dip results from driving the bare atomic transition and the dip to the right is a consequence of the dissociation of dimers. The trimer association manifests itself as a smaller feature sitting on the left flank of the central dip. The red lines are fits of two overlapping Gaussians to the data. The dashed blue lines show the Gaussians fitted to the central dip. The difference between these fits and the data, which shows the signal from the trimer association, is plotted as red squares. Each data point is the average of five to eight individual measurements, to improve clarity error bars are only shown for the dataset at 685 G.

For magnetic fields larger than 685 G the trimer association feature is clearly visible as a kink on the left shoulder of the dip caused by the free-free transition. As the features are better separated we one attempt to fit the spectra.

As we do not have a better model for the broadened lineshapes of the saturated transitions, we fitted the data with two Gaussians to obtain the positions of the

association feature.⁹ As a fit function we used the sum of two Gaussians

$$N(\nu) = N_0 - A_0 e^{-\frac{(\nu-\nu_0)^2}{w_0^2}} - A_1 e^{-\frac{(\nu-\nu_1)^2}{w_1^2}}; \quad (6.4)$$

the free parameters of the fit are the position, width and amplitude of the free-free (ν_0, w_0, A_0) and trimer association (ν_1, w_1, A_1) peaks and the initial particle number N_0 . To fit the data we performed a least-squares fit using the Matlab curve fitting tool. For this fit we had to exclude data points which are affected by the dimer dissociation feature. Unfortunately, the position of this cutoff can affect the width fitted to the central peak, which can alter the fit result for the position of the association feature. To estimate the possible systematic shift that is introduced by the cutoff we varied its position within the range that could be considered reasonable. From the changes in the fit parameters we estimated the systematic shift to be $\lesssim 10$ kHz.

The results of the fits are shown as red lines in Fig. 6.9. To better visualize the part of the signal caused by trimer association the difference between the data and the Gaussian fitted to the free-free peak is plotted as red squares.

From the difference between the peak positions we can calculate the trimer binding energy for each magnetic field value according to

$$E_{123} = E_{12} + h(\nu_0 - \nu_1). \quad (6.5)$$

For magnetic fields $B \geq 705$ G the energy difference between the $|23\rangle$ -dimer and the trimer is large enough that we can apply this fitting procedure as well, although we have to fix the position of the free-free transition to the value calculated from the magnetic field to achieve a stable fit (see Fig. 6.10).

The results of our fits to the RF-spectra are shown in Fig. 6.11. The black circles show the data obtained when starting from a $|2\rangle$ - $|12\rangle$ mixture. The red data points were taken using a $|2\rangle$ - $|23\rangle$ mixture as initial system. The measurements from the different initial systems show remarkably good agreement. For both datasets the error bars give the 2σ confidence bounds of the fits to the spectra, however the naive model for the lineshapes can cause additional systematic errors. We estimate these to be a fraction of the width $w_1 \approx 50$ kHz of the association features. In addition to these uncertainties there can be an additional shift of the association features caused by the finite kinetic energy of the particles. Each of the two

⁹As both the trimer and the dimer state are universal objects whose properties are known from universal theory, the wavefunction overlap of a pair of an atom and a dimer with the trimer state should be determined by universal theory as well. As the binding energies of the involved bound states are much lower than the energy involved in the spin flip, they should have only negligible effects on the coupling between the different spin states induced by the RF-field. Therefore it should in principle be possible to calculate the lineshape of the association features using universal theory. However, this goes beyond our abilities as experimental physicists.

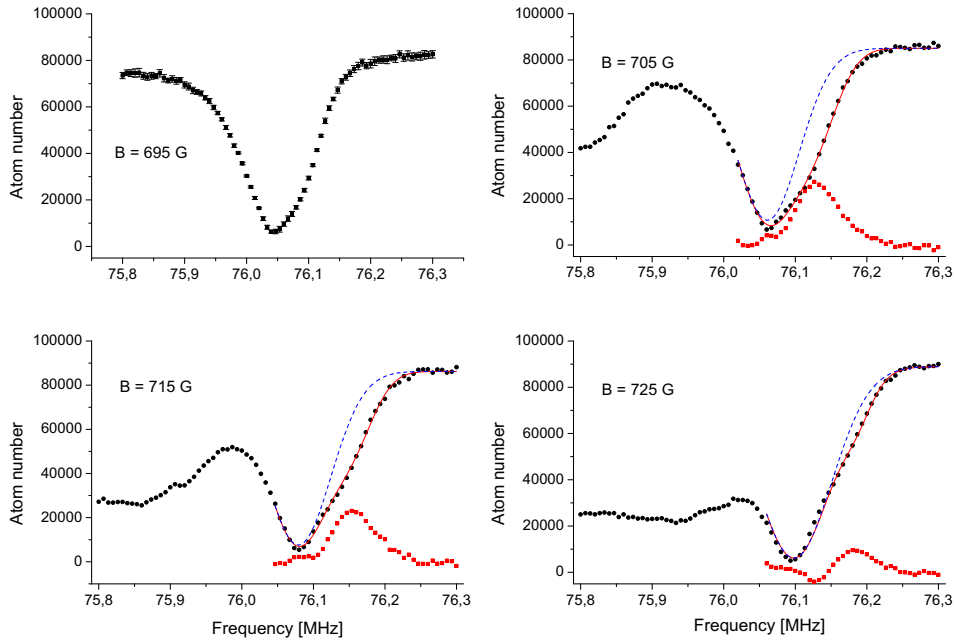


Figure 6.10: Spectra of trimer association from a mixture of atoms in state $|2\rangle$ and $|23\rangle$ dimers. The red lines are fits of two overlapping Gaussians to the data. The fit to the central dip is shown as a blue line, the difference between this fit and the data is shown as red squares. As the free atoms are driven to state $|1\rangle$ the features for dimer dissociation appear at lower frequency than the bare transition, while the trimer association appears higher frequency (see Fig. 6.7). Due to the smaller separation between the bare transition and the trimer association the visibility of the association dip is not as good as for the $|2\rangle$ - $|12\rangle$ mixture. For magnetic fields below 705 G the association feature is too close to the bare transition to accurately determine its position. Each data point is the average of eight to nine individual measurements

particles involved in the association process carries a kinetic energy of $3/2k_B T$. As the motion of the center of mass of the two particles does not affect the association process, the shift of the feature can be expected to be on the order of $\frac{3}{2}k_B T/h \approx 30$ kHz. This effect can be reduced by using colder samples, which was done in a recent work by S. Nakajima et al. [Nak10a].

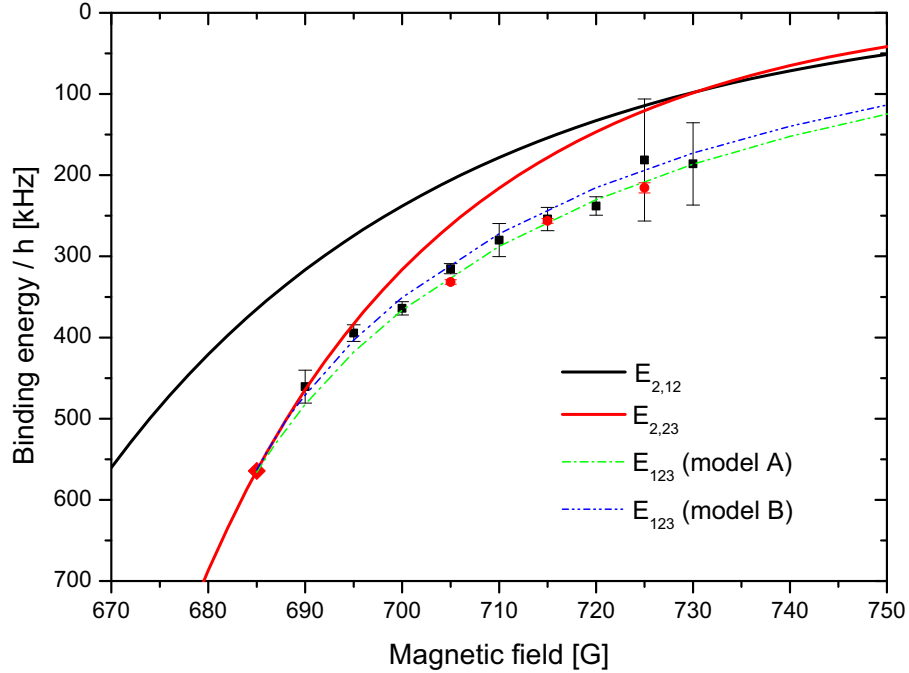


Figure 6.11: Measured binding energy of the second Efimov trimer in ${}^6\text{Li}$ measured using a $|2\rangle\text{-}|12\rangle$ (black squares) or $|2\rangle\text{-}|23\rangle$ (red dots) mixture as the initial system. The error bars are derived from the 2σ confidence bounds of the fits to the RF-spectra. The solid lines give the energies of the initial $|2\rangle\text{-}|12\rangle$ and $|2\rangle\text{-}|23\rangle$ mixtures including non-universal corrections to the dimer binding energies [Nak10b]. The red diamond marks the position of the observed intersection of the trimer state with the $|1\rangle\text{-}|23\rangle$ atom-dimer threshold (see Section 5.6). The dashed lines show the binding energy of the trimer according to calculations from [Nak10b].

When examining the data shown in Fig. 6.11 one sees that the measured trimer binding energy increases for smaller magnetic fields (and therefore smaller scattering lengths), as it is expected from Efimov's scenario. At the same time the difference between the energy of the trimer and the $|23\rangle$ -dimer decreases. At a magnetic field of 690 G both energies are the same within our experimental resolution and for $B \leq 685$ G the association signal vanishes. This coincides with the position of the atom-dimer resonance of 685 ± 2 G and therefore confirms

the previous interpretation of such loss resonances as signatures of a trimer state becoming degenerate with the continuum.

We can also compare our data to the calculations of the trimer binding energies shown in Fig. 5.13, which use the positions of the observed loss resonances as input parameters (dashed lines in Fig. 6.11). The two curves show the results of two models which use different energy-dependent parametrizations of the scattering length to describe the effective-range corrections to the dimer and trimer binding energies [Nai10, Nak10b]. These models also contain an energy-dependence of the three-body parameter to describe the variation of the three-body parameter observed in the high-field region (see sect. 5.6). Within their systematic uncertainties, our measurements of the trimer binding energy are in good agreement with these calculations. However, the resolution of our measurements is currently insufficient to distinguish between these models and a calculation with a constant three-body parameter derived from the atom-dimer resonance at 685 G.

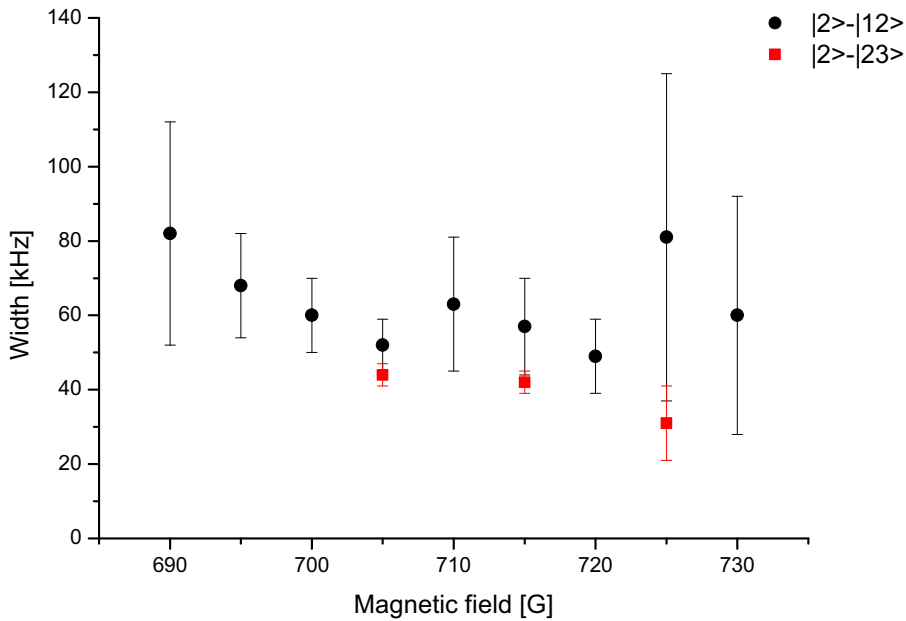


Figure 6.12: Width of the Gaussians fitted to the association features shown in Fig. 6.9 and 6.10 using Eq. 6.4. Within the statistical and systematic errors the data is consistent with a constant width of about 60 kHz.

Another interesting aspect of the RF-spectra is the width of the association features. In principle, the linewidth of a transition and the lifetime of the excited state are connected by

$$\tau = \frac{1}{\Gamma} = \frac{1}{2\pi\gamma}, \quad (6.6)$$

where Γ is the decay rate and $\gamma = \Gamma/2\pi$ is the natural linewidth of the transition. However, for our association experiments we have to expect a significant increase in the observed width of the association features due to systematic effects. One factor which is certain to play a role is the kinetic energy of the particles, which is on the order of $\frac{3}{2}k_B T/h \approx 30$ kHz. Additionally, the vicinity of the association features to the strongly saturated free-free transition can further affect the lineshape in a way that is not described by our naive fitting function. Applying Eq. 6.6 to our data can therefore only give a lower bound for the lifetime of the trimer state.

Fig. 6.12 shows the results obtained for the widths of the association peaks when fitting the spectra according to Eq. 6.4. In addition to the statistical uncertainties of the fit shown by the error bars, there can be systematic errors caused by the naive fitting function for the overlapping peaks. While there might be a slight decrease of the fitted width for higher magnetic fields, the data is consistent with a constant width of $w \approx 60$ kHz of the association features. This corresponds to a lower bound of $\tau > 2 \mu\text{s}$, which is much less than the lifetime of the trimer state of about $140 \mu\text{s}$ derived from the three-atom resonance at 895 G. This was calculated using a small η approximation where the trimer lifetime is proportional to η_* [Bra10]. However, the value of the inelasticity parameter $\eta_* \approx 0.34$ found for the atom-dimer resonance at 685 G is about a factor of twenty larger than the value at the three-atom resonance at 895 G. While the validity of this approximation is questionable at this value of η_* , we can still use it to get a rough guess of the trimer lifetime in the region where we perform our association measurements. The resulting value of $\tau \approx 7 \mu\text{s}$ is somewhat larger than the lower bound we extract from our spectra, which can be explained by the broadening of the association features by systematic effects.

Finally, we can also consider the amplitude of the Gaussians fitted to the association features. As one can see from Fig. 6.13 the amplitude of the features shows a much stronger variation with the magnetic field strength than their width. Let us first look at the results for the $|2\rangle$ - $|12\rangle$ mixture. While for magnetic fields above 710 G the amplitude of the association features is roughly constant, there is a strong decrease in the association signal as one approaches the atom-dimer crossing at 685 G. For the $|2\rangle$ - $|23\rangle$ mixture we observe the opposite: The association signal gets stronger for smaller magnetic fields.

We believe that this behavior can be explained by the changing structure of the Efimov trimers: As stated before, the Efimov trimer looks similar to a weakly bound pair of a state $|1\rangle$ atom and a $|23\rangle$ -dimer close to the atom-dimer threshold. Therefore the wavefunction overlap for driving a pair of a state $|2\rangle$ atom and a $|23\rangle$ -dimer to the trimer state is higher in the vicinity of the resonance, while the association from a $|2\rangle$ - $|12\rangle$ mixture is suppressed in this magnetic field region. This becomes quite apparent when comparing the measurements with the

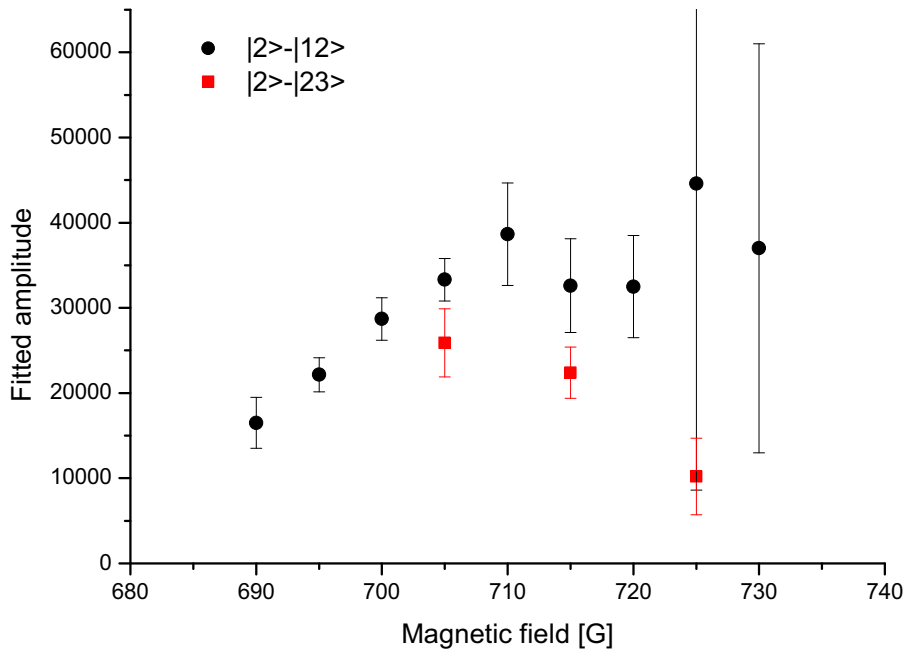


Figure 6.13: Amplitude of the Gaussians fitted to the association features shown in Fig. 6.9 and Fig. 6.10. The error bars give the 2σ confidence bounds of the fit. The large errors for the $|2\rangle$ - $|12\rangle$ mixture for magnetic fields above 720 G are caused by the decreasing separation of the free-free and trimer association peaks for higher fields, which makes the fit less stable. For the $|2\rangle$ - $|12\rangle$ mixture the amplitude decreases when approaching the atom-dimer resonance at 685 G, while it increases for the $|2\rangle$ - $|23\rangle$ mixture. We attribute this behavior to the asymmetry of the Efimov trimer close to the atom-dimer threshold.

two different mixtures for the magnetic field of $B = 685$ G where the trimer becomes unbound: For the $|2\rangle$ - $|12\rangle$ mixture (see Fig. 6.9) the association feature has completely vanished at this point, whereas the trimer clearly affects the $|2\rangle$ - $|23\rangle$ mixture shown in Fig. 6.8. Farther away from the atom-dimer threshold the asymmetry between the atoms in the different states is much smaller. This explains why the efficiency of RF-association from the $|2\rangle$ - $|12\rangle$ system seems to grow for larger magnetic fields, while association from the $|2\rangle$ - $|23\rangle$ system becomes more difficult.

This concludes our analysis of the spectra from our RF-association measurements. In the next section we will sum up our findings and discuss possible improvements of our RF-association technique.

6.5 RF-association of Efimov trimers: Achievements and prospects

With our RF-association experiments we have performed the first direct observation of an Efimov state. This technique allows to measure the binding energy of an Efimov state as a function of the magnetic field, in contrast to previous experiments which could only detect Efimov states by studying the rate constants for inelastic collisions [Lom10b]. With our measurements we could show that the collisional resonances in the atom-dimer scattering described in Sect. 5.5.2 are indeed at the points where the binding energy of an Efimov trimer becomes degenerate with the atom-dimer threshold. This confirms the interpretation of such scattering resonances as signatures for the intersections of Efimov states with the continuum.

One of the great advantages of RF-association spectroscopy is that the binding energy measurements can be used to directly study the behavior of the Efimov states far away from the continuum. If one assumes a constant three-body parameter this can be used to test the predictions Efimov's radial law makes for the trimer binding energy (see Sect. 3.3.1). On the other hand, assuming that the universal theory – maybe with the inclusion of some effective range corrections – accurately describes the system, one can use RF-association spectroscopy to map out the value of the three-body parameter as a function of the magnetic field.

This has been done by S. Nakajima et al. in a recent experiment. They found a non-monotonous variation of the three-body parameter, which is not yet understood [Nak10a].

One other application of our RF-association technique besides precision studies of Efimov states could be the preparation of macroscopic samples of universal trimers. This would require a Rabi frequency much higher than the decay rate of the trimer, such that the trimer state can be populated in a coherent fashion. By performing a π -pulse or a rapid adiabatic passage one could then coherently transfer a part of an atom-dimer sample into the trimer state. The fraction of the sample converted into trimers would depend on the wavefunction overlap of the initial system with a gas of trimers, which is currently unknown. If the fraction is large enough to create a few thousand trimers with a single RF-pulse, we should be able to image the created trimers with resonant light, just like it is done with universal dimers. By varying the time between the creation of the trimers and the imaging pulse we should then be able to directly measure the lifetime of the Efimov trimers.

Due to the short lifetime of the Efimov trimers this scheme would require a Rabi frequency of $\Omega \gtrsim 1$ MHz, which we cannot achieve with our current setup. However, we are setting up a new experiment dedicated to studying three-component

Fermi gases, where the RF-antenna is much closer to the atoms and such high Rabi frequencies should be achievable. We will discuss this new setup – together with our plans to study many-body physics of three-component Fermi gases – in the next chapter.

Chapter 7

From few- to many-body physics

In this chapter we will discuss the consequences of our results for future studies of three-component Fermi gases. First we will consider the possibility of utilizing the techniques for preparation and manipulation of three-component Fermi gases developed during this thesis for the study of many-body physics. Next we will discuss how the stability of the system can be enhanced by the presence of an optical lattice. Finally we will introduce the new experimental apparatus we are currently setting up, which will be dedicated to studying three-component Fermi gases, and give a brief outlook on the experiments we want to perform with this new machine.

7.1 Studying the many-body physics of a three-component Fermi gas

To study interesting many-body physics at the temperatures which can currently be achieved in ultracold Fermi gases the system has to be strongly interacting ($k_F a > 1$) (see Sect. 2.8.2). For two-component gases of ${}^6\text{Li}$ this strongly interacting regime can easily be reached in the vicinity of the Feshbach resonances in the high-field region, but for three-component gases this is much more challenging. The main difficulty is that for large enough scattering lengths (for ${}^6\text{Li}$ this is $a \gtrsim 300 a_0$) the many-body ground state is an ideal gas of Efimov trimers (see Fig. 2.9). However, such a system is extremely unstable due to the short lifetime of the Efimov trimers and – as the trimers are identical fermions which cannot interact at ultracold temperatures – does not offer interesting many-body physics. To observe exciting many-body effects such as color superfluidity one therefore has to work in a metastable regime. We will first examine how one could obtain a three-component gas in the strongly interacting regime, followed by a discussion of the measurements that could be performed with such a system.

Our established technique for creating three-component Fermi gases is to start with a two-component gas and populate the third state with an RF-transfer at a magnetic field of 563 G where all scattering lengths are small (see sect 5.1). The two-component gas which serves as the initial system has to be prepared by evaporative cooling at a magnetic field of 300 G, which limits the achievable degeneracy to $T/T_F \approx 0.2$ (see sect. 4.6). The subsequent RF-transfer of one third of the population to the third state creates holes in the Fermi distribution, which effectively heats up the gas. Therefore the highest degeneracy we have been able to reach in a three-component gas prepared in this fashion is $T/T_F \approx 0.35$. This is not sufficient to reach e.g. superfluid phases of the three-component system. Additionally, when taking such a gas and ramping to a Feshbach resonance we would move up on the repulsive branch of the resonance as shown in Fig. 2.4. Therefore the system would need to relax into the ground state via evaporative cooling. However, due to the high loss rates in this region the sample will decay before this ground state is reached. For these reasons this is not a viable method for preparing deeply degenerate three-component gases.

The alternative to this approach is to directly prepare the sample in the high-field region. This has the advantage that it is possible to start from a deeply degenerate ($T/T_F \lesssim 0.1$) two-component Fermi gas, which can be easily created by evaporative cooling in the vicinity of a Feshbach resonance (see Sect. 4.6). However, the preparation of the three-component sample is made much more difficult by the high decay rates.

One approach is to prepare the sample in the magnetic field region above 834 G where all scattering lengths are negative, similar to the preparation of the three-component gas from free atoms in the low-field region. As in the preparation scheme described in Section 5.1, the superpositions created by the RF-pulse have to decohere before one obtains a three-component sample (see Sect. 5.1). However, the inelastic decay is much stronger in the high-field region and the atoms are lost in inelastic collisions during this decoherence process.

A much more promising approach is to start from a deeply degenerate atom-dimer mixture and use a scheme similar to the one described in Section 5.5.1. This degenerate atom-dimer mixture spatially separates into a molecular BEC in the center of the trap and an outer shell of unpaired fermions. These free atoms can be easily transferred to the third state with an RF-pulse. If we perform this transfer at a magnetic field where the mean field energies of the initial and final state are similar, the system should still be close to equilibrium after the transfer. This gives us a viable strategy to prepare deeply degenerate three-component gases in thermal equilibrium.

The next important question is whether we can use this system to study many-body physics. To answer this let us first consider the techniques which have been used to study the many-body physics of two-component gases. The most prominent

methods are the observation of collective oscillations [Bar04a, Kin04, Nas09], probing the properties of fermion pairs in the unitary and BCS-regime with RF-spectroscopy [Chi04a, Sch08c, Ste08, Sch09] and in-situ observation of density profiles [Par06, Zwi06c, Nas10, Hor10]. To measure the frequency of collective oscillations it is necessary to follow the evolution of the shape of the cloud for a long time. Therefore this method requires a long-lived system, which is not fulfilled for a three-component Fermi gas. In contrast, RF-spectroscopy and in-situ observation can be used to extract information about the system on much shorter timescales.

When using these techniques to probe a many-body system it is advantageous to work with a gas which is in equilibrium. For example, to study phase separation of color superfluids in a trap as predicted in [Paa07] it would be necessary to prepare equilibrated three-component samples at a number of different interaction strengths. Reaching such equilibrated states requires a certain amount of elastic collisions. Therefore the key factor that determines whether this is a viable approach is the ratio between elastic and inelastic collisions in the system. Just as the inelastic collisions the elastic scattering in a three-component Fermi system is affected by the presence of the Efimov trimers. Consequently, the results we obtained studying inelastic collisions can be used to calculate the cross sections for the atom-dimer scattering in a three-component mixture of ${}^6\text{Li}$. The results for the $|1\rangle$ - $|23\rangle$ mixture are plotted in Fig. 7.1.

For a three-component gas at magnetic fields above 834 G where all scattering lengths are negative there are no dimer states in the system. For a thermal gas the atoms are lost in three-body collisions in this magnetic field region. In this case it is possible to tune the ratio of elastic to inelastic collisions by varying the density of the sample, as the rate of two-body collisions – which are responsible for thermalization – scales with n^2 while the loss rate scales with n^3 . However, for a deeply degenerate Fermi gas with large negative scattering lengths the loss is not necessarily dominated by three-body collisions, as the particles will form pairs which can be lost in two-body collisions. This has been observed for two-component Fermi gases [Du09, Zür09] but has not been studied for three-component systems. Therefore we cannot give a number for the ratio of elastic to inelastic collisions in this region, but we expect it to be similar to the value calculated for the atom-dimer system.

From Fig. 7.1 one can see that for magnetic fields above 720 G the rate of elastic collisions is about a factor of ten higher than the rate of inelastic loss. Compared to the ratio of about 10^5 that can be reached in a two-component Fermi gas of ${}^6\text{Li}$ (see Sect. 2.7.1) this value is very small. However, ${}^6\text{Li}$ is an exceptional case, many-body physics can also be studied in two-component Fermi gases of ${}^{40}\text{K}$ where this ratio is much smaller.

To make a more quantitative statement about the feasibility of studying many-

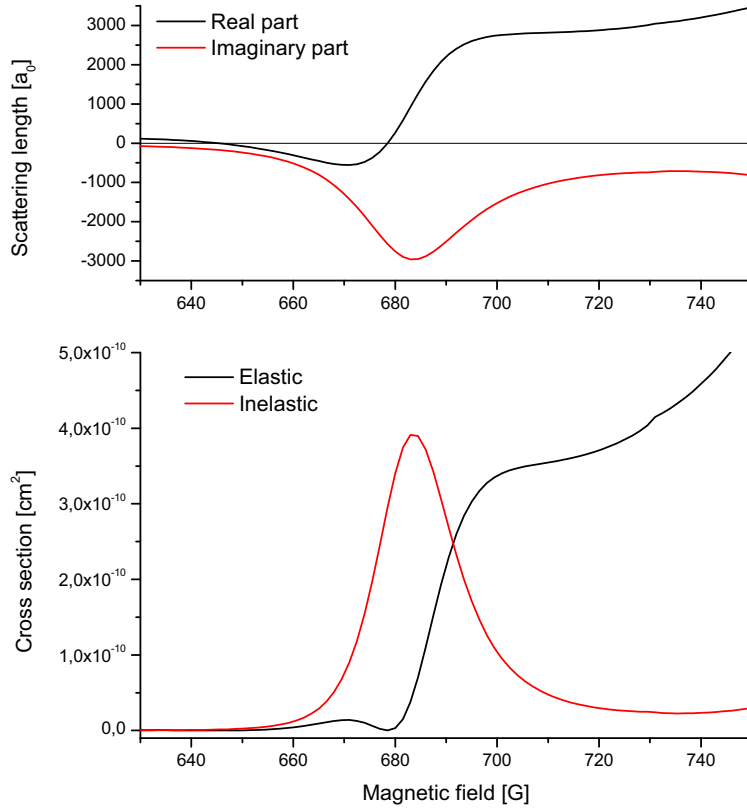


Figure 7.1: Real and imaginary parts of the scattering length (top) and the corresponding cross sections for elastic and inelastic collisions (bottom) in a $|1\rangle$ - $|23\rangle$ mixture as a function of the magnetic field. The curves were calculated using a mathematica notebook provided by D. Petrov [Pet10], where we set the three-body parameter to a value which reproduces the experimental results for the inelastic scattering. At a field of 685 G where the trimer state hits the atom-dimer threshold there is a scattering resonance. Due to the presence of inelastic channels in the system the scattering length does not diverge at the resonance position. As one can see the cross section for inelastic collisions is much larger than the elastic cross section in this region, therefore it is unclear whether it will be possible to use this resonance as an experimental tool.

body physics in a system it is therefore useful to compare the ratio of elastic and inelastic collisions to the average number of collisions per particle required to bring the system into equilibrium. This problem has been studied in the early days of cold atoms in the context of evaporative cooling. It was found that three collisions per particle are sufficient to bring a gas into thermal equilibrium [Ket96]. This means that even at the low ratio of elastic to inelastic collisions of the $|1\rangle$ - $|23\rangle$ atom-dimer mixture the system can be brought into thermal equilibrium.

However, the strongly interacting systems we are interested in are in the hydrodynamic regime, i.e. the mean free path of the particles is much shorter than the extension of the trap. For such systems changes of macroscopic parameters such as the density distribution can take much longer than the creation of a local thermal equilibrium. So while the ratio of elastic to inelastic collisions is good enough to create a local thermal equilibrium in the system, it is probably too small to reach equilibrium across the whole sample.

One way to circumvent this problem and study the behavior of such an unstable system is to study dynamical properties. This was done in a recent experiment with a two-component Fermi mixture of ^6Li and ^{40}K , which also has a low stability for strong interactions. In this experiment it could be shown that this interspecies mixture can be brought into the strongly interacting regime by studying the hydrodynamic expansion of the gas in the vicinity of a Feshbach resonance [Tre11].

While it is possible to extract information about the equation of state of the many-body system from such measurements, most of the experimental tools which have made the studies of two-component Fermi gases so successful cannot be applied to unstable systems. We will therefore discuss a method to increase the stability of a three-component Fermi gas of ^6Li in the next section.

7.2 Three-component Fermi gases in optical lattices

Inelastic three-atom and atom-dimer collisions are a convenient tool for studying the few-body physics of a three-component Fermi gas, but as we have seen in the previous section they also pose one of the greatest challenges for studying the many-body physics of the system. However, by putting the three-component gas into an optical lattice we should be able to use the high loss rate to prevent three-body loss and to stabilize the color superfluid phase, which would turn this bug into a feature.

To understand this counterintuitive effect let us consider a gas of ultracold atoms in an optical lattice, which is described by a Hubbard Hamiltonian with a tunneling energy J and an on-site interaction energy U . If the atoms are non-interacting ($U = 0$) all atoms are delocalized across the entire lattice. For an attractive in-

teraction $U < 0$ with $|U|/J \gg 1$ it is energetically favorable for three atoms to occupy the same lattice site. These three atoms can still tunnel as a composite object, which is called a trion. However, in a realistic system three strongly interacting atoms on a single lattice site will rapidly decay via three-body recombination.

If the decay rate is smaller than the single-particle tunneling rate J/h , the trionic state can be populated, which leads to the loss of particles from the system. However, if the decay rate is much faster than the tunneling rate the loss suppresses tunneling of atoms onto doubly occupied lattice sites and the trionic state is never populated. This is due to a quantum Zeno suppression of tunneling very similar to the suppression of RF-association discussed in Section 6.3.1.

To illustrate this let us consider a pair of atoms on a single lattice site and an atom on a neighboring site. If the tunneling rate is higher than the decay rate, the atom can tunnel onto the site occupied by the pair and the three atoms can be lost by three-body recombination.¹ If the decay rate is much faster than the tunneling rate, the decay serves as a continuous measurement which projects the tunneling atom back to its initial state. This leads to a suppression of tunneling onto doubly occupied sites and therefore to a suppression of three-body loss.

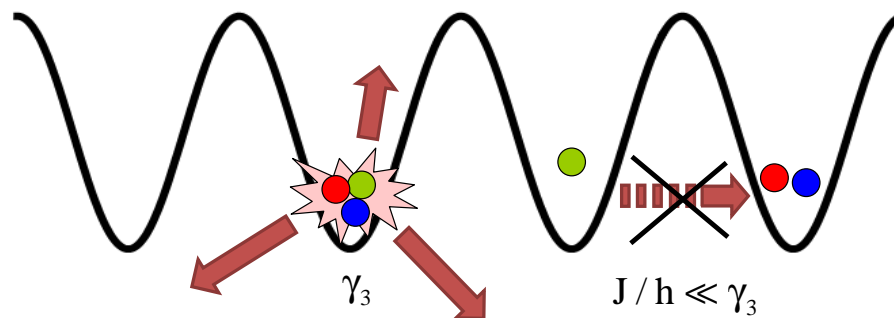


Figure 7.2: illustration of loss blocking in a three-component Fermi gas with strong interactions. If the loss rate γ_3 for three atoms confined to a single lattice site is much higher than tunneling rate J/h between two lattice sites the tunneling of atoms onto doubly occupied sites is suppressed by the quantum Zeno effect.

In a 2009 paper A. Kantian et al. calculated that the loss rate for a three-component Fermi gas scales with J^2/γ_3 , where γ_3 is the three-body loss rate for three atoms confined to a single lattice site [Kan09]. For sufficiently high loss rates this creates a three-body constraint that effectively eliminates the trionic state from the system.

¹For large interaction energy direct tunneling onto the occupied site is actually forbidden by energy conservation and a second order tunneling process proportional to J^2 becomes dominant, as shown in [Fol07]. However, this does not affect our qualitative argument.

This drastically alters the expected many-body behavior of the system. For a 2D or 3D system the new ground state has been predicted to be an atomic color superfluid, which is expected to show phase separation into a paired superfluid and a normal component. This phase separation should persist even for temperatures above the critical temperature for superfluidity and provide a clear experimental signature for the presence of the three-body constraint [Pri10].

The presence of these interesting phases and the enhanced stability make the lattice system a much more promising candidate for studying exciting many-body physics of three-component Fermi gases than the homogeneous case discussed in the previous section. Therefore we have begun to plan and set up an experiment to study three-component gases of ${}^6\text{Li}$ in an optical lattice.

To obtain direct optical access for in-situ imaging of the density distribution in the optical lattice we intend to work with a single two-dimensional layer of atoms. Such a reduced dimensionality can be created by trapping the atoms in an anisotropic confinement in which the level spacing along one axis is much larger than all other relevant energy scales in the system. In this case all atoms will be in the ground state of the trapping potential in this direction, which creates an effective 2D system. Once the atoms have been prepared in this 2D geometry it is straightforward to add an optical lattice in the 2D plane using a pair of retroreflected laser beams. Such two-dimensional lattice experiments with in-situ imaging have been recently realized with ultracold bosons [Gem09, Bak10, She10], which will allow us to adapt existing technology to our fermionic system.

Our planned setup, which is similar to the approach followed in [Gem09], is shown in Fig. 7.3: Two laser beams with a wavelength of 1064 nm intersecting under an angle of about 15° will create a standing wave pattern with a spacing of about $4\ \mu\text{m}$, which will provide the 2D confinement. The lattice will be created by two pairs of retroreflected laser beams, which create a sinusoidal confinement with a spacing of 532 nm in the horizontal plane. The atoms in this lattice potential can be directly imaged with high resolution using a high numerical aperture objective.

The first key challenge in these experiments will be to prepare a degenerate three-component Fermi gas in an optical lattice. The standard approach for loading a two-component gas into an optical lattice is to start from a degenerate Fermi gas in an optical dipole trap and slowly ramp up the periodic potential. For a three-component gas there is the additional challenge that the system is only stable if the interactions are weak – this is the case both with and without the lattice – or if the sample is in an optical lattice with $\gamma_3 \gg J$.

Let us examine how this affects the lattice loading process. If we start from a three-component Fermi gas with weak interactions, we can easily load this gas into an optical lattice, but if the gas is degenerate this loading process will create a large number of triply occupied sites. As soon as we try to bring this gas into

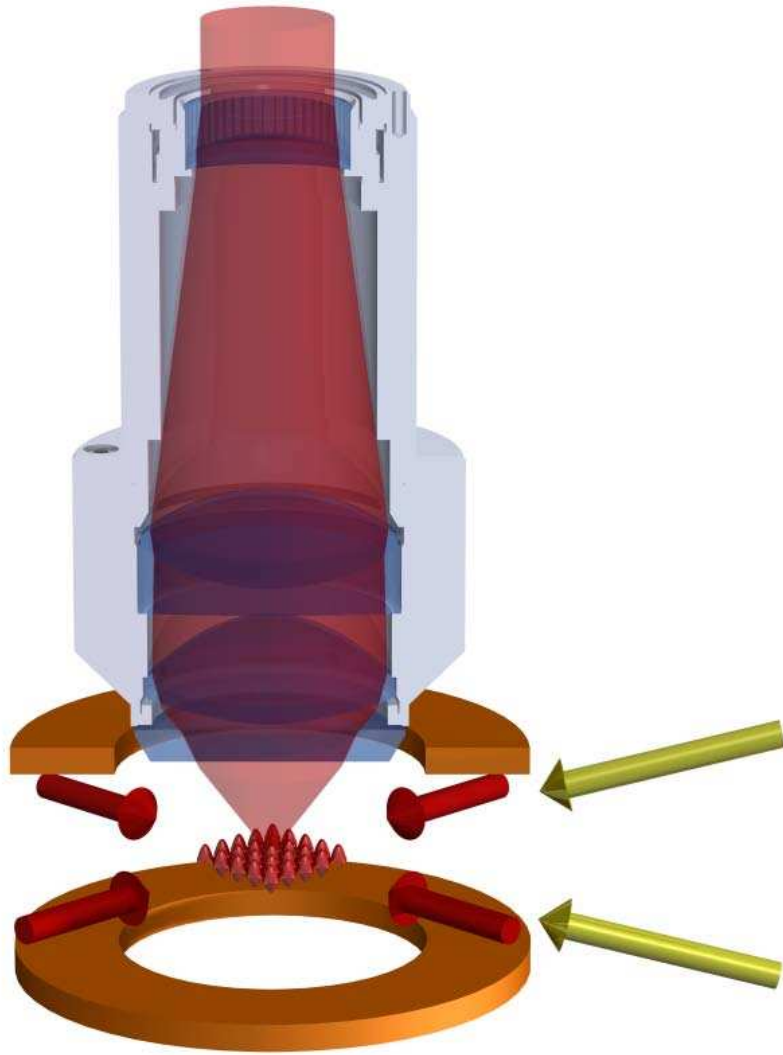


Figure 7.3: Sketch of the planned setup for the two-dimensional optical lattice. The 2D confinement is provided by two laser beams intersecting under an angle of 15° (yellow). The lattice potential in this 2D plane is created by crossing two pairs of retroreflected laser beams (red). The atoms in the lattice potential can be imaged with high resolution using a large aperture objective, which can also be used to create arbitrary optical potentials for the atoms. The magnetic field coils for creating the Feshbach field are shown in brown.

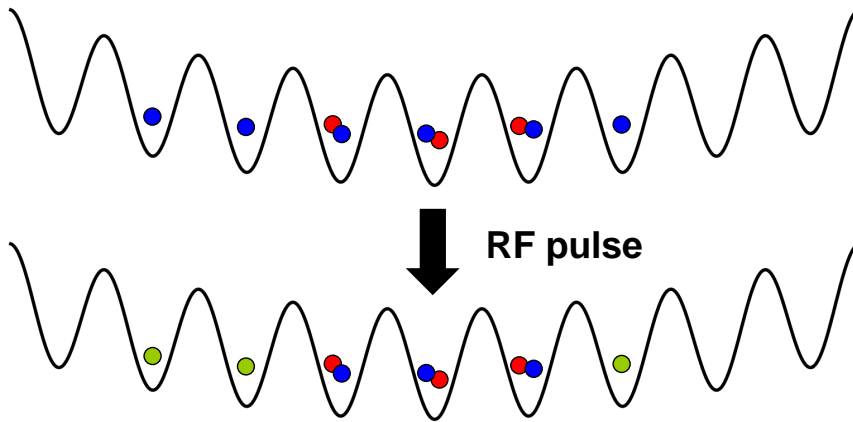


Figure 7.4: Sketch illustrating our planned scheme for creating a deeply degenerate three-component Fermi gas in an optical lattice. For an imbalanced two-component Fermi gas with strong attractive interactions at sufficiently low temperature all minority atoms are on doubly occupied lattice sites. The unpaired majority atoms can then be addressed independently with an RF-pulse to create a three-component sample.

the strongly interacting regime the atoms on these triply occupied sites will be lost via three-body recombination. If one tried to prevent this by performing the loading process in a region with a higher three-body loss rate, the sample would decay during the slow loading process that is required to prevent excessive heating of the gas. Therefore starting from a three-component gas is not a viable loading scheme, and we need a different approach for initializing our system.

Our plan is to start by loading a degenerate, imbalanced two-component Fermi gas into the optical lattice. For the following discussion we will assume a gas of atoms in states $|1\rangle$ and $|2\rangle$ with more atoms in state $|2\rangle$. For attractive interactions this sample would align itself in the lattice as shown in Fig. 7.4.

When one tries to drive an RF-transition between state $|2\rangle$ and state $|3\rangle$ for an atom on a doubly occupied site, the transition will be shifted by the difference of the interaction energies U_{12} and U_{13} of the initial and final state. This is comparable to driving a bound-bound transition between two molecules as shown in Fig. 6.2. If the difference between U_{12} and U_{13} is sufficiently large, the atoms in state $|2\rangle$ on singly occupied sites can be driven to the third state without affecting atoms on doubly occupied sites. This technique has already been used to measure the suppression of doubly occupied sites in a fermionic Mott insulator [Jor08].

If we start from a two-component Fermi gas in a magnetic field region where the three-body loss is large enough to prevent the formation of triply occupied sites, this technique can also be used to prepare stable three-component Fermi gases

in optical lattices. Those gases could then be used as a starting point for further experiments which study the many-body physics of three-component Fermi gases in optical lattices.

Chapter 8

Conclusion and outlook

When we created the first ultracold three-component Fermi gas three years ago, there was only very little knowledge about the physics one could expect to find in such a gas. Therefore we began our studies of this system by exploring its few-body physics, which turned out to be dominated by universal three-body bound states, the so-called Efimov trimers. To study the properties of these trimer states we observed their effect on the three-atom and atom-dimer scattering in our system. We did this by measuring the rate constants for inelastic collisions for a three-atom and three different atom-dimer mixtures of ${}^6\text{Li}$. The main results from these measurements are summarized in Fig. 8.1.

We observed resonances in the inelastic three-atom and atom-dimer scattering, which allowed to determine the critical values of the interaction strength at which the energy of an Efimov state becomes degenerate with the three-atom or atom-dimer continuum (red diamonds in Fig. 8.1) [Ott08, Wen09b, Lom10a]. From the results of such collision measurements the binding energies of the Efimov states in ${}^6\text{Li}$ were calculated by extending Efimov's scenario to the case of three distinguishable particles [Bra10, Nak10b, Nai10].

Additionally, our measurements of inelastic atom-dimer collisions allowed us to study ultracold chemistry of universal molecules. We showed that these chemical reactions are influenced by the presence of universal trimer states by observing interference minima in the rate of $|3\rangle + |12\rangle \rightarrow |1\rangle + |23\rangle$ exchange reactions (black squares in Fig. 8.1) [Lom10a].

The ${}^6\text{Li}$ system also turned out to be uniquely suited for directly observing Efimov trimers with RF-spectroscopy. This has allowed us to directly measure the binding energy of a universal trimer state as a function of the strength of the interparticle interactions [Lom10b]. The results of these measurements are shown in Fig. 8.1 as blue circles and are in good agreement with the predictions for the trimer binding energy made by universal theory.

With our measurements we have obtained direct experimental proof for the exis-

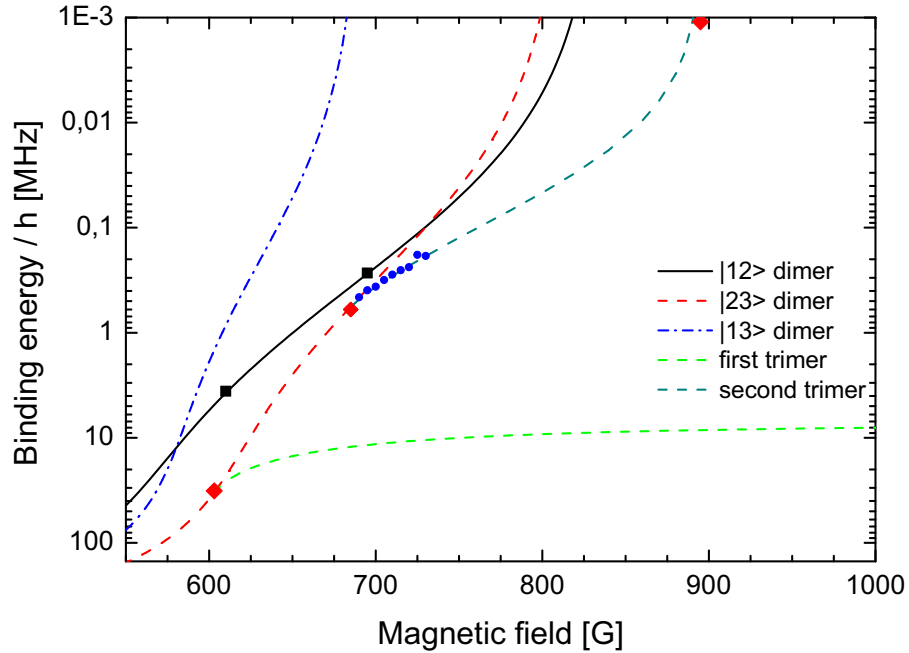


Figure 8.1: Summary of the main experimental results presented in this thesis. The binding energies of the universal dimer and trimer states are plotted as a function of the magnetic field. The red diamonds show the points at which a trimer state becomes degenerate with the three-atom or atom-dimer continuum; these were determined from measurements of inelastic three-atom and atom-dimer collisions. The black squares indicate the positions of the minima in the rate of molecular exchange reactions observed in a $|3\rangle$ - $|12\rangle$ atom-dimer mixture. The blue circles show the measurements of the binding energy of the second Efimov trimer by RF-association spectroscopy.

tence of universal trimer states. Our results show that the theoretical framework developed by V. Efimov more than thirty years ago [Efi79] gives an accurate description of these trimer states. This is a direct experimental confirmation of the Efimov effect, which is one of the paradigms of few-body physics.

In addition to advancing our general understanding of universal few-body physics, our experiments have also given us detailed knowledge about the scattering properties of three-component gases of ${}^6\text{Li}$. This puts us in a position where we can begin to work towards our next major goal: To study the many-body physics of three-component Fermi gases.

As shown in chapter 7, the most promising approach to studying strongly correlated three-component Fermi system is to prepare the system in an optical lattice. For sufficiently high three-body loss rates there is a suppression of tunneling

onto doubly occupied lattice sites. If the system is initialized properly, this does not only suppress three-body loss, it also effectively removes the universal trimer states from the phase diagram shown in Fig. 2.9. The presence of a periodic potential can therefore greatly extend the parameter space where one can expect to find color superfluid phases.

Given the knowledge and techniques we have obtained in our studies of the few-body physics of the system, we are confident that we can use the preparation scheme introduced in sect. 7.2 to create stable three-component gases in optical lattices. This would give physicists access to a completely new and exciting playground where phenomena such as pairing and superfluidity or even quantum magnetism could be studied in an exotic fermionic system.

Bibliography

- [ALI10] ALICE Collaboration, *Elliptic Flow of Charged Particles in Pb-Pb Collisions at $\sqrt{s_{NN}} = 2.76$ TeV*, Phys. Rev. Lett. **105**, 252302 (2010).
- [And95] M. H. Anderson, J. R. Ensher, M. R. Matthews, C. E. Wieman, E. A. Cornell, *Observation of Bose-Einstein condensation in a Dilute Atomic Vapor*, Science **269**, 198–201 (1995).
- [ATL10] ATLAS Collaboration, *Observation of a Centrality-Dependent Dijet Asymmetry in Lead-Lead Collisions at $\sqrt{s_{NN}} = 2.76$ TeV with the ATLAS Detector at the LHC*, Phys. Rev. Lett. **105**, 252303 (2010).
- [Bak10] W. S. Bakr, A. Peng, M. E. Tai, R. Ma, J. Simon, J. I. Gillen, S. Fölling, L. Pollet, M. Greiner, *Probing the Superfluid-to-Mott Insulator Transition at the Single-Atom Level*, Science **329**, 547–550 (2010).
- [Bar57a] J. Bardeen, L. N. Cooper, J. R. Schrieffer, *Microscopic Theory of Superconductivity*, Phys. Rev. **106**, 162–164 (1957).
- [Bar57b] J. Bardeen, L. N. Cooper, J. R. Schrieffer, *Theory of superconductivity*, Phys. Rev. **108**, 1175–1204 (1957).
- [Bar04a] M. Bartenstein, A. Altmeyer, S. Riedl, S. Jochim, C. Chin, J. H. Denschlag, R. Grimm, *Collective Excitations of a Degenerate Gas at the BEC-BCS Crossover*, Phys. Rev. Lett. **92**, 203201 (2004).
- [Bar04b] M. Bartenstein, A. Altmeyer, S. Riedl, S. Jochim, C. Chin, J. H. Denschlag, R. Grimm, *Crossover from a molecular Bose-Einstein condensate to a Degenerate Fermi Gas*, Phys. Rev. Lett. **92**, 120401 (2004).
- [Bar05] M. Bartenstein, A. Altmeyer, S. Riedl, R. Geursen, S. Jochim, C. Chin, J. H. Denschlag, R. Grimm, A. Simoni, E. Tiesinga, C. J. Williams, P. S. Julienne, *Precise Determination of ^6Li Cold Collision Parameters by Radio-Frequency Spectroscopy on Weakly Bound Molecules*, Phys. Rev. Lett. **94**, 103201 (2005).
- [Bar09] G. Barontini, C. Weber, F. Rabatti, J. Catani, G. Thalhammer, M. Inguscio, F. Minardi, *Observation of Heteronuclear Atomic Efimov Resonances*, Phys. Rev. Lett. **103**, 043201 (2009).

- [Ber11] M. Berninger, *Private Communication* (2011).
- [Blu08] D. Blume, S. T. Rittenhouse, J. von Stecher, C. H. Greene, *Stability of inhomogeneous multicomponent Fermi gases*, *Phys. Rev. A* **77**, 033627 (2008).
- [Bou03] T. Bourdel, J. Cubizolles, L. Khaykovich, K. M. F. Magalhães, S. J. J. M. F. Kokkelmans, G. V. Shlyapnikov, C. Salomon, *Measurement of the Interaction Energy near a Feshbach Resonance in a ${}^6\text{Li}$ Fermi Gas*, *Phys. Rev. Lett.* **91**, 020402 (2003).
- [Bra04] E. Braaten, M. Kusunoki, *Production of the X(3870) at the Upsilon (4S) by the coalescence of charm mesons*, *Phys. Rev. D* **69**, 114012 (2004).
- [Bra06] E. Braaten, H. W. Hammer, *Universality in Few-body Systems with Large Scattering Length*, *Physics Reports* **428**, 259 (2006).
- [Bra09] E. Braaten, H.-W. Hammer, D. Kang, L. Platter, *Three-Body Recombination of ${}^6\text{Li}$ Atoms with Large Negative Scattering Lengths*, *Phys. Rev. Lett.* **103**, 073202 (2009).
- [Bra10] E. Braaten, H. W. Hammer, D. Kang, L. Platter, *Efimov physics in ${}^6\text{Li}$ atoms*, *Phys. Rev. A* **81**, 013605 (2010).
- [Bus07] T. Busch, B.-G. Englert, K. Rzazewski, M. Wilkens, *Two Cold Atoms in a Harmonic Trap*, *Foundations of Physics* **28**, 549–559 (1998-04-07).
- [Chi04a] C. Chin, M. Bartenstein, A. Altmeyer, S. Riedl, S. Jochim, J. H. Denschlag, R. Grimm, *Observation of the Pairing Gap in a Strongly Interacting Fermi Gas*, *Science* **305**, 1128–1130 (2004).
- [Chi04b] C. Chin, R. Grimm, *Thermal equilibrium and efficient evaporation of an ultracold atom-molecule mixture*, *Phys. Rev. A* **69**, 033612 (2004).
- [Chi10] C. Chin, R. Grimm, P. Julienne, E. Tiesinga, *Feshbach resonances in ultracold gases*, *Rev. Mod. Phys.* **82**, 1225 (2010).
- [Clo62] A. M. Clogston, *Upper Limit for the Critical Field in Hard Superconductors*, *Phys. Rev. Lett.* **9**, 266 (1962).
- [Coo56] L. N. Cooper, *Bound Electron Pairs in a Degenerate Fermi Gas*, *Phys. Rev.* **104**, 1189–1190 (1956).
- [Cub03] J. Cubizolles, T. Bourdel, S. J. J. M. F. Kokkelmans, G. V. Shlyapnikov, C. Salomon, *Production of Long-Lived Ultracold Li_2 Molecules from a Fermi Gas*, *Phys. Rev. Lett.* **91**, 240401 (2003).
- [Dal98] J. Dalibard, *Collisional dynamics of ultracold atomic gases*, in M. Inguscio, S. Stringari, C. Wieman (Ed.), *Bose-Einstein Condensation in Atomic Gases*, Vol. Course CXL of *Proceedings of the International School of Physics Enrico Fermi* (IOS Press, Varenna, 1998).

- [Dav95] K. B. Davis, M. O. Mewes, M. R. Andrews, N. J. van Druten, D. S. Durfee, D. M. Kurn, W. Ketterle, *Bose-Einstein condensation in a gas of sodium atoms*, Phys. Rev. Lett. **75**, 3969–3973 (1995).
- [Del60] L. M. Delves, *Tertiary and general-order collisions (II)*, Nuclear Physics **20**, 275 – 308 (1960).
- [DeM99] B. DeMarco, D. S. Jin, *Onset of Fermi degeneracy in a trapped atomic gas*, Science **285**, 1703–1706 (1999).
- [D’I04] J. P. D’Incao, H. Suno, B. D. Esry, *Limits on Universality in Ultracold Three-Boson Recombination*, Phys. Rev. Lett. **93**, 123201 (2004).
- [D’I08] J. P. D’Incao, B. D. Esry, C. H. Greene, *Ultracold atom-molecule collisions with fermionic atoms*, Phys. Rev. A **77**, 052709 (2008).
- [D’I09] J. P. D’Incao, B. D. Esry, *Ultracold Three-Body Collisions near Overlapping Feshbach Resonances*, Phys. Rev. Lett. **103**, 083202 (2009).
- [Die02] K. Dieckmann, C. A. Stan, S. Gupta, Z. Hadzibabic, C. H. Schunck, W. Ketterle, *Decay of an Ultracold Fermionic Lithium Gas near a Feshbach Resonance*, Phys. Rev. Lett. **89**, 203201 (2002).
- [Du09] X. Du, Y. Zhang, J. E. Thomas, *Inelastic Collisions of a Fermi Gas in the BEC-BCS Crossover*, Phys. Rev. Lett. **102**, 250402 (2009).
- [Efi70] V. Efimov, *Energy levels arising from resonant two-body forces in a three-body system*, Physics Letters B **33**, 563 – 564 (1970).
- [Efi71] V. Efimov, *Weakly-bound states of three resonantly-interacting particles*, Sov. J. Nucl. Phys. **12**, 589–595 (1971), originally: Yad. Fiz. **12**, 1080-1091 (1970).
- [Efi79] V. Efimov, *Low-energy properties of three resonantly interacting particles*, Sov. J. Nucl. Phys. **29**, 546–553 (1979), originally: Yad. Fiz. **29**, 1058-1069 (1979).
- [Ein25] A. Einstein, *Quantentheorie des einatomigen idealen Gases. Zweite Abhandlung*, Sitzungsberichte der preussischen Akademie der Wissenschaften **1** (1925).
- [Esr99] B. D. Esry, C. H. Greene, J. P. Burke, *Recombination of Three Atoms in the Ultracold Limit*, Phys. Rev. Lett. **83**, 1751–1754 (1999).
- [Esr01] B. D. Esry, C. H. Greene, H. Suno, *Threshold laws for three-body recombination*, Phys. Rev. A **65**, 010705 (2001).
- [Fed93] D. V. Fedorov, A. S. Jensen, *Efimov effect in coordinate space Faddeev equations*, Phys. Rev. Lett. **71**, 4103–4106 (1993).

- [Fer09] F. Ferlaino, S. Knoop, M. Berninger, W. Harm, J. P. D’Incao, H.-C. Nägerl, R. Grimm, *Evidence for Universal Four-Body States Tied to an Efimov Trimer*, Phys. Rev. Lett. **102**, 140401 (2009).
- [Fli05] T. Fließbach, *Quantenmechanik* (Spektrum Akademischer Verlag, 2005).
- [Flo09] S. Floerchinger, R. Schmidt, C. Wetterich, *Three-body loss in lithium from functional renormalization*, Phys. Rev. A **79**, 053633 (2009).
- [Fol07] S. Folling, S. Trotzky, P. Cheinet, M. Feld, R. Saers, A. Widera, T. Müller, I. Bloch, *Direct observation of second-order atom tunnelling*, Nature **448**, 1029–1032 (2007).
- [Gem09] N. Gemelke, X. Zhang, C.-L. Hung, C. Chin, *In situ observation of incompressible Mott-insulating domains in ultracold atomic gases*, Nature **460**, 995–998 (2009).
- [Gra02] S. R. Granade, M. E. Gehm, K. M. O’Hara, J. E. Thomas, *All-Optical Production of a Degenerate Fermi Gas*, Phys. Rev. Lett. **88**, 120405 (2002).
- [Gre03] M. Greiner, C. A. Regal, D. S. Jin, *Emergence of a molecular Bose-Einstein condensate from a Fermi gas*, Nature **426**, 537–540 (2003).
- [Gri93] G. F. Gribakin, V. V. Flambaum, *Calculation of the scattering length in atomic collisions using the semiclassical approximation*, Phys. Rev. A **48**, 546 (1993).
- [Gro09] N. Gross, Z. Shotan, S. Kokkelmans, L. Khaykovich, *Observation of Universality in Ultracold ^7Li Three-Body Recombination*, Phys. Rev. Lett. **103**, 163202 (2009).
- [Gro10] N. Gross, Z. Shotan, S. Kokkelmans, L. Khaykovich, *Nuclear-Spin-Independent Short-Range Three-Body Physics in Ultracold Atoms*, Phys. Rev. Lett. **105**, 103203 (2010).
- [Had03] Z. Hadzibabic, S. Gupta, C. A. Stan, C. H. Schunck, M. W. Zwierlein, K. Dieckmann, W. Ketterle, *Fiftyfold Improvement in the Number of Quantum Degenerate Fermionic Atoms*, Phys. Rev. Lett. **91**, 160401 (2003).
- [Ham10] H.-W. Hammer, D. Kang, L. Platter, *Efimov physics in atom-dimer scattering of ^6Li atoms*, Phys. Rev. A **82**, 022715 (2010).
- [Hei01] H. Heiselberg, *Fermi systems with long scattering lengths*, Phys. Rev. A **63**, 043606 (2001).
- [Hon04] C. Honerkamp, W. Hofstetter, *BCS pairing in Fermi systems with N different hyperfine states*, Phys. Rev. B **70**, 094521 (2004).

- [Hor10] M. Horikoshi, S. Nakajima, M. Ueda, T. Mukaiyama, *Measurement of Universal Thermodynamic Functions for a Unitary Fermi Gas*, *Science* **327**, 442–445 (2010).
- [Hou98] M. Houbiers, H. T. C. Stoof, W. I. McAlexander, R. G. Hulet, *Elastic and inelastic collisions of ^6Li atoms in magnetic and optical traps*, *Phys. Rev. A* **57**, 1497 (R) (1998).
- [Huc09] J. H. Huckans, J. R. Williams, E. L. Hazlett, R. W. Stites, K. M. O’Hara, *Three-Body Recombination in a Three-State Fermi Gas with Widely Tunable Interactions*, *Phys. Rev. Lett.* **102**, 165302 (2009).
- [Ino98] S. Inouye, M. R. Andrews, J. Stenger, H.-J. Miesner, D. M. Stamper Kurn, W. Ketterle, *Observation of Feshbach resonances in a Bose-Einstein condensate*, *Nature* **392**, 151–154 (1998).
- [Ita90] W. M. Itano, D. J. Heinzen, J. J. Bollinger, D. J. Wineland, *Quantum Zeno effect*, *Phys. Rev. A* **41**, 2295 (1990).
- [Joc03a] S. Jochim, M. Bartenstein, A. Altmeyer, G. Hendl, C. Chin, J. H. Denschlag, R. Grimm, *Pure Gas of Optically Trapped Molecules Created from Fermionic Atoms*, *Phys. Rev. Lett.* **91**, 240402 (2003).
- [Joc03b] S. Jochim, M. Bartenstein, A. Altmeyer, G. Hendl, S. Riedl, C. Chin, J. Hecker Denschlag, R. Grimm, *Bose-Einstein condensation of molecules*, *Science* **302**, 2101–2103 (2003).
- [Joc04] S. Jochim, *Bose-Einstein Condensation of Molecules*, Dissertation, Universität Innsbruck (2004).
- [Jor08] R. Jordens, N. Strohmaier, K. Gunter, H. Moritz, T. Esslinger, *A Mott insulator of fermionic atoms in an optical lattice*, *Nature* **455**, 204–207 (2008).
- [Kan09] A. Kantian, M. Dalmonte, S. Diehl, W. Hofstetter, P. Zoller, A. J. Daley, *Atomic Color Superfluid via Three-Body Loss*, *Phys. Rev. Lett.* **103**, 240401 (2009).
- [Ket96] W. Ketterle, N. V. Druten, *Evaporative Cooling of Trapped Atoms*, in B. Bederson, H. Walther (Ed.), *Advances In Atomic, Molecular, and Optical Physics*, Vol. 37, 181–236 (Academic Press, 1996).
- [Ket08] W. Ketterle, M. W. Zwierlein, *Making, probing and understanding ultracold Fermi gases*, in: M. Inguscio, W. Ketterle, and C. Salomon (Eds.); *Ultracold Fermi Gases*, Proceedings of the International School of Physics - Enrico Fermi **Course CLXIV**, IOS Press (2008).
- [Kin04] J. Kinast, S. L. Hemmer, M. E. Gehm, A. Turlapov, J. E. Thomas, *Evidence for Superfluidity in a Resonantly Interacting Fermi Gas*, *Phys. Rev. Lett.* **92**, 150402 (2004).

- [Kno09] S. Knoop, F. Ferlaino, M. Mark, M. Berninger, H. Schobel, H.-C. Nägerl, R. Grimm, *Observation of an Efimov-like trimer resonance in ultracold atom-dimer scattering*, *Nature Physics* **5**, 227 (2009).
- [Kno10] S. Knoop, F. Ferlaino, M. Berninger, M. Mark, H.-C. Nägerl, R. Grimm, J. P. D’Incao, B. D. Esry, *Magnetically Controlled Exchange Process in an Ultracold Atom-Dimer Mixture*, *Phys. Rev. Lett.* **104**, 053201 (2010).
- [Koh08] M. Kohnen, *Ultracold Fermi Mixtures in an Optical Dipole Trap*, Diploma thesis (2008).
- [Kra06] T. Kraemer, M. Mark, P. Waldburger, J. G. Danzl, C. Chin, B. Engeser, A. D. Lange, K. Pilch, A. Jaakkola, H.-C. Nägerl, R. Grimm, *Evidence for Efimov quantum states in an ultracold gas of caesium atoms*, *Nature* **440**, 315–318 (2006).
- [Leg80] A. Leggett, *Diatomic molecules and cooper pairs*, in A. Pekalski, J. Przystawa (Ed.), *Lecture Notes in Physics*, Vol. 115, 13–27 (Springer Berlin / Heidelberg, 1980).
- [Lev09] J. Levinsen, T. G. Tiecke, J. T. M. Walraven, D. S. Petrov, *Atom-Dimer Scattering and Long-Lived Trimers in Fermionic Mixtures*, *Phys. Rev. Lett.* **103**, 153202 (2009).
- [Lom08] T. Lompe, *An apparatus for the production of molecular Bose-Einstein condensates*, Diploma thesis (2008).
- [Lom10a] T. Lompe, T. B. Ottenstein, F. Serwane, K. Viering, A. N. Wenz, G. Zürn, S. Jochim, *Atom-Dimer Scattering in a Three-Component Fermi Gas*, *Phys. Rev. Lett.* **105**, 103201 (2010).
- [Lom10b] T. Lompe, T. B. Ottenstein, F. Serwane, A. N. Wenz, G. Zürn, S. Jochim, *Radio-Frequency Association of Efimov Trimers*, *Science* **330**, 940–944 (2010).
- [Luo06] L. Luo, B. Clancy, J. Joseph, J. Kinast, A. Turlapov, J. E. Thomas, *Evaporative cooling of unitary Fermi gas mixtures in optical traps*, *New Journal of Physics* **8**, 213 (2006).
- [Mar08] B. Marcelis, S. J. J. M. F. Kokkelmans, G. V. Shlyapnikov, D. S. Petrov, *Collisional properties of weakly bound heteronuclear dimers*, *Phys. Rev. A* **77**, 032707 (2008).
- [Met99] H. J. Metcalf, P. van der Straten, *Laser Cooling and Trapping* (Springer-Verlag, New York, 1999).
- [Mis77] B. Misra, E. C. G. Sudarshan, *The Zeno’s paradox in quantum theory*, *J. Math. Phys.* **18**, 756–763 (1977).

- [Mos01] A. Mosk, S. Jochim, H. Moritz, T. Elsässer, M. Weidemüller, R. Grimm, *Resonator-enhanced optical dipole trap for fermionic lithium atoms*, *Opt. Lett.* **26**, 1837–1839 (2001).
- [Mot37] N. F. Mott, R. Peierls, *Discussion of the paper by de Boer and Verwey*, *Proceedings of the Physical Society* **49**, 72 (1937).
- [Nai09] P. Naidon, M. Ueda, *Possible Efimov Trimer State in a Three-Hyperfine-Component Lithium-6 Mixture*, *Phys. Rev. Lett.* **103**, 073203 (2009).
- [Nai10] P. Naidon, M. Ueda, *The Efimov effect in Lithium 6*, arXiv:1008.2260 (2010).
- [Nak10a] S. Nakajima, M. Horikoshi, T. Mukaiyama, P. Naidon, M. Ueda, *Measurement of an Efimov trimer binding energy in a three-component mixture of ^6Li* , arXiv:1010.1954 (2010).
- [Nak10b] S. Nakajima, M. Horikoshi, T. Mukaiyama, P. Naidon, M. Ueda, *Nonuniversal Efimov Atom-Dimer Resonances in a Three-Component Mixture of ^6Li* , *Phys. Rev. Lett.* **105**, 023201 (2010).
- [Nas09] S. Nascimbéne, N. Navon, K. J. Jiang, L. Tarruell, M. Teichmann, J. McKeever, F. Chevy, C. Salomon, *Collective Oscillations of an Imbalanced Fermi Gas: Axial Compression Modes and Polaron Effective Mass*, *Phys. Rev. Lett.* **103**, 170402 (2009).
- [Nas10] S. Nascimbéne, N. Navon, K. J. Jiang, F. Chevy, C. Salomon, *Exploring the thermodynamics of a universal Fermi gas*, *Nature* **463**, 1057–1060 (2010).
- [Nie99] E. Nielsen, J. H. Macek, *Low-Energy Recombination of Identical Bosons by Three-Body Collisions*, *Phys. Rev. Lett.* **83**, 1566–1569 (1999).
- [Noz85] P. Nozières, S. Schmitt-Rink, *Bose condensation in an attractive fermion gas: From weak to strong coupling superconductivity*, *Journal of Low Temperature Physics* **59**, 195–211 (1985), 10.1007/BF00683774.
- [O’H01] K. M. O’Hara, M. E. Gehm, S. R. Granade, J. E. Thomas, *Scaling laws for evaporative cooling in time-dependent optical traps*, *Phys. Rev. A* **64**, 051403 (2001).
- [O’H02] K. M. O’Hara, S. L. Hemmer, M. E. Gehm, S. R. Granade, J. E. Thomas, *Observation of a Strongly Interacting Degenerate Fermi Gas of Atoms*, *Science* **298**, 2179–2182 (2002).
- [Onn11] H. K. Onnes, *Further Experiments with Liquid Helium: On the Change of the Electrical Resistance of pure Metals at very low Temperatures, etc. V. The disappearance of the resistance of mercury.*, *Communications from the Physical Laboratory of the University of Leiden* **122**, 13–15 (1911).

- [Ott08] T. B. Ottenstein, T. Lompe, M. Kohnen, A. N. Wenz, S. Jochim, *Collisional Stability of a Three-Component Degenerate Fermi Gas*, Phys. Rev. Lett. **101**, 203202 (2008).
- [Ott10] T. B. Ottenstein, *Few-body physics in ultracold Fermi gases*, Dissertation, University of Heidelberg (2010).
- [Paa06] T. Paananen, J.-P. Martikainen, P. Törmä, *Pairing in a three-component Fermi gas*, Phys. Rev. A **73**, 053606 (2006).
- [Paa07] T. Paananen, P. Törmä, J.-P. Martikainen, *Coexistence and shell structures of several superfluids in trapped three-component Fermi mixtures*, Phys. Rev. A **75**, 023622 (2007).
- [Par06] G. B. Partridge, W. Li, R. I. Kamar, Y.-a. Liao, R. G. Hulet, *Pairing and Phase Separation in a Polarized Fermi Gas*, Science **311**, 503–505 (2006).
- [Pet03] D. S. Petrov, *Three-body problem in Fermi gases with short-range interparticle interaction*, Phys. Rev. A **67**, 010703 (2003).
- [Pet04] D. S. Petrov, C. Salomon, G. V. Shlyapnikov, *Weakly Bound Dimers of Fermionic Atoms*, Phys. Rev. Lett. **93**, 090404 (2004).
- [Pet05] D. S. Petrov, C. Salomon, G. V. Shlyapnikov, *Scattering properties of weakly bound dimers of fermionic atoms*, Phys. Rev. A **71**, 012708 (2005).
- [Pet10] D. S. Petrov, *Private Communication* (2010).
- [PHE05] PHENIX Collaboration, *Formation of dense partonic matter in relativistic nucleus-nucleus collisions at RHIC: Experimental evaluation by the PHENIX Collaboration*, Nuclear Physics A **757**(1-2), 184–283 (August 2005).
- [PHE10] PHENIX Collaboration, *Enhanced Production of Direct Photons in Au+Au Collisions at $\sqrt{s_{NN}} = 200$ GeV and Implications for the Initial Temperature*, Phys. Rev. Lett. **104**, 132301 (2010).
- [Pit03] L. Pitaevski, S. Stringari, *Bose-Einstein-Condensation* (Oxford Science Publications, 2003).
- [Pol09] S. E. Pollack, D. Dries, R. G. Hulet, *Universality in Three- and Four-Body Bound States of Ultracold Atoms*, Science **326**, 1683–1685 (2009).
- [Pri10] A. Privitera, I. Titvinidze, S. Chang, S. Diehl, A. J. Daley, W. Hofstetter, *Loss-induced phase separation and pairing for 3-species atomic lattice fermions*, arxiv:1010.0114 (2010).
- [Rap07] Ákos Rapp, G. Zaránd, C. Honerkamp, W. Hofstetter, *Color Superfluidity and “Baryon” Formation in Ultracold Fermions*, Phys. Rev. Lett. **98**, 160405 (2007).

- [Rap08] A. Rapp, W. Hofstetter, G. Zaránd, *Trionic phase of ultracold fermions in an optical lattice: A variational study*, Phys. Rev. B **77**, 144520 (2008).
- [Reg03] C. A. Regal, C. Ticknor, J. L. Bohn, D. S. Jin, *Creation of ultracold molecules from a Fermi gas of atoms*, Nature **424**, 47–50 (2003).
- [Reg04] C. A. Regal, M. Greiner, D. S. Jin, *Lifetime of Molecule-Atom Mixtures near a Feshbach Resonance in ^{40}K* , Phys. Rev. Lett. **92**, 083201 (2004).
- [RG00] M. W. R. Grimm, Y. B. Ovchinnikov, *Optical dipole traps for neutral atoms*, Advances in Atomic, Molecular and Optical Physics **42**, 95 (2000).
- [Rit10] S. T. Rittenhouse, *Magnetic-field dependence and Efimov resonance broadening in ultracold three-body recombination*, Phys. Rev. A **81**, 040701 (2010).
- [Sch99] U. Schünemann, H. Engler, R. Grimm, M. Weidemüller, M. Zielonkowski, *Simple scheme for tunable frequency offset locking of two lasers*, Rev. Sci. Instrum. **70**, 242–243 (1999).
- [Sch01] F. Schreck, G. Ferrari, K. L. Corwin, J. Cubizolles, L. Khaykovich, M.-O. Mewes, C. Salomon, *Sympathetic cooling of bosonic and fermionic lithium gases towards quantum degeneracy*, Phys. Rev. A **64**, 011402 (2001).
- [Sch07] C. H. Schunck, M. W. Zwierlein, A. Schirotzek, W. Ketterle, *Superfluid Expansion of a Rotating Fermi Gas*, Phys. Rev. Lett. **98**, 050404 (2007).
- [Sch08a] A. Schirotzek, Y.-i. Shin, C. H. Schunck, W. Ketterle, *Determination of the Superfluid Gap in Atomic Fermi Gases by Quasiparticle Spectroscopy*, Phys. Rev. Lett. **101**, 140403 (2008).
- [Sch08b] U. Schneider, L. Hackermüller, S. Will, T. Best, I. Bloch, T. A. Costi, R. W. Helmes, D. Rasch, A. Rosch, *Metallic and Insulating Phases of Repulsively Interacting Fermions in a 3D Optical Lattice*, Science **322**, 1520–1525 (2008).
- [Sch08c] C. H. Schunck, Y.-i. Shin, A. Schirotzek, W. Ketterle, *Determination of the fermion pair size in a resonantly interacting superfluid*, Nature **454**, 739–743 (2008).
- [Sch09] A. Schirotzek, C.-H. Wu, A. Sommer, M. W. Zwierlein, *Observation of Fermi Polarons in a Tunable Fermi Liquid of Ultracold Atoms*, Phys. Rev. Lett. **102**, 230402 (2009).
- [Ser07] F. Serwane, *The setup of a Magneto Optical Trap for the preparation of a mesoscopic degenerate Fermi gas*, Diploma thesis (2007).
- [Ser11] F. Serwane, G. Zürn, T. Lompe, T. B. Ottenstein, A. N. Wenz, S. Jochim, *Deterministic preparation of a tunable few-fermion system*, <http://arxiv.org/abs/1101.2124> (2011).

- [She10] J. F. Sherson, C. Weitenberg, M. Endres, M. Cheneau, I. Bloch, S. Kuhr, *Single-atom-resolved fluorescence imaging of an atomic Mott insulator*, Nature **467**, 68–72 (2010).
- [Shi06] Y. Shin, M. W. Zwierlein, C. H. Schunck, A. Schirotzek, W. Ketterle, *Observation of Phase Separation in a Strongly Interacting Imbalanced Fermi Gas*, Phys. Rev. Lett. **97**, 030401 (2006).
- [Sko57] G. Skorniakov, K. Ter-Martirosian, *Three body problem for short range forces I. Scattering of low energy neutrons by deuterons*, Sov. Phys. JETP **4**, 648 (1957), [J. Exptl. Theoret. Phys. (U.S.S.R.) 31 (1956) 775].
- [STA05] STAR Collaboration, *Experimental and theoretical challenges in the search for the quark-gluon plasma: The STAR Collaboration’s critical assessment of the evidence from RHIC collisions*, Nuclear Physics A **757**(1-2), 102–183 (August 2005).
- [Ste08] J. T. Stewart, J. P. Gaebler, D. S. Jin, *Using photoemission spectroscopy to probe a strongly interacting Fermi gas*, Nature **454**, 744–747 (2008).
- [Ste09] J. von Stecher, J. P. D’Incao, C. H. Greene, *Signatures of universal four-body phenomena and their relation to the Efimov effect*, Nature Physics **5**, 417 (2009).
- [Str03] K. E. Strecker, G. B. Partridge, R. G. Hulet, *Conversion of an Atomic Fermi Gas to a Long-Lived Molecular Bose Gas*, Phys. Rev. Lett. **91**, 080406 (2003).
- [Str06] E. W. Streed, J. Mun, M. Boyd, G. K. Campbell, P. Medley, W. Ketterle, D. E. Pritchard, *Continuous and Pulsed Quantum Zeno Effect*, Phys. Rev. Lett. **97**, 260402 (2006).
- [Tho05] S. T. Thompson, E. Hodby, C. E. Wieman, *Ultracold Molecule Production via a Resonant Oscillating Magnetic Field*, Phys. Rev. Lett. **95**, 190404 (2005).
- [Tre11] A. Trenkwalder, C. Kohstall, M. Zaccanti, D. Naik, A. I. Sidorov, F. Schreck, R. Grimm, *Hydrodynamic Expansion of a Strongly Interacting Fermi-Fermi Mixture*, Phys. Rev. Lett. **106**, 115304 (2011).
- [Tru01] A. G. Truscott, K. E. Strecker, W. I. McAlexander, G. B. Partridge, R. G. Hulet, *Observation of Fermi Pressure in a Gas of Trapped Atoms*, Science **291**, 2570–2572 (2001).
- [Vol04] M. Voloshin, *Interference and binding effects in decays of possible molecular component of X(3872)*, Physics Letters B **579**, 316–320 (2004).
- [Web03] T. Weber, J. Herbig, M. Mark, H.-C. Nägerl, R. Grimm, *Three-Body Recombination at Large Scattering Lengths in an Ultracold Atomic Gas*, Phys. Rev. Lett. **91**, 123201 (2003).

- [Wei09] M. Weidemüller, C. Zimmermann (Ed.), *Cold Atoms and Molecules* (WILEY-VCH, 2009).
- [Wen09a] A. N. Wenz, *Few-Body Physics in a Three-Component Fermi Gas*, Diploma thesis (2009).
- [Wen09b] A. N. Wenz, T. Lompe, T. B. Ottenstein, F. Serwane, G. Zürn, S. Jochim, *Universal trimer in a three-component Fermi gas*, *Phys. Rev. A* **80**, 040702 (2009).
- [Wil09] J. R. Williams, E. L. Hazlett, J. H. Huckans, R. W. Stites, Y. Zhang, K. M. O’Hara, *Evidence for an Excited-State Efimov Trimer in a Three-Component Fermi Gas*, *Phys. Rev. Lett.* **103**, 130404 (2009).
- [Zac09] M. Zaccanti, B. Deissler, C. D’Errico, M. Fattori, M. Jona-Lasinio, S. Müller, G. Roati, M. Inguscio, G. Modugno, *Observation of an Efimov spectrum in an atomic system*, *Nat Phys* **5**, 586–591 (2009).
- [Zür09] G. Zürn, *Realization of an Optical Microtrap for a Highly Degenerate Fermi Gas*, Diploma thesis (2009).
- [Zwi03] M. W. Zwierlein, C. A. Stan, C. H. Schunck, S. M. F. Raupach, S. Gupta, Z. Hadzibabic, W. Ketterle, *Observation of Bose-Einstein Condensation of Molecules*, *Phys. Rev. Lett.* **91**, 250401 (2003).
- [Zwi04] M. W. Zwierlein, C. A. Stan, C. H. Schunck, S. M. F. Raupach, A. J. Kerman, W. Ketterle, *Condensation of Pairs of Fermionic Atoms near a Feshbach Resonance*, *Phys. Rev. Lett.* **92**, 120403 (2004).
- [Zwi05] M. W. Zwierlein, J. R. Abo-Shaeer, A. Schirotzek, C. H. Schunck, W. Ketterle, *Vortices and superfluidity in a strongly interacting Fermi gas*, *Nature* **435**, 1047–1051 (2005).
- [Zwi06a] M. Zwierlein, *High-Temperature Superfluidity in an Ultracold Fermi Gas*, Dissertation, MIT (2006).
- [Zwi06b] M. W. Zwierlein, A. Schirotzek, C. H. Schunck, W. Ketterle, *Fermionic Superfluidity with Imbalanced Spin Populations*, *Science* **311**, 492–496 (2006).
- [Zwi06c] M. W. Zwierlein, C. H. Schunck, A. Schirotzek, W. Ketterle, *Direct observation of the superfluid phase transition in ultracold Fermi gases*, *Nature* **442**, 54–58 (2006).

Acknowledgments

This thesis would not have been possible without the help and support I received from a great number of people, of whom I can name only a small fraction here.

First and foremost, I have to thank Selim for being a great advisor. He basically spent his first year as a professor in the lab, teaching Friedhelm, Timo and me how to build one of the best Lithium machines in the world. He always took the time to interact with his students, and was always patient in explaining when it took us a little longer to catch up with him. He is a great boss, who always listens and with whom one can have heated discussions without there being hard feelings afterwards. Being his minion for the past four years has certainly been an honor and a privilege.

Next I would like to thank my fellow group members (in order of appearance): Friedhelm, Timo, Andre, Gerhard(t), Matthias, Martin, Philipp, Daniel, Johanna and Andrea. They did not only contribute to this thesis in more ways than can be listed here, they also created a relaxed atmosphere and group spirit that made it a pleasure to come to work (one might even call it "work") each day. Especially our lunchtime conversations with their wildly changing and often questionable topics, which were followed by intense table soccer matches, were a constant source of entertainment.

Friedhelm was the first diploma student of our group; when I signed up a few months later he made me feel welcome immediately. Timo started his PhD shortly before I joined, he taught me about setting up optics and until he left a year ago he was the theoretical backbone of our group. When Matthias joined our group he immediately began working on the optical dipole trap and developed the first iteration of the setup for the creation of arbitrary optical potentials, which later turned out to be of great importance for our measurements of atom-dimer collisions. Andre was the first of our group to dive into the Braaten-Hammer review, which was a daunting task for someone completely new to the field of few-body physics. His dedication was essential for understanding what was going on in our three-body system. When Gerhard joined our group he quickly proved to be a tenacious worker with an amazing talent for building stuff, ranging from his G-Tower, which is sure to stand the test of time, over numerous electronics to the improved RF-antenna which enabled the RF-spectroscopy of Efimov trimers. I am especially grateful to Kirsten, who came over from Texas to work on the microtrap, and instead ended up helping me measure atom-dimer collisions in the cave of dying function generators.

Martin and Phillip were the first members of our group who started working on the new experiment, which we decided to build when it became clear that adding a lattice to the three-component system was the natural next step. They planned

and set up the vacuum chamber and created the first MOT in less than a year, which is remarkable achievement. With the help of Andre – who returned from Berkeley to start his PhD in our group – and Johanna, our new Diploma student this experiment will probably prepare its first three-component Fermi gases very soon.

To Joachim Ullrich and his entire group I am grateful for their constant support and many interesting discussions. They were also worthy opponents at table soccer. We will miss them when we move down to the city next year.

A good thing about the move is that it will bring us closer to the groups of Markus Oberthaler and Matthias Weidemüller, with whom we already had a fruitful exchange over the past few years. Being next door to them, especially the NaLi and LiCS experiments will certainly be a great inspiration.

I would also like to thank the staff of the MPI-K, which was a great help in our work. Especially I want to thank Stephan Flicker and Florian Säubert from the teaching workshop: Without their dedicated work and technical expertise, our machine would be missing some of its most important components.

Eric Braaten, Hans-Werner Hammer and Jose D’Incao took a lot of time to teach us about the physics behind the Efimov effect. Without their help, we never would have figured out what was going on in our system.

A special thanks goes to my beta readers Andre, Martin and Johanna who spent a lot of time and work polishing the rough edges off this thesis.

My friends and fellow physicists Christian, Friedor, Joelle, Lukas, Maria, Matthias, Peter, Stefan and Wolfgang I do not only thank for their help in doing exercises and studying for the various tests and examinations, but also for the time we spent together just having fun. Without the countless barbecues, nights out in town and evenings spent discussing in the Handschuhsheimer Landstrasse 63 my studies of physics certainly would have been a lot less enjoyable.

Last but not least I want to thank my family, especially my parents and my brother. There are few things as comforting as knowing that you are there for me.